THE BELL SYSTEM
TECHNICAL JOURNAL

Volume 48 February 1969 Number 2

The Application of Delta Modulation to Analog-to-PCM Encoding

By DAVID J. GOODMAN

(Manuscript received September 24, 1968)

This paper describes a pulse code modulation (PCM) encoder that employs a delta modulator as the analog-to-digital converter. A tapped binary shift register and an up-down counter cause delta modulation signals to be converted to a uniformly quantized PCM format. When tap weights are optimized with respect to a minimum mean square error criterion, the number of shift register stages necessary to obtain a fixed level of output quantizing noise varies inversely with delta modulation sampling rate. Because the tap weights may be rounded to a modest number of binary places, the arithmetic operations are simple to implement. A significant portion of the delta modulation-to-PCM converter may be time shared among several signals.

I. INTRODUCTION

Although delta modulation (ΔM) has been the subject of many theoretical and experimental studies, instances of its practical application are, to date, rare. In commercial systems, the most prominent digital representation of continuous signals is pulse code modulation (PCM). Relative to PCM, ΔM has the advantage of admitting simpler means of analog-to-digital and digital-to-analog conversion. However, the ΔM sampling rate is higher than that of PCM and in many cases the transmission rate is also higher.

Since the discovery of delta modulation in the early 1950's,[1, 2] in-

vestigators have proposed various modifications of the elementary, single-integration ΔM system (for example, double integration ΔM^2, high information ΔM^3, continuous ΔM^4) for the purpose of decreasing the required sampling rate. Generally, lower rates are achieved by means of operations on the continuous signals presented to and appearing in the delta modulator and thus at the expense of equipment complexity.

In this paper we propose a PCM encoder that incorporates the simple single-integration delta modulator and a transversal digital filter that converts the ΔM sequence to a uniformly quantized PCM sequence. For this encoder, we demonstrate an inverse relationship between the ΔM sampling rate and the number of digital filter stages required to achieve a specified level of PCM quantizing noise power. With this encoder the advantages of ΔM, in particular the simple means of analog-to-digital conversion, may be combined with those of PCM: a linear representation of the continuous signal and in many cases a lower transmission rate than that required by simple ΔM. This union of ΔM and PCM is achieved with a digital filter which may be readily implemented with integrated circuit devices.

In the following sections of this paper, we demonstrate the validity of a transversal filter as a ΔM-PCM converter by reference to a ΔM-analog-PCM signal processing sequence. We then criticize the digital filter design method that is based on simulation of the analog system and we proceed to demonstrate the relevance of a mean square error design criterion. The associated synthesis method results in a class of encoders for each output signal-to-noise ratio. Within each class the required sampling rate is inversely related to the number of digital filter stages.

II. THE ΔM SYSTEM

Fig. 1 shows a delta modulator that transforms a continuous input signal $y(t)$ to the binary sequence

$$\{b_n\} = \cdots, b_{-1}, b_0, b_1, \cdots \tag{1}$$

in which b_i may have the value $+1$ or -1. These binary symbols are generated at τ second intervals; we assume that $y(t)$ is a member of a class of signals band-limited to W Hz. Thus we can represent $y(t)$ by a sequence of PAM samples generated at the rate of $2W$ per second. In order to simplify the ΔM-PCM conversion, we constrain the delta modulator such that its output rate, $1/\tau$, is an integral multiple

of the PAM rate. The ratio of its input (ΔM) rate to its output (PAM) rate is a basic parameter of the ΔM-PCM converter. This ratio is the integer

$$R = \frac{1}{2W\tau}. \tag{2}$$

The other basic parameter is the step size, δ, the gain of the modulator feedback loop. Assume that the linear filter in this loop is an ideal integrator with impulse response

$$\begin{aligned} f(t) &= 1 \quad \text{for} \quad t \geqq 0 \\ &= 0 \quad \text{for} \quad t < 0 \end{aligned} \tag{3}$$

so that the integrated ΔM signal, $x(t)$, contains a step of height $\pm\delta$ at each ΔM sampling instant and is constant between sampling instants. R and δ determine the inherent quantizing noise of the delta modulator, and δ, in a practical system, is selected to provide a proper balance between granular[9,11] quantizing noise (that predominates for high values of δ) and slope-overload noise (the predominant form for low values of δ).[5,6,7] In the analysis to follow, assume that no slope overload occurs; to make this assumption valid, we specify the parameter δ such that δ/τ, the maximum slope of the analog signal that may be reconstructed from $\{b_n\}$, is four times the rms slope of $y(t)$. If $y(t)$ is a sample function of a stationary time series with power density spectrum $Y(f)$, the spectrum of the time derivative of $y(t)$ is $(2\pi f)^2 Y(f)$, and the parameter β, the ΔM step size as a multiple of rms signal amplitude, is

$$\beta = \frac{\delta}{\sigma} = 8\pi\tau f_e \tag{4}$$

where we define

$$f_e = \left[\frac{\int_0^W f^2 Y(f)\, df}{\int_0^W Y(f)\, df} \right]^{\frac{1}{2}} \tag{5}$$

as the "effective frequency width" of the analog input. If f_e is expressed as a constant times W, the cutoff frequency of $Y(f)$, it is clear that equation (4) is proportional to τW, so that for a given spectral density function, βR is a constant.

The ΔM design condition of equation (4) is identical to the one adopted by van de Weg[9] in his analysis of the granular quantizing noise of ΔM and it is analogous to the "4σ loading" which is the basis

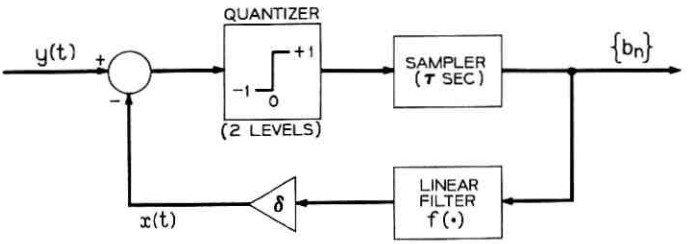

Fig. 1 — Delta modulator.

of Bennett's analysis of PCM quantizing noise.[10] If slope overload noise as well as granular noise is taken into account, analytic and simulation studies[6, 7] indicate that for minimal overall quantizing noise, the parameter βR [a constant in equation (4)] should increase with increasing R. For $R = 32$, equation (4) approximates the optimal step size, but for lower values of R the total quantizing noise inherent in $\{b_n\}$ may be reduced if a lower δ is accepted. A decrease in δ reduces the quantity of granular noise in the ΔM system while increasing the slope overload content.

The analytic work reported in this paper follows Bennett and van de Weg by constraining the ΔM parameters to conform to equation (4) and by assuming that no slope overload occurs. [If $y(t)$ is drawn from a gaussian random process, the probability that its derivative exceeds δ/τ is less than 4×10^{-5}.]

III. THE ΔM-PCM CONVERTER

Fig. 2 shows a ΔM-PCM converter that consists of an analog-to-PCM encoder operating on the analog signal produced by a ΔM receiver. This receiver contains a replica of the delta modulator feedback loop and a linear filter that in many analytic studies is considered to possess an ideal low-pass transfer function. This filter

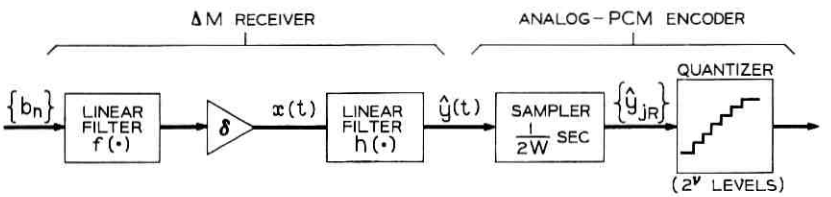

Fig. 2 — ΔM-analog-PCM converter.

processes the integrated ΔM signal, $x(t)$, and rejects the portion of its quantizing noise that lies outside the W Hz bandwidth of the original analog signal. In Fig. 2, ΔM signals are accepted by the converter at τ second intervals and PAM samples are presented to the PCM quantizer every $1/2W = R\tau$ seconds. The PAM sample that approximates $y_{iR} = y(jR\tau)$ is $\hat{y}_{iR} = \hat{y}[(jR + M)\tau]$ in which the delay of the filter $h(\cdot)$ is assumed to be $M\tau$ seconds. This output sample is related to $\{b_n\}$, the ΔM input of Fig. 2, by

$$\hat{y}_{iR} = \delta \sum_{n=0}^{\infty} g_n b_{iR+M-n} \tag{6}$$

where $g_n = g(n\tau)$ and $\delta g(\cdot)$ is the impulse response of the ΔM receiver. Thus, $g(\cdot)$ is the convolution of $f(\cdot)$ and $h(\cdot)$.

In the case of single integration ΔM, $f(\cdot)$ is the unit step function and $g(\cdot)$ is the unit step response of the filter $h(\cdot)$, that is,

$$g(t) = \int_0^t h(u)\, du. \tag{7}$$

Thus $h(\cdot)$ may be scaled such that

$$\lim_{n\to\infty} g_n = 1$$

which implies that a number N exists such that equation (6) may be approximated with arbitrary accuracy by

$$\hat{y}_{iR} \cong \delta \sum_{n=0}^{N-1} g_n b_{iR+M-n} + \delta \sum_{n=N}^{\infty} b_{iR+M-n}. \tag{8}$$

The second term in equation (8) may be realized by an up-down counter operating on the ΔM input delayed by $N\tau$ seconds. The first term is the weighted sum of the outputs of a tapped binary shift register. The structure implied by equation (8) is shown in Fig. 3.

Figure 3 represents a transversal filter with analog coefficients generating a discrete-time analog output, $\{\hat{y}_{iR}\}$. The required quantization of $\{\hat{y}_{iR}\}$ may be realized by means of the quantization of the filter coefficients.* The purpose of the converter implies the digitization of Fig. 3 and its implementation (with finite-precision arithmetic) as the entire ΔM-PCM converter.

---

* In this paper, a PCM encoder is assumed to consist of a sampler and quantizer only. In a transmission system this encoder would be followed by a "channel encoder" that represents the quantized signal in an appropriate (for example, binary or multilevel) format.

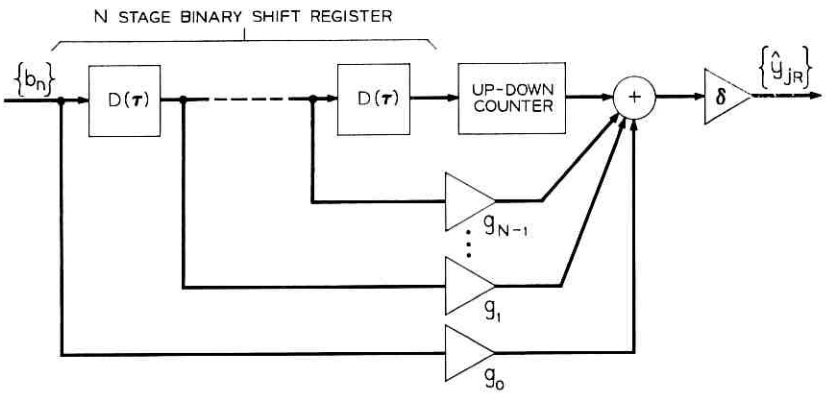

Fig. 3 — Digital ΔM-PCM converter [$D(\tau)$ denotes a τ second delay].

3.1 *Simulation of the Analog System*

If this digital converter is designed to simulate the analog-interface structure of Fig. 2, the filter coefficients, g_n, may be derived as samples, separated by τ seconds, of the unit step response of the filter $h(\cdot)$. In order to find N, the required number of coefficients, a number ϵ is chosen to represent the maximum tolerable truncation error. This error is bounded in the following expression

$$\epsilon \leqq \delta \sum_{n=N}^{\infty} | 1 - g(n\tau) | \cong \frac{\delta}{\tau} \int_{N\tau}^{\infty} | 1 - g(t) | \, dt. \tag{9}$$

Because δ/τ is constant with changing sampling rates the truncation error requirement implies a constant value of $N\tau$ or N/R. Thus the number of filter stages is proportional to the ΔM sampling rate when the design procedure is based in this manner on the simulation of the analog interface converter. A similar conclusion was reached by O'Neal who employed a different simulation procedure but found the number of required filter stages to be $N = 10R$.†

3.2 *Critique of the Analog Simulation Method*

The principal goal of the present study is to demonstrate the relationship between the ΔM speed (proportional to R) and the digital filter complexity (indicated by N), required to obtain PCM output signals of a given quality. As R increases, the difference between

† O'Neal, J. B., unpublished memorandum relating to the computer simulation, the results of which are given in Ref. 6.

the integrated ΔM signal [$x(t)$ in Fig. 2] and the analog input is reduced; this implies that in order to achieve a fixed output fidelity, the noise rejection requirements of the digital filter may be relaxed. It would be desirable to represent the reduced performance demands on the converter as a decrease in its complexity, N. Since the simulation design technique achieves the opposite result we use a minimum mean square error design which admits the calculation of optimum coefficient values for any N and the derivation of the desired trade-off between ΔM speed and converter complexity.

3.3 *Minimal Mean Square Error Design*

The converter in Fig. 3 derives an estimate of y_{jR} that is a linear combination of a finite set of sample values of $x(t)$. Thus we are able to use the covariance statistics of the sampled data sequences $\{y_{jR}\} = \{y(jR\tau)\}$ and $\{x_n\} = \{x(n\tau)\}$ to calculate optimal (with respect to mean square error) values of the filter coefficients.

We consider the desired PAM sample, $\hat{y}_{jR}$, to be an estimate of y_{jR} that is based on the statistical evidence of the ΔM sequence, $\cdots$, b_{-1}, b_0, b_1, $\cdots$, b_{jR+M}, beginning in the indefinite past relative to $t = jR\tau$ and terminating with the $(jR + M)$th binary symbol. If M is negative, the estimation process involves prediction of y_{jR} on the basis of information available (at the delta modulator) prior to t = $jR\tau$. In the case considered here, M will range over nonnegative numbers and the estimator will have a lag of $M\tau$ seconds.

The linear estimation design problem involves the specification of the infinite set of coefficients α_n in the estimation formula

$$\hat{y}_{jR} = \sum_{n=-\infty}^{jR+M} \alpha_{jR-n} b_n \,. \tag{10}$$

This problem will be approached by a consideration of the sample values of $x(t)$, the integrated ΔM signal:

$$x(t) = \delta \sum_{n=-\infty}^{k} b_n \quad \text{for} \quad k\tau \leqq t < (k+1)\tau.$$

Each sample value, $x_n = x(n\tau)$, depends on the entire history of the ΔM sequence. The character of $x(t)$ and its relation to $y(t)$, the original analog signal, are illustrated in Fig. 4. Except when the system is in a slope overload condition, x_n differs from the analog signal by no more than two times the step size. Thus,

$$|x_n - y_n| \leqq 2\,\delta. \tag{11}$$

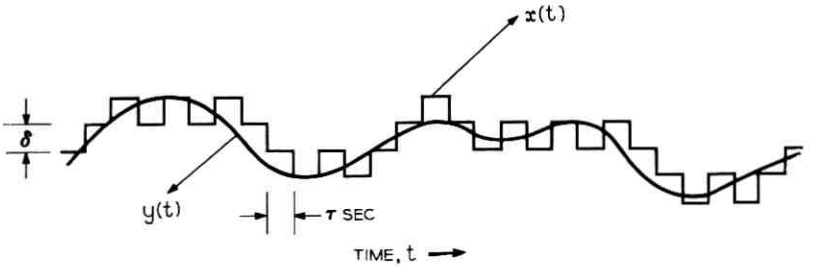

Fig. 4 — Analog input, $y(t)$, and integrated ΔM signal, $x(t)$.

Equation (11) and Fig. 4 suggest that x_n is closely correlated with y_{jR} for values of n near jR. Such correlation implies the usefulness of the $N = 2M + 1$ samples, $x_{jR-M}, x_{jR}, \ldots, x_{jR+M}$ in the estimation of y_{jR}. These N sample values comprise the statistical evidence of the estimate,

$$\hat{y}_{jR} = \sum_{k=-M}^{M} a_k x_{jR-k} \, . \tag{12}$$

Adoption of equation (12) requires the derivation of only a finite set of coefficients, a significant improvement over the situation suggested by equation (10). The two estimation procedures are identical, however, because the infinite set of α_n in equation (10) may be calculated directly from the N values of a_k as

$$\begin{aligned} \alpha_n &= \delta \sum_{k=-M}^{n} a_k \qquad -M \leqq n \leqq M \\ \alpha_n &= \delta \sum_{k=-M}^{M} a_k = \alpha_M \qquad n > M. \end{aligned} \tag{13}$$

Thus equation (12) may be rewritten,

$$\hat{y}_{jR} = \sum_{n=-M}^{M} \alpha_n b_{jR-n} + \alpha_M \sum_{n=M+1}^{\infty} b_{jR-n} \, , \tag{14}$$

which is equivalent to equation (8) with $N = 2M + 1$ and $\delta g_{n+M} = \alpha_n$. Thus the estimation procedure of equation (12) may be realized by the structure shown in Fig. 3.

We now consider the mean square estimation error of equation (12)

$$\eta = E\{(y_{jR} - \hat{y}_{jR})^2\} \tag{15}$$

or

$$\eta = \sigma^2 - 2 \sum_{k=-M}^{M} a_k E\{y_{jR} x_{jR-k}\} + \sum_{k=-M}^{M} \sum_{l=-M}^{M} a_k a_l E\{x_{jR-k} x_{jR-l}\} \tag{16}$$

where $E\{\cdot\}$ is the expectation operator. The expected values on the right side of equation (16) are, respectively, the cross-covariance function of $\{y_{jR}\}$ and $\{x_n\}$ and the autocovariance function of $\{x_n\}$. It has been shown that if $y(t)$ is a member of a stationary ensemble, the sequence of samples $\{x_n\}$ is also stationary.[11] Thus we may adopt the notation

$$\Phi_k = E\{y_{jR}x_{jR-k}\} \tag{17}$$

for the cross-covariance which depends only on $|k|$ and

$$r_\mu = E\{x_{jR-k}x_{jR-l}\} \tag{18}$$

for the autocovariance which is a function only of $|\mu| = |l - k|$. Equation (16) will now be expressed in matrix notation in terms of Φ and A defined as column vectors ($N \times 1$ matrices) with components Φ_k and $a_k(-M \leqq k \leqq M)$ respectively, and in terms of ψ, defined as the $N \times N$ autocovariance matrix with components $\psi_{k,l} = r_{l-k}(-M \leqq k, l \leqq M)$. Thus we have

$$\eta = \sigma^2 - 2A^T\Phi + A^T\psi A. \tag{19}$$

If the mean value of $y(t)$ is zero the coefficients for which η is minimized are given by[12]

$$A^* = \psi^{-1}\Phi \tag{20}$$

and the minimal mean square error is

$$\eta_{\min} = \sigma^2 - \Phi^T\psi^{-1}\Phi \tag{21}$$

which is the result of substituting A^* in equation (20) for A in equation (19).

The Appendix shows that when $y(t)$ is a sample function of a stationary gaussian process the estimation error may be expressed in terms of the quantizing noise correlation vector Q with components $Q_k(-M \leqq k \leqq M)$, the correlation coefficients of the error samples $\{y_n - x_n\}$. Equation (21) may be approximated by

$$\eta_{\min} \cong Q_0 - Q^T\psi^{-1}Q. \tag{22}$$

IV. ENCODER CHARACTERISTICS

The Appendix gives formulas for the correlation coefficients, r_μ and Φ_k associated with the encoding of an analog input signal that is a member of a stationary gaussian ensemble. These formulas have been applied to the calculation of filter coefficients [equation (20)] and the

quantizing noise power [equation (21)] of the PCM samples generated by optimal linear processing of the ΔM sequence. In particular, the relationships among the following three parameters have been investigated: (*i*) R, the bandwidth expansion ratio, (*ii*) N, the number of coefficients, and (*iii*) $S = \sigma^2/\eta_{\min}$ the signal-to-quantizing-noise ratio.

This signal-to-noise ratio is a function of the spectrum of the processed signal and of N and R which have been treated as independent variables in the calculations. In a practical design procedure, S would be the independent variable, specified according to the system fidelity criterion. With S fixed, N and R vary inversely; in practice their values would be selected as a compromise between the objectives of achieving low ΔM speed (low R) and a simple converter structure (low N).

Figure 5 pertains to a system whose gaussian input process has a flat spectrum band-limited to W Hz. The solid curves show S as a function of R for various values of N and the broken curve indicates the result of optimal analog processing of the integrated ΔM signal.

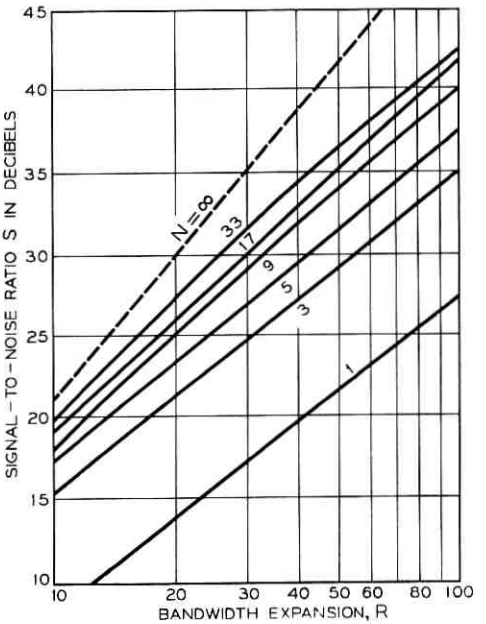

Fig. 5 — Performance curves, flat spectrum.

This curve, the ratio of σ^2 to η_∞ [see Appendix, equation (42)], is a bound on the solid curves. It corresponds to the signal-to-noise ratio of a transversal filter with an unlimited number of stages. The slope of the broken curve is 30 dB/decade.

The lowest curve in Fig. 5 indicates the signal-to-noise ratio of the encoder with a digital filter with one coefficient. For $R \geqq 16$, this coefficient may be set equal to unity with little (less than 0.5 dB) loss in estimation accuracy. With a unit coefficient, the converter reduces to an up-down counter alone, and the encoder consists only of a delta modulator and a counter as shown in Fig. 6. In this case each PCM output is a sample of the integrated ΔM signal, $x(t)$. Sampling this signal (whose bandwidth is RW Hz) at the Nyquist rate of the analog input results in aliasing of the high frequency noise components of $x(t)$ into the W Hz signal band of the coded signal. The noise power in the output of Fig. 6 is the entire mean square error of $\{x_n\}$,

$$Q_0 = E\{(y_n - x_n)^2\} \cong \delta^2/3, \tag{23}$$

so that the signal-to-noise ratio increases with ΔM speed at the rate of 20 dB/decade.

The effect of setting $N = 3$, which involves the addition of a 2-stage tapped binary shift register to Fig. 6 is (for $R \geqq 16$) a signal-to-noise ratio improvement of more than 7 dB or a ΔM speed reduction by a factor of 2.4 for a fixed value of S. Two additional stages ($N = 5$) further increase S by 2 dB or reduce the ΔM speed required for fixed S to less than one-third of that required when only an up-down counter is employed. Figure 5 demonstrates the manner in which further (through diminishing) improvements are obtained with the incorporation of additional coefficients and stages of delay.

Notice some of the functions that the transversal filter may be said to perform. In particular its noise reduction effects may be viewed as the result of filtering in the frequency domain, of statistical estimation, or of digital interpolation. Viewed as a substitute for the analog filter in Fig. 2, the transversal filter may be said to reject the out-of-band components of the error signal, $y(t) - x(t)$. As the number of stages increases, the filter cutoff becomes sharper and the output noise power is reduced.[13] Considered as an estimator of a random variable, the filter bases its estimates on an increasing number of correlated data as N increases. The quadratic form, $Q^T\psi^{-1}Q$, consisting of correlation coefficients, increases with increasing N and therefore the output noise power given by equation (22) decreases. Finally, the filter may be viewed as an interpolator. As the number

Fig. 6 — Encoder structure for $N = 1$.

of filter stages increases, the ΔM speed may be decreased and a proportionally greater step size may be tolerated in the delta modulator. The resolution of the ΔM signal is thus reduced while the accuracy of the PCM output is maintained due to the interpolation performed by the digital filter between increasingly separated ΔM quantization levels.

4.1 *Digitization of Coefficient Values*

The data of Fig. 5 apply strictly to an analog estimate obtained with analog coefficients. ("Analog" numbers in this context mean numbers quantized to the precision of the numerical methods used in calculating the coefficient values.) In a practical application of the ΔM–PCM conversion method, the coefficients would exist in digital form; in order to investigate this situation, we will consider the effect of rounding the values of the derived coefficients to a limited number of binary places.

In the discussion that follows, it will be convenient to divide equation (14) by δ and to consider the estimator of y_{jR}/δ, given by

$$\frac{\hat{y}_{jR}}{\delta} = \sum_{n=-M}^{M-1} \gamma_n b_{jR-n} + \gamma_M \sum_{n=M}^{\infty} b_{jR-n} \tag{24}$$

in which $\gamma_i = \alpha_i/\delta$. The coefficients of equation (24) are related to the components of A, the coefficient vector, by the sums

$$\gamma_n = \sum_{k=-M}^{n} a_k \qquad -M \leqq n \leqq M. \tag{25}$$

In the digitization of the ΔM–PCM converter, the set of analog coefficients, $\gamma_{-M}, \cdots, \gamma_0, \cdots, \gamma_M$, is rounded to L binary places by means of the computation

$$\gamma_i(L) = 2^{-(L-1)} \times [\text{the greatest integer} \leqq 2^{(L-1)}\gamma_i + 0.5]. \tag{26}$$

Corresponding to the limited-precision coefficients of equation (26) is a quantized coefficient vector,

$$A(L) = [a_{-M}(L), \cdots, a_0(L), \cdots, a_M(L)]^T,$$

whose components are calculated according to

$$a_{-M}(L) = \gamma_{-M}(L)$$

$$a_i(L) = \gamma_i(L) - \gamma_{i-1}(L) \quad -M+1 \leqq i \leqq M. \tag{27}$$

The mean square error of the digitized converter may be calculated from equation (19),

$$\eta(L) = \sigma^2 - 2[A(L)]^T \Phi A(L) + [A(L)]^T \psi A(L). \tag{28}$$

For each estimator considered in the derivation of Fig. 5, the signal-to-noise ratio, $\sigma^2/\eta(L)$, has been computed for $L = 1, 2, \ldots, 15$ binary places in each coefficient.

Under the assumption that the quantization of coefficients is not allowed to degrade the signal-to-noise ratio by more than 0.5 dB, Table I has been obtained. L^* in this table is the minimum value of L for which the inequality

$$10 \log [\eta(L)/\eta_{\min}] < 0.5$$

is valid over all $R \geqq 10$.

When the coefficients are rounded to L^* places according to Table I, we find in every case that $\gamma_M(L) = 1$ so that equation (24) may be specified as

$$\frac{\hat{y}_{iR}}{\delta} = \sum_{n=-M}^{M-1} \gamma_n(L^*) b_{iR-n} + \sum_{n=M}^{\infty} b_{iR-n}. \tag{29}$$

The second summation in equation (29) is the output of the up-down counter (which requires no weighting); the first summation may be implemented by means of a tapped binary shift register with $2M = N - 1$ stages.

It is also the case that for $n < M$, $\gamma_n(L^*) < 1$, so that each of the $N - 1$ tap weights is a proper binary fraction that may be represented by $L^* - 1$ bits. The output of the counter ranges over the set of integers and the tapped shift register serves as an interpolator so that the resultant PCM output is more finely quantized than the

TABLE I — EFFECT OF COEFFICIENT ROUND-OFF

Required coefficient accuracy (L^*)	1	4	4	5	7	8
Number of coefficients (N)	1	3	5	9	17	33

sample values of the integrated ΔM signal, of which it is a weighted sum.

4.2 Other Signal Spectra

The data of Fig. 5 relate to the processing of analog input signals that possess a flat band-limited spectrum. Converter performance characteristics have also been obtained for analog input signals with spectral density functions of the general form

$$\begin{aligned} Y(f) &= \frac{2\pi}{f_c \tan^{-1}\left(\frac{2\pi W}{f_c}\right)} \times \frac{f_c^2}{(2\pi f)^2 + f_c^2} \qquad |f| \leqq W \\ &= 0 \qquad |f| > W. \end{aligned} \tag{30}$$

Such spectra result when band limited white noise is processed by a low-pass RC filter with corner frequency $f_c = 1/RC$.

Corresponding to the examples analyzed by O'Neal, two spectra conforming to equation (30) have been considered.[6] In one case the ratio f_c/W, of corner frequency to cutoff, is 0.25 and in the other case this ratio is 0.068. These spectra relate to broadcast television and *Picturephone®* visual telephone signals, respectively; the performance curves are given in Figs. 7 and 8. The shapes of these two families of curves are similar to one another; both resemble the curves in Fig. 5. The principal difference betwen any two corresponding curves is a vertical translation whose magnitude is the squared ratio, expressed in dB, of the two relevant step sizes.

Thus, for any of the three spectra considered and a given N and R, the signal-to-noise ratio in dB is approximately the value of S given in Fig. 5 plus the correction

$$-10 \log [3 f_e^2] \text{ dB}. \tag{31}$$

(For signals with a flat spectral density function $f_e^2 = \frac{1}{3}$.)

For spectra in the form of equation (30), this correction is[6]

$$\begin{aligned} 11.19 - 10 \log \left\{ \frac{2\pi(f_c/W)}{\tan^{-1}[2\pi(W/f_c)]} - \left(\frac{f_c}{W}\right)^2 \right\} \\ = 11.35 \text{ dB} \quad \text{for} \quad f_c/W = 0.25 \\ = 16.89 \text{ dB} \quad \text{for} \quad f_c/W = 0.068. \end{aligned} \tag{32}$$

For speech signal processing, realistic analytic results are more difficult to obtain. Signal spectra vary from speaker to speaker; the

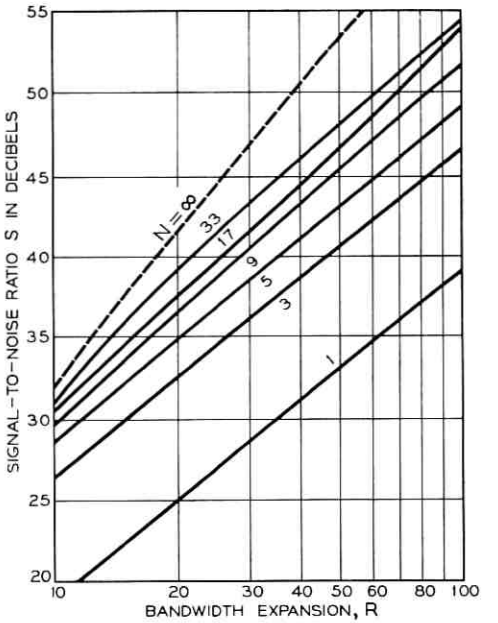

Fig. 7 — Performance curves, RC spectrum, $f_c/W = 0.25$.

portion of the speech spectrum to be conveyed depends on the application. A particularly severe problem arises when a range of signal levels must be accommodated by the encoder. To treat this problem, it may be possible to introduce companding to the delta modulator; but the solution currently favored is the acceptance of a higher ΔM sampling rate than would be required if the signal level were fixed and the introduction of a digital compandor[14] to operate on the uniformly quantized signal produced by the ΔM–PCM converter.

4.3 *A Design Example*

This section demonstrates the form of a converter designed to process the digital representation of analog signals with a band-limited RC spectrum in which $f_c/W = 0.068$. We assume that a PCM signal-to-noise ratio of at least 41 dB is required, and refer to Fig. 8 to determine values of N and R for which this requirement may be met. For each value of N illustrated in Fig. 8, the required R is given in Table II. Thus the converter in which $N = 5$ and $R = 24$ meets the stated objective. Table III gives the optimal coefficients a_i, α_i, and the limited precision set,

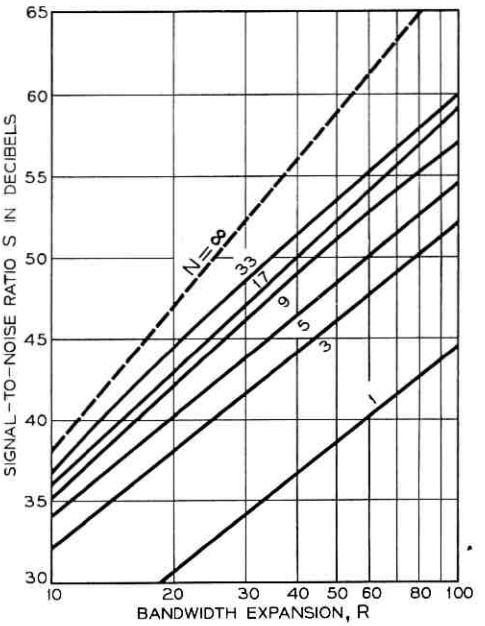

Fig. 8 — Performance curves, RC spectrum, $f_c/W = 0.068$.

$\gamma_i(4)$, for $-2 \leqq i \leqq 2$. The signal-to-noise ratio associated with the analog coefficients is 41.9 dB and that associated with the coefficients rounded to four binary places is 41.8 dB. (When the coefficients are limited in precision to three binary places, the value of S is reduced to 39.9 dB.)

Figure 9 demonstrates, in the schematic form of Fig. 3, one implementation of the converter. The indicated arithmetic operations need be performed only once for every 24 ΔM inputs accepted by the converter. These operations consist of modification of the sign of each coefficient (multiplication by ± 1), addition of four 3-bit numbers, and addition of their sum to the counter output. The sign modification and coefficient addition operations (shown in the broken box) may be performed by a combination of Boolean logic elements with four binary

TABLE II — VALUES OF N AND R FOR $S \geqq 41$ dB IN FIG. 8

R	67	29	21	18	17	15	13
N	1	3	5	9	17	33	∞

TABLE III — CONVERTER COEFFICIENTS, $N = 5$

i	α_i	α_i	$\gamma_i(4)$ (binary form)
−2	0.15996	0.15996	0.001
−1	0.22575	0.38571	0.011
0	0.22866	0.61437	0.101
1	0.22575	0.84013	0.111
2	0.15996	1.00009	1.000

inputs and five outputs. Because the logical processor is required to operate during only one of every 24 basic time intervals of the system, the possibility exists for it to be shared among other digital signals.

Notice that, in general, for converters in which $N = 5$, it has been found that coefficient values may be truncated to four binary places without unacceptable degradation of converter performance. Furthermore, the coefficients, $\gamma_i(4)$, have, in general, the values given in Table III. Thus, regardless of the spectrum of the analog input and the sampling rate and step size of the delta modulator, the same converter structure may be employed to produce a near-maximum (within 0.5 dB) PCM signal-to-noise ratio. This signal-to-noise ratio is a function primarily of the step size of the delta modulator. Except in the manner that it determines the step size [through equation (4)], the precise shape of the spectrum of the input signal has only a secondary influence on system performance. With regard to the ΔM sampling rate, variations in R affect the converter only by varying the number of ΔM inputs accepted between the generation of

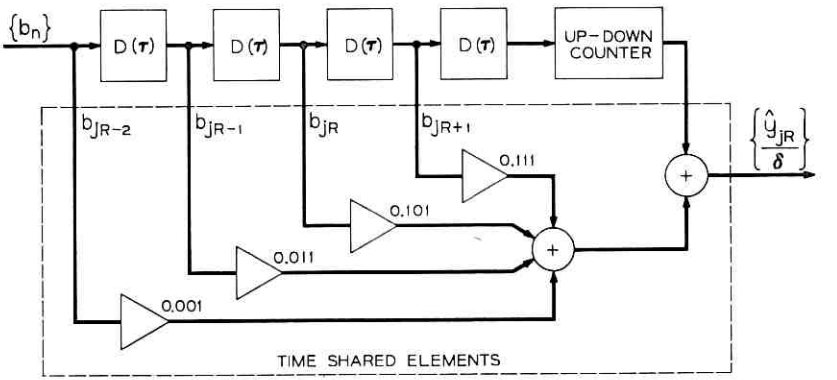

Fig. 9 — Converter structure for $N = 5$.

PCM outputs. The configuration of the logical processor (arithmetic unit) is not altered by changes in ΔM sampling rate.

V. CONCLUSIONS

The PCM encoder described combines the principal advantage of delta modulation, a simple means of analog-to-digital conversion, with the advantages of PCM, a linear representation of the coded signal and often fewer bits per second than are required with ΔM. The result of adopting the minimum mean square error criterion, in the synthesis of the ΔM–PCM converter, is a family of encoders for each possible level of output quantizing noise and thus considerable design flexibility.

The transversal filter in the converter has a particularly simple configuration. The sequence of signals to be processed is represented by one bit per sample so that the only required arithmetic operations are addition and subtraction of prespecified coefficient values. These coefficients may be rounded to a modest number of binary places and the digital filter may be considered to be a combination of elementary Boolean logic elements rather than an arithmetic unit. With the exception of the up-down counter, the elements of the ΔM–PCM converter may be time-shared among several signals.

In addition to being applicable as a general-purpose PCM encoder, the device described in this paper may be adopted to serve in a digital communication system which performs local office switching of signals coded in a ΔM format and trunk transmission of PCM signals. In this application there would be a ΔM modem for each analog station and a limited number of ΔM–PCM converters for processing trunk calls. Elements of such a system are shown schematically in Fig. 10.

APPENDIX

ΔM Signal Statistics, Gaussian Inputs[11]

Expressions have been derived for the matrices required in the application of equations (20) and (21) to the determination of filter coefficients and values of noise power under the assumption that $y(t)$, the input to the delta modulator, is a member of a gaussian ensemble. The correlation coefficients Φ_k and r_μ are presented in this section and the following section expresses the ΔM and PCM quantizing noise characteristics in terms of these correlation characteristics.

The covariance statistics are expressed as functions of the ΔM step

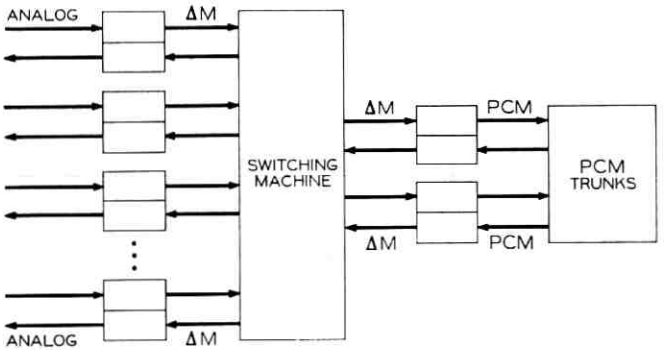

Fig. 10 — An application in which the delta modulator and the ΔM-PCM converter are separated.

size, δ, its normalized value, $\beta = \delta/\sigma$, and the correlation coefficients of the analog input,

$$\rho_k = \frac{1}{\sigma^2} E\{y(n\tau)y[(n+k)\tau]\}. \tag{33}$$

These coefficients are samples, taken at τ second intervals, of the autocorrelation function, $\rho(\cdot)$, of $y(t)$. The power density spectrum, $Y(\cdot)$, is the Fourier transform of $\sigma^2\rho(\cdot)$.

The cross-covariance of the integrated ΔM sequence, $\{x_n\}$, and the samples of the analog input, $\{y_{jR}\}$, is proportional to the autocovariance of $\{y_j\}$. Thus,

$$\Phi_0 = \sigma^2\left\{1 + 2\sum_{k=1}^{\infty} \exp\left[-\frac{2\pi^2k^2}{\beta^2}\right]\right\}$$

and in general

$$\Phi_k = \rho_k\Phi_0 . \tag{34}$$

For the autocovariance of $\{x_n\}$, we have the more complicated formulas:

$$r_0 = \sigma^2\left\{1 + 4\sum_{k=1}^{\infty} \exp\left[-\frac{2\pi^2k^2}{\beta^2}\right]\right\} + \delta^2\left\{\frac{1}{3} + \sum_{k=1}^{\infty}\frac{1}{\pi^2k^2}\exp\left[-\frac{2\pi^2k^2}{\beta^2}\right]\right\}$$

$$r_\mu = \rho_\mu\sigma^2\left\{1 + 4\sum_{k=1}^{\infty} \exp\left[-\frac{2\pi^2k^2}{\beta^2}\right]\right\} + \frac{\delta^2}{\pi^2}\sum_{m=1}^{\infty}\sum_{k=1}^{\infty}\frac{1}{mk}[1 + (-1)^{m+k}]$$

$$\cdot\left\{\exp\left[-\frac{\pi^2(k^2 + m^2 - 2mk\rho_\mu)}{2\beta^2}\right] - \exp\left[-\frac{\pi^2(k^2 + m^2 + 2mk\rho_\mu)}{2\beta^2}\right]\right\}$$

for μ even

$$r_\mu = \rho_\mu\sigma^2\left\{1 + 4\sum_{k=1}^{\infty}\exp\left[-\frac{2\pi^2k^2}{\beta^2}\right]\right\} + \frac{2\delta^2}{\pi^2}\sum_{m=1}^{\infty}\sum_{k=1}^{\infty}\frac{1}{mk}(-1)^m$$
$$\cdot\left\{\exp\left[-\frac{\pi^2(k^2 + m^2 - 2mk\rho_\mu)}{2\beta^2}\right] - \exp\left[-\frac{\pi^2(k^2 + m^2 + 2mk\rho_\mu)}{2\beta^2}\right]\right\}$$
$$\text{for } \mu \text{ odd.} \qquad (35)$$

In most cases of practical interest, the ΔM step size is a fraction of the rms input signal and the formulas in equations (34) and (35) may be simplified considerably. All of the single summations in these formulas involve powers of

$$\exp\left[-\frac{2\pi^2}{\beta^2}\right] = \exp\left[-\frac{19.7}{\beta^2}\right],$$

which for $\beta < 0.5$ is less than 10^{-34}. In this event we have the very accurate approximations

$$\Phi_0 \cong \sigma^2 \quad \text{and} \quad r_0 \cong \sigma^2 + \delta^2/3. \qquad (36)$$

In the formulas for r_μ, there are double sums of the difference of two exponential terms. When equation (36) applies, the second term is negligible and the first term has significant values only when the two indices of summation are equal. We thus have the approximation,

$$r_\mu \cong \rho_\mu\sigma^2 + \frac{2\delta^2}{\pi^2}\sum_{k=1}^{\infty}\frac{(-1)^{\mu k}}{k^2}\exp\left[-\frac{\pi^2k^2(1 - \rho_\mu)}{\beta^2}\right], \qquad (37)$$

which is valid in most cases of practical interest.

A.1 *Quantizing Noise*

A consideration of the statistical properties of the quantizing noise signals that appear in the analog-ΔM–PCM encoder provides insight into the signal processing operations described in this paper. In the delta modulator, we have the error signal $y(t) - x(t)$, that is sampled and quantized to produce the ΔM sequence, $\{b_n\}$. This is a high frequency signal with effective bandwidth RW; the filter, $h(\cdot)$, in the ΔM-analog receiver of Fig. 2 has the role of rejecting its out-of-band components. Similarly, the digital ΔM–PCM converter rejects an increasing proportion of the power of the error signal as N, the number of filter stages, increases. Equation (6) indicates that the performance of a digital ΔM–PCM converter with an unlimited number of stages ($N = \infty$) is equivalent to that of the analog-interface converter of Fig. 2.

The autocovariance coefficients of $\{y_n - x_n\}$, the sequence of

error samples, are

$$Q_k = E\{(y_n - x_n)(y_{n+k} - x_{n+k})\} = \sigma^2\rho_k + r_k - 2\Phi_k . \quad (38)$$

Equations (34) and (38) may be combined in the expression

$$\Phi_k = \frac{\Phi_0}{2\Phi_0 - \sigma^2}(r_k - Q_k) = \frac{C}{2C - 1}(r_k - Q_k) \quad (39)$$

in which we have set

$$C = \frac{\Phi_0}{\sigma^2} = 1 + 2\sum_{k=1}^{\infty} \exp\left[-\frac{2\pi^2 k^2}{\beta^2}\right].$$

Equation (39) may now be substituted into equation (21) for minimum mean square error, $\eta_{\min}$. Appearing in the resulting expression for $\eta_{\min}$ are the terms $r^T\psi^{-1}$ and $\psi^{-1}r$ in which r denotes the column matrix with components $r_k(-M \leqq k \leqq M)$. The two matrix products are transposes of one another; both are identical to quite simple matrices. Thus,

$$r^T\psi^{-1} = [0, 0, \cdots, 1, \cdots, 0, 0] = [\psi^{-1}r]^T. \quad (40)$$

When equation (40) is applied, equation (21) may be expressed in terms of the quantizing noise statistics as

$$\eta_{\min} = \left(\frac{C}{2C - 1}\right)^2 (Q_0 - Q^T\psi^{-1}Q) - \frac{(C - 1)^2}{2C - 1}\sigma^2, \quad (41)$$

in which Q is the error covariance vector and Q_0 is the total power in the error signal, $\{y_n - x_n\}$. Thus $Q^T\psi^{-1}Q$ represents the amount of noise rejected by a digital filter whose coefficients are given by equation (20). Because ψ is positive definite, equation (41) indicates that such a filter cannot enhance the quantizing noise power of the system.

As N increases without limit, the mean square error approaches the quantizing noise power associated with the optimum analog interpolation filter of the ΔM signals. This quantity may be expressed in terms of the signal spectra as[11]

$$\eta_\infty = \lim_{N\to\infty} \eta_{\min} = \left(\frac{C}{2C - 1}\right)^2 \frac{1}{R}\left[Q_0 + 2\sum_{k=1}^{\infty} Q_k \frac{\sin\left(\frac{\pi k}{R}\right)}{\left(\frac{\pi k}{R}\right)}\right.$$

$$\left. - \int_0^1 \frac{[E^*(fW)]^2}{(2C - 1)Y^*(fW) + E^*(fW)}\, df\right] - \frac{(C - 1)^2}{2C - 1}\sigma^2 \quad (42)$$

in which $Y^*(\cdot)$ and $E^*(\cdot)$ are the power spectral density functions of $\{y_n\}$, the sampled analog signal, and $\{y_n - x_n\}$, the sampled error signal, respectively. Thus

$$Y^*(fW) = \sigma^2\left[1 + 2\sum_{k=1}^{\infty} \rho_k \cos\frac{\pi f}{R}\right] = \frac{1}{\tau}\sum_{n=-\infty}^{\infty} Y[W(f + 2nR)] \quad (43)$$

and

$$E^*(fW) = Q_0 + 2\sum_{k=1}^{\infty} Q_k \cos\frac{\pi f}{R}. \quad (44)$$

The sum in equation (42) of Q_0 and the infinite series is the quantizing noise at the output of an ideal low pass filter with bandwidth W Hz. The integral represents the additional noise power reduction that results from an optimal, rather than a flat, filter transfer function.

When the approximations given in equations (36) and (37) are valid, the correlation coefficients that appear in equations (41) and (44) may be approximated by

$$\begin{aligned} Q_0 &\cong \frac{\delta^2}{3} \\ Q_\mu &\cong \frac{2\delta^2}{\pi^2}\sum_{k=1}^{\infty}\frac{(-1)^{\mu k}}{k^2}\exp\left[-\frac{\pi^2 k^2(1-\rho_\mu)}{\beta^2}\right]. \end{aligned} \quad (45)$$

REFERENCES

1. Libois, L. J., "Un Nouveau Procédé de Modulation Codée 'La Modulation en Δ'," L'Onde Electrique, *32*, No. 298 (January 1952), pp. 26–31.
2. de Jager, F., "Delta Modulation, A Method of PCM Transmission Using the 1-Unit Code," Philips Research Reports, *7*, No. 6 (December 1952), pp. 442–466.
3. Winkler, M. R., "High Information Delta Modulation," IEEE International Convention Record, *11*, part 8, (1963), pp. 260–265.
4. Greefkes, J. A. and de Jager, F., "Continuous Delta Modulation," Philips Research Reports, *23*, No. 2 (April 1968), pp. 233–246.
5. Zetterberg, L. H., "A Comparison Between Delta and Pulse Code Modulation," Ericsson Technics, *11*, No. 1 (1955), pp. 95–154.
6. O'Neal, J. B., "Delta Modulation Quantizing Noise Analytical and Computer Simulation Results for Gaussian and Television Input Signals," B.S.T.J., *45*, No. 1 (January 1966), pp. 117–141.
7. Protonotarios, E. N., "Slope Overload Noise in Differential Pulse Code Modulation," B.S.T.J., *46*, No. 9 (November 1967), pp. 2119–2162.
8. Gabor, D., "Theory of Communications," Journal of IEE, *93*, Pt. III, No. 26 (November 1946), pp. 429–457.
9. van de Weg, H., "Quantizing Noise of a Single Integration Delta Modulation System with an N-Digit Code," Philips Research Reports, *8*, No. 5 (October 1953), pp. 367–385.
10. Bennett, W. R., "Spectra of Quantized Signals," B.S.T.J., *27*, No. 3 (July 1948), pp. 446–472.

11. Goodman, D. J., Delta Modulation Granular Quantizing Noise, to be published.
12. Papoulis, A., *Probability, Random Variables, and Stochastic Processes,* New York: McGraw-Hill, 1965.
13. Fleischer, P. E., "Digital Realization of Complex Transfer Functions," Simulation, *6,* No. 3 (March 1966), pp. 171–180.
14. Schaefer, D. H., "Logarithmic Compression of Binary Numbers," Proc. IRE, *49,* No. 7 (July 1961), p. 1219.

Diode Array Camera Tubes and X-ray Imaging

By ARTHUR N. CHESTER, THOMAS C. LOOMIS, and M. M. WEISS

(Manuscript received September 11, 1968)

A modification of the silicon diode array camera tube has been carried out which permits X-ray images to be displayed on a television monitor. The silicon target, 50 to 150 μm thick, serves as the tube's vacuum window. Each X-ray photon generates a large number of holes in the silicon substrate. Most of these can be usefully collected, and effective quantum efficiencies over 1000 have been measured. Absolute measurements of the spectral sensitivity have been made and show good agreement with theoretical predictions made using values of hole lifetime and surface recombination velocity obtained from optical measurements on the same target. The silicon diode array offers a number of inherent advantages in X-ray imaging compared with the conventional amorphous selenium target. Among these are greater quantum efficiency, high sensitivity, and temperature stability. The diode array sensitivity greatly exceeds that of film in this X-ray energy range (5 to 20 keV). Moreover, because the video signal current is linear as a function of X-ray photon flux over a wide dynamic range, relative intensities may be compared directly rather than necessitating densitometer measurements as does film. The performance of the many types of X-ray imaging systems in different applications is compared in some detail.

I. INTRODUCTION

The silicon diode array camera tube, developed for *Picturephone*® visual telephone service applications,[1] has proved to be a versatile device. The possibility of using the diode array target for X-ray imaging had been discussed on various occasions, but a particularly useful step was the realization by E. I. Gordon that, since each X-ray photon could produce a great number of hole-electron pairs, very high quantum efficiency might be expected in this application.[2] Sub-

sequent measurements bore out this expectation.[3, 4] There are many uses for a practical imaging device with high visual brightness, ranging from medical and biological research applications to production-line testing of silicon wafer crystal orientation.[5]

This paper describes the modification of the camera tube for X-ray imaging and measurements of spectral response obtained with such a tube. The relevant features of all the various X-ray imaging techniques are compared in the context of specific applications to identify the particular devices which are most suitable for specific purposes. This permits a balanced evaluation of the usefulness of the silicon diode array camera tube for X-ray imaging, as well as shedding light upon other possible imaging systems.

II. DESCRIPTION OF DETECTION SYSTEM

The fundamental unit of the detection system is the diode array camera tube[1] developed for the *Picturephone* visual telephone station set. Let us start with a brief summary of the operation of this tube, as it applies to X-ray detection.

The camera tube target consists of a thin disk of n-type silicon, typically 0.800 inch in diameter, whose uniform thickness may range from 0.7 mil up to several mils, depending upon the specific application.

An array of p-n diodes is formed on one side of the silicon disk by standard photolithography and diffusion. Early versions of the target used diodes of 8-μm diameter spaced on 20-μm centers, covering a rectangular area approximately 1 cm on a side. In recent versions the diode spacing is 15 μm. These dimensions are consistent with specifications for the *Picturephone* visual telephone set and are not necessarily optimum for X-ray applications.

The target substrate is maintained at a potential of 5 to 10 volts positive relative to the electron gun cathode by the target bias voltage. An electron beam is scanned across the diode array, building up a negative charge on the p-side of the diodes until that surface of the target is charged down to cathode potential; then additional arriving electrons are repelled and do not land on the target (these are collected at another electrode, the collector). Under these conditions the diodes are reverse-biased, and in the absence of light will store their charge for a long time. The storage time is limited by diode leakage current. The amount of charge that leaks off between the successive times that the electron beam accesses a given diode (the frame time)

is replaced when the electron beam reaches that diode again. The associated charging current constitutes the video signal. The charging current observed when the target is not illuminated is called the dark current.

The detection ability of the diode array arises because the rate at which the diodes discharge can be greatly accelerated by various means. For *Picturephone* visual telephone service applications, an optical image is focused on the side of the silicon disk opposite the diodes. Photons create hole-electron pairs in the substrate; the holes diffuse to the nearest diodes and are swept across the space charge region, partially discharging the diodes. For X-ray detection, an X-ray photon is absorbed by a substrate atom, producing a fast electron carrying most of the original photon energy.[6] This electron creates many hole-electron pairs as it decelerates, losing its energy in a distance of no more than a few μm.[7] The resulting holes diffuse to adjacent diodes and discharge them. In either case, a video signal will be produced when the electron beam accesses those portions of the target which have been discharged by exposure to light or X-rays.

In the present work, the diode array was scanned in 275 horizontal lines; the frame time (the time required to scan all diodes once) was 1/30 second. The video bandwidth was about 1 MHz, and the picture was displayed on a TV monitor .

Provision was also made for blanking off the electron beam, allowing only every Nth frame to be read. This technique, described as "N:1 frame delay," allows the diodes longer between sweeps to lose charge in response to X-ray flux; thus within limits it increases the magnitude of the video signal obtained by increasing the integration time of the camera tube. This is simply analogous to using a longer exposure time in photographic work. The result is increased contrast in the displayed image.

The normal diode leakage current is also integrated; however, the extra dark current signal that results is not deleterious for storage times up to $\approx$1 sec. After a sufficiently long delay all diodes will discharge completely because of leakage, regardless of X-ray signal; thus excessive frame delay reduces picture contrast. The other undesirable feature of excessive frame delay is that moving objects will blur when frame delay is too long. In the early stages of the experiment, very long frame delays were subjectively unpleasant to use because the picture would only be displayed a few times a second, leading to flicker; however, this effect has now been minimized by using a long-persistence cathode-ray-tube in the monitor and could

be eliminated completely by using a storage tube for repetitive display of the same frame.

The diode array target is ordinarily mounted inside the camera tube vacuum envelope behind a glass window 0.100 inch thick. Since that thickness of glass would have introduced excessive attenuation of X-radiation, for X-ray use the tubes were assembled without mounting a diode array in the tube. The glass window of the tube was replaced with a copper plate in which a hole of ⅜ inch diameter was drilled. The diode array target was attached to the outside of the window, covering this hole, with Delta-Bond adhesive,* a high-temperature epoxy with clean vacuum characteristics. The tube was processed at a temperature of 190°C. Thus the diode array target itself served as the tube window and had to support the tube vacuum against atmospheric pressure. The target used in this work had a mechanically measured thickness ranging from 0.0104 to 0.0109 cm and a phosphorous diffusion at the back surface to reduce the hole recombination velocity at the surface. Because of dimpling in the target, resulting from the pressure difference, and the lack of beveling around the hole, causing distortion in the electric field between the last focusing element and the target, the electron beam could only provide uniform sensitivity over an area about ¼ inch in diameter on the target. Other tubes have now been constructed which avoid target distortion by using a beryllium or mylar window to hold the vacuum, allowing the target to be mounted inside the tube more or less conventionally. The usable sensitive area of the target in such tubes is the size of the entire diode array (1.34 × 1.34 cm in the present design).

III. CALIBRATION OF A MONOCHROMATIC HIGH-INTENSITY X-RAY SOURCE

A fluorescence X-ray tube with a copper anode was used to excite characteristic X-radiation from nine different samples, ranging in atomic number from vanadium to tellurium, as indicated in Table I. This radiation passed through a brass collimator 4 inches long with a 3/16 inch inside diameter, into which brass tubes of smaller inside diameter could be inserted to provide further collimation. The detector was positioned so that its window was 2.01 cm from the collimator. To reduce the energy spread of the resulting radiation an appropriate absorbing foil was introduced into the output beam, consisting of an element with a critical absorption energy just above the $K\alpha$ lines of

* Wakefield Engineering, Inc., Wakefield, Mass.

TABLE I—COMBINATIONS OF RADIATORS AND ABSORBING FOILS USED

Radiator			Foil			Representative Calculated Values of Photon Flux Using 40 mA Tube Current, Full Wave Rectification, with an Aperture of the Indicated Diameter		
	X-ray Fluorescence, keV							
Material	$K\alpha_1$	$K\alpha_2$	Thickness inches	Material	Absorption Edge, keV	0.020" photons/min	2.21 mm photons/sec	Peak Voltage kV
V	4.952	4.944	0.0016	Ti	4.964	456301	577139	40
Co	6.930	6.915	0.0028	Fe	7.111	314037	397200	40
Zn	8.638	8.615	0.0018	Cu	8.980	236438	299052	40
As	10.543	10.507	0.0042	Ge	11.103	157273	198922	40
Zr	15.774	15.690	0.0026	Y	17.037	419462	530544	40
Mo	17.478	17.373	0.0052	Zr	17.998	259854	328669	50
Pd	21.175	21.018	0.0057	Rh	23.224	87328	110454	50
Sn	25.270	25.042	0.0060	Ag	25.517	119537	151193	50
Te	27.471	27.200	0.0049	Sn	29.190	172146	217734	50

the radiator being used. It was determined by using a proportional counter with a multichannel pulse-height analyzer that the absorbing foil removed not only a great deal of X-radiation at lower energies, but also greatly attenuated the $K\beta$ lines produced by the radiator. Thus the transmitted radiation was essentially monochromatic, consisting only of the $K\alpha$ lines of the radiator being used, and ranged in energy from 4.95 keV (2.5 Å wavelength) to 27.3 keV (0.45 Å wavelength).

Once combinations of radiators and foils had been selected to provide X-radiation only in narrow spectral ranges, it was necessary to calibrate the absolute intensity of the output beam. This was done using a scintillation counter with a Siemens GS-DM ZO/B X-ray detector. By using a cobalt radiator with varying numbers of 0.003 inch aluminum absorbing foils, it was determined that this detection system reads 1 percent too low because of counter dead time loss at a count rate of 300,000 per minute; apertures were therefore chosen to keep all count rates on the Siemens detector below this level for the remainder of the measurements.

The detector used for calibration was a General Electric SPG 4 scintillation counter. The counting efficiencies used were calculated for a NaI crystal of nominal thickness 0.040 inch. Experiments are under way to establish an accurate experimental efficiency curve for this detector.[8] The efficiency of the Siemens detector was determined by comparison with the GE detector, using a crystal monochromator source, and was found to vary from 60.1 percent at vanadium to 88.6 percent at tellurium. The peak efficiency was 90.5 percent for cadmium $K\alpha$; the efficiency was above 79 percent for all the wavelengths subsequently used except the vanadium $K\alpha$.

Measurements were then made of the photons per second issuing from an aperture of diameter 0.020 inch for tube currents of 40, 11, and $\approx$2 mA, using a full-wave rectified power source, with peak tube voltages of 40 and 50 kV. Background intensities were subtracted in all cases. The statistical precision of these measurements was adequate to give a fractional standard deviation ($N^{-1/2}$) of 0.003 or less for each wavelength.[9]

In order to provide more X-ray intensity for detection by the silicon camera tube, a series of apertures of increasing size was used, finally arriving at an aperture 2.21 mm in diameter. The proportional counter was used to obtain intensity ratios between various apertures, and the final value for the intensity using the 2.21-mm aperture relative to that using the 0.020 inch aperture was determined to be 75.9,

with a calculated statistical precision of 3.5 percent. The maximum calibrated intensity available varied from 110,000 to 577,000 photons per second, depending upon the X-ray energy, as indicated in Table I.

The particular combination of aperture, radiators, foil filters, detector distance, and X-ray source measured thus provides a variable-energy monochromatic output of known intensity. If the instability of the power supply-detector combination is taken to be 0.2 percent, this indicates that the relative intensities available at different energies are known with a standard deviation of 0.36 percent, and the absolute intensity at any given wavelength is known with a standard deviation of 3.5 percent.

IV. MEASURED X-RAY SPECTRAL RESPONSE AND SENSITIVITY

The camera tube was mounted with its diode array target 2.01 cm from the 2.21-mm aperture and the X-ray beam was chopped at 13 cps using a lead chopper blade. The video signal was synchronously detected to provide greater measurement accuracy. It was verified that the video signal obtained did not change when the size of the scanned area on the diode array was increased. The magnitude of the 13-cps signal was compared with the video signal measured with a dc meter without chopping the X-ray beam; the rms deviation in this calibration factor was found to be 3.8 percent. This introduces an error in the absolute scale of the measurements, in addition to the 3.5 percent resulting from errors in measuring intensity ratios using different apertures.

The noise in the synchronous detector signal had an rms value of 0.2 microvolts. An X-ray beam whose intensity was just sufficient to give a signal on the synchronous detector equal to this noise level, if directed onto the camera tube without chopping, would have given a dc video current of 0.79 pA. Since video currents of about a nanoampere were required to produce a strong image on the monitor with the beam size used here, many of the X-ray intensities measured therefore did not produce a visible spot on the monitor. The error bars indicated in the graphs indicate the range of values represented by this error of 0.2 microvolts, since the 0.36 percent error in the relative calibration of the X-ray source was too small to affect the accuracy of these measurements. The overall presumed accuracy of $[(3.5)^2 + (3.8)^2]^{1/2} = 5.2$ percent is not indicated in the figures but should apply to the absolute magnitude of the measurements.

Figure 1 indicates the dc response of the diode array camera tube

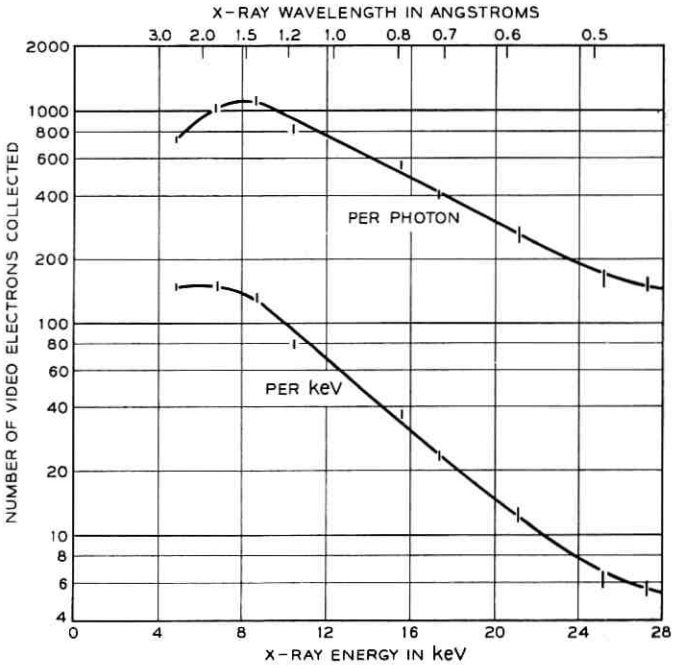

Fig. 1 — Video electrons collected by tube No. TN-84 as a function of incident X-ray energy.

as deduced from the synchronous detector measurements. Since the number of hole-electron pairs produced when an X-ray photon is absorbed is a linear function of the available photon energy, it was felt that it was most meaningful to plot numbers of collected electrons as a function of photon energy rather than photon wavelength. Figure 1 gives the number of video electrons collected per incident X-ray photon and per keV of incident X-ray photon energy.

V. DETERMINATION OF TARGET SUBSTRATE PARAMETERS

In order to extract information more indicative of the physical processes leading to the X-ray detection, some further processing of this data is necessary. If information can be extracted about the intrinsic quantum efficiency of the detection process, then the practical performance of diode array targets of various thicknesses and various physical properties can be estimated. In this section the hole lifetime and surface recombination velocity are determined for the target used in our experiments.

One piece of information necessary for this computation is the absorption coefficient of the diode array target for the various wavelengths of X-rays used. This information is well known, and for this work was taken from a table published by Philips Electronic Instruments.[10]

It is also necessary to know the distribution in position of the holes generated in the silicon when an X-ray photon is absorbed. This is relatively simple to determine under the assumption that the X-ray photon upon absorption produces a very fast electron carrying most of the photon's energy; this electron then produces many hole-electron pairs as it loses energy. The rate of production of the fast electrons decreases exponentially with distance as the X-ray beam is absorbed; thus the rate of hole production will also have this exponential profile, spread out slightly by the range of the fast electrons in the silicon substrate. However, an estimate of the range of fast electrons of the appropriate energy yields values less than 5 percent of the 1/e absorption distance for X-rays in silicon in the energy range treated here. Thus a hole production rate that decays exponentially with distance will be assumed in this energy range.

The last piece of information that is needed is the fraction of holes generated that are collected by the diode and thus lead to a video signal, for the exponentially decaying hole generation rate previously obtained. This can be determined fairly well as follows. The absorption mechanism for photons in the near infrared is primarily hole-electron pair formation, the photon energy involved being sufficiently small that only one hole can be produced per photon absorbed. Moreover, different hole generation geometries can be obtained since the absorption coefficient of the silicon varies as a function of wavelength. To duplicate the X-ray absorption depths relevant to the measurements reported here, it would be necessary to use infrared light varying in wavelength from 0.87 to 1.11 microns.[11]

However, even though light and X-radiation are chosen having the same absorption depth in silicon, the hole generation geometry may differ in the two cases. Unless the absorption coefficient is sufficiently great that virtually all of the light is absorbed in a single pass through the target substrate, light will be reflected from the surface at which the diodes are located, changing the simple exponential spatial dependence of the hole generation rate to some more complicated form, and making the hole generation geometry different for the light and the X-rays. Since absorption and optical interference are known to take place[12] in the oxide-resistive overlay region, even

the reflectivity of the diode surface of the substrate is complicated and wavelength-dependent.

Crowell and Labuda have developed a recombination-diffusion model for hole collection in a diode array target which is valid for light in the visible part of the spectrum, where multiple internal reflections may be ignored.[13] The measured optical collection efficiency of the diode array target in this wavelength range can be used to determine sufficiently accurately the two parameters required in this model, namely, the hole lifetime in the substrate and the hole recombination velocity at the illuminated side of the target. Although the collection efficiency predicted by the model becomes invalid when applied to infrared light, it is perfectly valid for X-rays of all wavelengths, since X-radiation maintains the exponential hole generation geometry regardless of the absorption of the substrate because the X-rays are not appreciably reflected at the surfaces of the silicon. Crowell and Labuda's collection efficiency model was applied to the X-ray camera tube to determine the necessary target parameters.

First, measurements were made of the number of video electrons collected per incident photon for light in the wavelength range 0.46 to 1.15 microns. Since A. J. Chick's computer calculations of the collection efficiency predicted by Crowell and Labuda's theory did not include the effects of reflection at the silicon-air interface and the "dead layer"[14, 15] at the illuminated side of the silicon target, the measured collection efficiency was corrected before comparing with the theoretical curves.

The measured collection efficiency was first multiplied by a factor, $\exp(+\alpha L_d)$, to eliminate effects resulting from absorption in a "dead layer" of thickness $L_d = 0.2$ μm. The absorption coefficient α of silicon for visible light was taken from published data.[11] The measured collection efficiency was further increased by $1/(1 - R)$ to correct for reflection at the silicon surface, using published values of the reflectivity of silicon.[16] This yielded the open data points shown in Fig. 2, which represent as accurately as possible the number of video electrons collected per optical photon passing through the dead layer into the active region of the substrate.

The reflectivity of the diode array was measured, as described in the Appendix, to verify that the reflectivity corrections being made were accurate. If the measured values of reflectivity are used to obtain the collection efficiency for wavelengths greater than 1 μm in Fig. 2, the two solid data points are obtained. However, Crowell and Labuda's theory neglects internal reflections. Thus the corrected values of col-

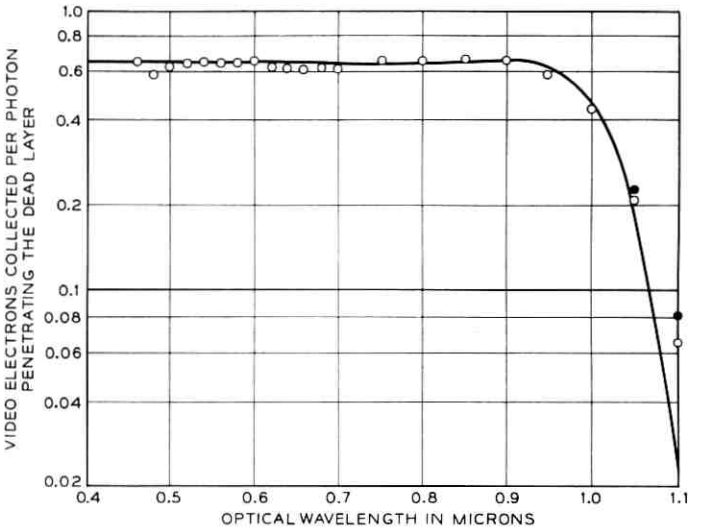

Fig. 2 — The data points represent measured values of collection efficiency for tube No. TN-84, corrected for reflectivity and dead layer absorption as discussed in the text. The solid data points use measured values of reflectivity rather than published values. The solid curve gives the predictions of Labuda's theory, which is expected to be valid only at wavelengths shorter than $\approx 0.93 \mu m$ because of its neglect of internal reflections.

lection efficiency shown in Fig. 2 may be used only at sufficiently short wavelengths such that the exponential hole profile within the substrate caused by the incident photons is not distorted by internal reflection from the diode surface of the target. To keep the intensity of light arriving at the diodes below 5 percent of that entering the target, the target thickness must be about three times the $1/e$ absorption depth. In the present target, with thickness of about 0.0107 cm, this requires considering in Fig. 2 only those wavelengths shorter than ≈ 0.93 μm.

The predictions of Crowell and Labuda's theory were then calculated for various values of hole lifetime τ and surface recombination velocity S. The depletion layer depth was taken to be 5 μm, a typical value for the conditions of vidicon operation (substrate resistivity 10 ohm-cm, target voltage 5–10 volts).[17] The theoretical predictions were compared with the experimental data as follows.

Computed collection efficiency curves were drawn for a large number of values of S, ranging from 50 to 1000 cm per second, with τ ranging from 5 μsec to 10 msec. These ranges of values were known from previous work to include any values of the parameters which

might be encountered. The values of the collection efficiency at 0.50 μm wavelength and at its maximum were found to give good discrimination between the curves, and the values of S(cm/sec), τ(μsec) selected for further comparison were: (50, 11), (70, 12), (100, 12), (100, 13), (140, 13), and (140, 14). The rms deviations of these curves from the measured values (with oscillatory behavior removed as discussed in the Appendix) were calculated for wavelengths 0.50, 0.65, 0.80, and 0.90 μm, and the maximum value. Only one curve was found to agree within one averaged deviation at as many as four of these points; moreover, at the remaining point it was still only 1.35 averaged derivations away from the measured value.

The values determined by selecting this curve as the best fit were $\tau = 12(\pm 0.5)$ μsec and $S = 70(-10, +15)$ cm per second. This is shown as the solid curve in Fig. 2. The uncertainties quoted assume a probable error of half the interval to the next closest values of S or τ examined. These values are consistent with the values $\tau = 10$ μsec, $S \approx 50$ cm per second found by Buck, Casey, Dalton, and Yamin in similar diode array targets.[14] The hole diffusion coefficient D in silicon has been taken as 10 cm^2 per second[18].

VI. CALCULATED SPECTRAL RESPONSE OF DIODE ARRAY TARGETS

Using the values determined above for the hole lifetime and surface recombination velocity, a predicted X-ray quantum efficiency may be calculated for comparison with the measured values in Fig. 1. This is done for a variety of target thicknesses to provide an estimate of how the collection efficiency would be expected to change with target thickness, since it would be desirable for many applications to extend the spectral response to higher X-ray photon energies.

First, an upper limit to the number of video electrons collected per incident photon may be calculated, which will ultimately limit the performance of any silicon diode array target which does not incorporate heavier elements in substantial quantities. This is obtained by assuming that the holes produced by every X-ray quantum absorbed in the target are all collected, so that the limitation on quantum efficiency at low energies is the smaller energy per photon available for making hole-electron pairs, and at higher energies is the lack of absorption of these X-ray photons by silicon. Specifically, the fraction of X-ray photons absorbed by the target is obtained using published X-ray absorption coefficients for silicon.[10] It is then assumed that each 3.50 eV of energy in an absorbed photon leads

to a video electron. Such a calculation is consistent with a model which assumes that virtually all of the photon energy is transferred to an electron upon absorption; this fast electron produces hole-electron pairs as it decelerates (expending for each pair the value 3.50 eV),[19] all of the resulting holes are collected.

Such a calculation leads to the collection efficiency curves in Fig. 3, which give an upper limit to the quantum efficiency that could be anticipated using any target principally composed of silicon. The rise in collection efficiency in the 100 keV range occurs because the absorption coefficient of silicon, which drops approximately as E^{-3}

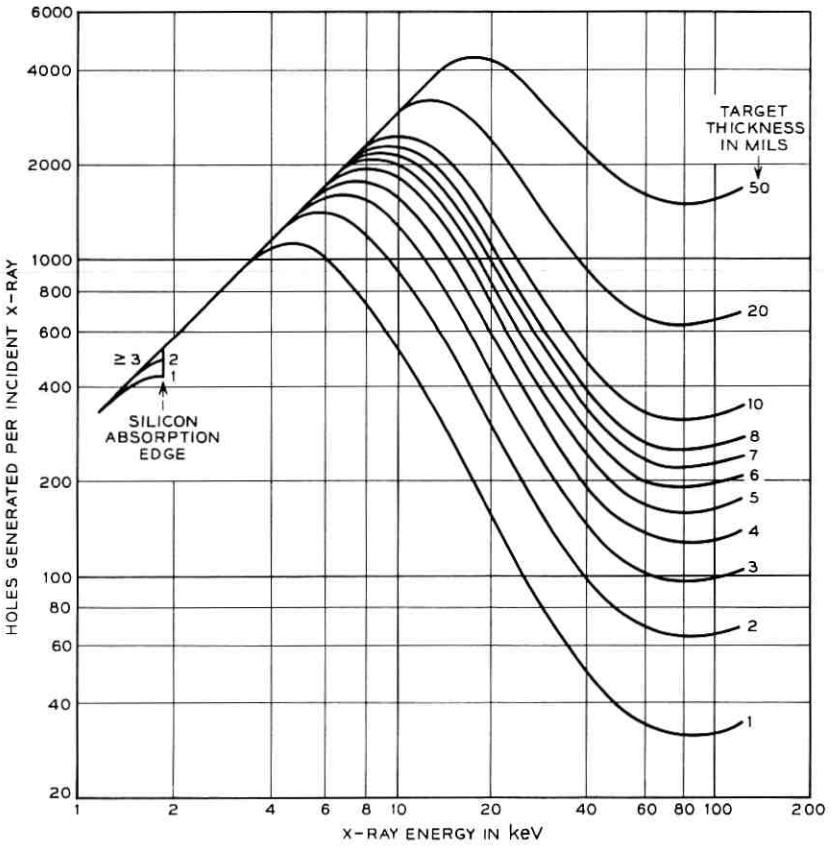

Fig. 3 — Maximum number of holes that could be generated per X-ray photon incident upon silicon targets having the indicated thickness, as a function of X-ray energy.

for X-ray energies in the range 2 to 30 keV, drops less rapidly at higher energies, falling at a rate slower than $1/E$ above 85 keV. This slower drop is more than compensated for by the greater energy available per photon which, of course, rises linearly with E. However, since this increased absorption occurs from Compton scattering rather than the photoelectric effect,[6] it may be less efficient at producing hole-electron pairs.

The additional information, provided by the values $\tau = 12$ μsec and $S = 70$ cm per second obtained in the previous section, permit more specific calculations to be made for the conventional type of diode array target having a "dead layer" of thickness 0.2 μm, with holes generated in the substrate either diffusing to a diode and being collected, recombining in the volume, or diffusing to the illuminated side of the target and recombining with electrons without leading to a video signal. The depletion layer thickness will again be assumed to be 5 μm.

The calculation is made using Crowell and Labuba's collection efficiency theory, corrected for the presence of the dead layer, again assuming that every 3.50 eV of absorbed X-ray energy leads to the production of a hole. A computer program by A. J. Chick using this theory leads to the curves in Fig. 4, which predicts the actual X-ray collection efficiency that should be observed using silicon diode array targets of various thicknesses, with the substrate parameters taken to be $\tau = 12$ μsec, $S = 70$ cm per second.

Notice that the target thickness yielding the greatest collection efficiency is about one hole diffusion length L_D in thickness, since $L_D = (D\tau)^{\frac{1}{2}} \approx 4$ mils. The experimental points indicated in Fig. 4 for tube No. TN-84, with target thickness 4 mils, are $\approx$20 percent lower than the calculated values. This discrepancy may arise from error in estimating the dead layer thickness, lack of accurate experimental calibration of the X-ray source, and neglect of excess recombination[20] in the theoretical treatment. Other contributing factors may be electrons lost by photoemission at either surface of the target and a ± 5 percent uncertainty in the mechanical measurement of the target thickness.

One final curve of some interest is the quotient of the theoretical predictions of Figs. 4 and 3. Since Fig. 3 gives essentially the total number of holes generated per incident photon and Fig. 4 gives the number of electrons collected per incident photon, the quotient of these values is the fraction of generated holes which are usefully collected by the diodes. This number, referred to here as the "geometrical efficiency" of the target, depends only upon the geometry of

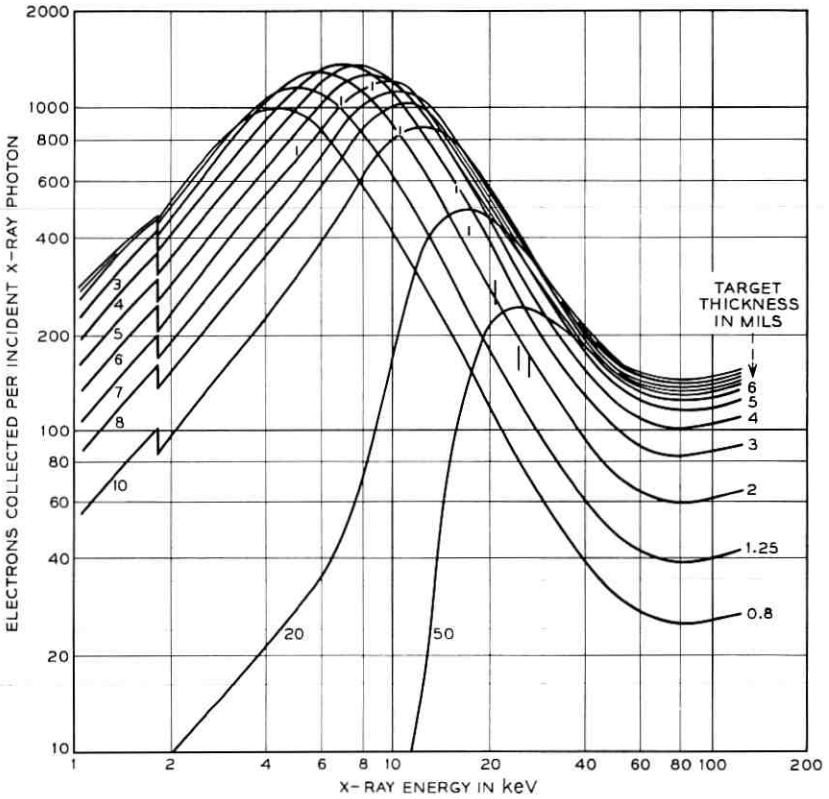

Fig. 4 — Collection efficiency for X rays as a function of X-ray energy, predicted by theory. Values measured for tube No. TN-84 are indicated.

the collection: absorption coefficient, substrate parameters, and target geometry. It is shown in Fig. 5 as a function of absorption coefficient, and the values presented apply to both X-ray detection and visible light detection, so long as the exponential hole generation geometry is maintained. Corresponding X-ray energies and optical wavelengths are indicated in the figure. As expected, the geometrical efficiency asymptotes to its maximum value when the absorption coefficient becomes so small that the hole generation is essentially uniform throughout the target volume.

VII. COMPARATIVE EVALUATION OF VARIOUS X-RAY IMAGING TECHNIQUES

The X-ray imaging devices known to the authors may be classified into the following categories:

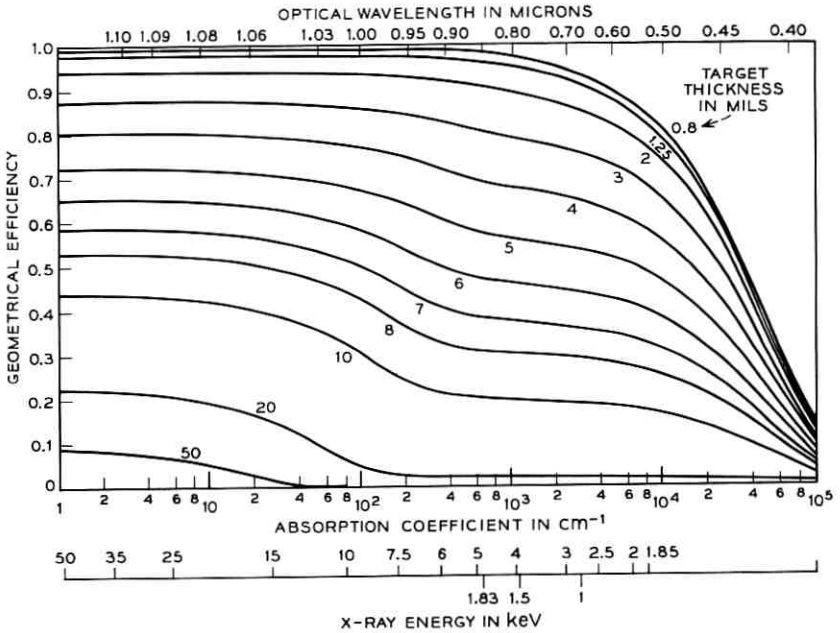

Fig. 5 — Geometrical efficiency of silicon targets of various thicknesses for visible light and X-radiation, assuming a dead layer of 0.2μm and strictly exponential hole generation.

(*i*) Film—Film may be directly sensitive to X-radiation or make use of a phosphor screen placed in close contact with the film.

(*ii*) Direct fluoroscopy—A fluorescent screen is viewed directly by a dark-adapted observer.

(*iii*) Image-intensified fluoroscopy—Systems in this category seem to have the common feature that image amplification occurs without dissecting the image sequentially. A conventional technique of this type uses a fluorescent screen in intimate contact with a photoemitter, taking the emitted electrons by electron focusing and minification to produce a brighter image on a cathodoluminiscent phosphor screen, which in turn may be viewed directly or imaged with a television system first. In this category would fall direct photoemission by X-rays, with later electron imaging. Another modification would replace the electron imaging stage by a solid-state image intensifier.

(*iv*) Flying spot tubes—A collimated X-ray beam is periodically scanned across an object to be examined, and a detector of high counting efficiency collects essentially all photons penetrating the

object. Although this is strictly speaking not an imaging system, it serves the same function for certain applications (for example, medical and radiographic) and therefore is to be considered competitive for such applications.

(*v*) Scanned-image camera tubes—These systems use sequential image dissection with subsequent electronic amplification. The tubes that have been constructed of this type use an electron beam to scan a photosensitive surface, usually a photoconductor. The diode array camera tube is in this category.

Qualitative comparisons among some of these systems have been given in the past.[21-30] The present discussion will be more quantitative and relate to specific practical applications.

7.1 *Microscopy*

The resolution element d is defined so that the modulation transfer function of the system is 50 percent at a spatial frequency of $1/2d$ line pairs per unit distance. The resolution obtainable with standard X-ray film is about a μm,[31, 32] and films of finer grain are available. Although film does not permit real-time viewing, it is still the most convenient choice for many applications, and can be used for motion studies by using a movie camera or a rotating film drum. The resolution of fluoroscopic screens ranges from 0.4 to 0.7 mm;[22, 29, 33-35] these are inappropriate for very fine imaging.

In scanned-image camera tubes a practical limitation likely to be encountered is bandwidth and electron beam spot size. Bandwidth is not too severe a limitation upon resolution, since it only limits the number of resolution elements in the picture (for a fixed frame time) rather than their size. Thus, finer detail may be observed at the sacrifice of viewing a smaller area of the image.

The limitation on electron beam spot size is more basic but again tradeoffs can be made. From Pierce,[36] the current density at a picture element, assuming an ideal lens, is

$$j_{spot} = j_{cathode}(1 + \Phi) \sin^2 \theta. \tag{1}$$

In this equation,

$$\Phi = eV/kT, \tag{2}$$

with V the target potential with respect to the cathode and T the cathode temperature. θ is the maximum angle with respect to the target normal which the paths of arriving electrons make, and $j_{cathode}$ is the

emission current density at the cathode. For an approximate calculation one may take $V \approx 1$ volt, and $kT/e \approx 0.1$ volt, so that $1 + \Phi \approx 10$. In practical devices an appropriate value is $\sin \theta = 0.1$. The current density available from a CPC cathode (a typical choice for diode array camera tubes) as measured by MacNair is $j_{\text{cathode}} = 2.5$ A/cm^2;[37] this cannot be bettered by more than about a factor of four, and then only at the expnse of operating lifetime.[37] Thus a practical limitation is

$$j_{\text{spot}} = i_{\max}/d^2 \approx 0.25 \text{ A/cm}^2. \tag{3}$$

For example, in tubes now available the maximum beam current is about $i_{\max} = 6$ μA, giving a minimum spot size of $d \approx 50$ μm, which agrees approximately with experience.[38]

In an electron beam scanned device, therefore, a spot size $d = 5$ μm, according to these considerations, permits only the relatively small amount of beam current $i_{\max} = 60$ nA; because of secondary electron emission, the maximum signal current available is still less. Practical difficulties in design, because of nonideal imaging, may make such small spot sizes hard to achieve. Thus, dynamic range must be sacrificed to get very high resolution with such a device.

The problem of lateral diffusion of carriers is particularly troublesome in connection with high resolution camera tubes. In the case of a diode array device there is virtually no electric field in the target substrate and carriers simply diffuse to the diodes. For an $S = 0$ surface[13] and lower energy X-rays, with the carriers generated near the surface, the carriers will, on the average, diffuse laterally a distance equal to the thickness t of the target while they diffuse an equal distance t to the depletion region of the diode. This lateral spread would give a picture element of approximate size $d = 2t$. This will only be slightly reduced (to perhaps $1.5t$) for X-rays of higher energy, even when a finite surface recombination velocity is taken into account. Since the minimum thickness for a self-supported target is about 10 μm at present, the attainable resolution for such a target is only about 15-20 μm. Higher resolution would probably suggest a thinner target, mounted on a beryllium entrance window. Similar considerations apply to other possible target materials, such as amorphous selenium,* PbO, or CdS (See Refs. 39 and 40, 21 and 41, and 21, respectively). However, these latter materials are not generally fabricated to be self-supported as is the diode array target.

Another effect that can be of some importance in determining the

* Westinghouse Type WX-5129 X-Ray Vidicon, Westinghouse Electric Corporation, Electronic Tube Division, Elmira, N. Y.

resolution arises from the nature of the primary photoprocess. Since a single fast photoelectron is produced when an X-ray quantum is absorbed, and since the velocity of that electron may have any direction with respect to the direction of photon incidence, the finite range of that electron's energy loss means that carriers are produced approximately throughout a sphere whose radius is the range of the hot electron in the substrate. The resolution element d will be taken to the diameter of that sphere. For example, in silicon an approximate value is[7]

$$d = 0.028[E(\text{keV})]^{1.65}\ \mu\text{m}. \tag{4}$$

This formula is quoted as having validity in the range 2 to 20 keV.[7] Since a similar formula given for the range of electrons in aluminum (only one less in atomic number than silicon) yields a value for range of 32.3 μm at 100 keV, not too far different from the measured value $\approx$55 μm,[42] it is reasonable to expect that the expression for silicon also retains validity to higher energies than 20 keV. This would indicate, in the case of silicon, a picture element of size $d = 3.9$ μm at 20 keV, increasing to 23.8 μm at 60 keV. The range for electrons would be expected to be smaller[42] for heavier target materials such as selenium, CdS, or PbO.

Finally, it is also possible that such effects as generation of secondary X-radiation and Compton scattering could impair resolution, especially at energies above 50 keV; these might have to be considered in the design of a very high-resolution camera tube.

The X-ray camera tube in its present form has an estimated resolution of about 25 μm. Depending upon the energy and intensity of the X-rays to be detected, the foregoing discussion indicates that this probably cannot be reduced to less than 5 or 10 μm in a camera tube of this type.

7.2 *Medical Applications*

For medical imaging applications it is desirable to have a large sensitive area (at least 6″, preferably 12″ in diameter)[34, 43, 44] and good video response to high energy X-rays, a typical effective X-ray energy being 60 keV. The former constraint does not apply to dental work. In addition, it is particularly necessary to minimize the dose to the patient by making effective use of as many incident X-ray photons as possible.

Film meets all these requirements most effectively when only a single picture needs to be made and when development time is not a

consideration. However, it is not practical for motion studies because of the inconvenience of sequentially exposing such large areas on successive frames of film.

Although direct fluoroscopy is very efficient in producing an optical image from the incident X-radiation, the eye is an inefficient gatherer of light and thus loses much of the advantage gained by the high quantum efficiency of the fluorescent screen.[22-24] Although the fraction f of usefully absorbed photons may be as high as 0.65, so that the majority of the incident X-ray photons are effective in producing visible quanta, each incident X-ray photon leads only to $\leqq 10^{-3}$ optical photons at the retina of the eye, so the effective f of the system must be taken to be this much smaller value.[22,24] Since this fraction f determines the amount of information transmitted by the detected photons, as pointed out by Rose,[45] for an f of 10^{-3} the statistical fluctuations in the detected signal are so great that only one-thousandth of the information contained in the incident photon flux is transmitted through the detection system.

When an image intensifier is used, the number of quanta per picture element never falls below the number originally usefully absorbed; the various stages of transmitting the picture information in the image intensifier system only act to increase the number of quanta per picture element, and even with the inefficiency of the eye's optics the number of photons reaching the retina is typically still an order of magnitude higher than the number of X-ray photons usefully absorbed.[22] Values of f for an image intensifier system could be as high as ≈ 0.65, depending upon X-ray photon energy, since the primary photoprocess uses this fraction of incident photons in direct fluoroscopy. However, in practice, thinner fluorescent screens are used in order to improve the resolving power of the system. Depending upon the energy of X-rays and the resolution required, values of f from 0.01 to 0.55 (but usually below 0.1) have been reported in these systems.[22, 24, 29, 46, 47] A useful compromise providing better resolution than direct fluoroscopy but still having a much higher effective f might be estimated to have $f = 0.1$.

Notice that with $f = 0.1$ only one photon in ten is detected. Thus even though the image intensifier display exhibits genuine quantum noise, it should be possible to reduce the dose to the patient a factor of ten without impairing the picture quality.

In addition to the present work, the usefulness of the silicon diode array camera tube for detecting X-rays in this energy range ($\approx$60 keV) has been demonstrated by Harpster and Jacoby.[48] To compute the

efficiency of the silicon tube and other photoconductive camera tubes (using PbO, CdS, and Se targets), it is first necessary to discuss some aspects of camera tubes using photoconducting targets. It has been shown, for example by Rose[49,50] and by Redington,[51] that the requirements of short response time (low "lag"), low dark current, and high photoconductive gain (referred to here as the geometrical efficiency g) cannot be simultaneously satisfied using ohmic contacts. The only way to keep g fairly large consistently with the other requirements is to use "blocking" contacts. Since these do not inject additional carriers from the electrodes the dark current can thus be kept acceptably low.

When a blocking contact is used, there is a depletion region adjacent to the contact, across which appears the voltage drop which is applied to the target. Carriers generated in this region are efficiently collected because of the electric field present, but carriers generated outside this region must diffuse to the depletion region before recombining if they are to be collected. Although the width of the depletion region can be widened by increasing the target voltage, in practice it is not generally possible to extend the depletion region throughout the target thickness because carrier injection will occur at higher voltages. This carrier injection increases dark current, and makes the contact effectively ohmic rather than blocking. Thus, although contacts to amorphous selenium X-ray vidicon targets are blocking in nature, the width of the depletion region is sufficiently small that most carriers are collected by diffusion rather than by being swept through a region by an electric field. This would explain why the optimum target thickness reported by Smith[40] was approximately equal to the carrier diffusion length, and is also consistent with depletion layer thicknesses discussed by Rose[49] and van den Broek.[52]

Since blocking contacts have been achieved in PbO,[52] amorphous selenium,[49] and CdS,[53] it is certainly possible to construct X-ray camera tubes, using such target materials, in which carriers are collected by diffusion to the electrodes, although the fabrication of the contacts may give some practical difficulty. Therefore such camera tubes can be easily compared with the silicon diode array tube since the method of carrier collection is similar and the same restraints that apply to the silicon tube (limited target thickness to prevent lateral diffusion of carriers and consequent resolution loss, and to prevent loss of carriers by volume recombination before collection) will also apply to these tubes.

If blocking contacts can be maintained at sufficiently high voltages that the depletion region can be extended through the target thick-

ness, the sensitivity will be much greater than estimated here. Such contacts were apparently not obtained in the work reported by Smith on amorphous selenium targets.[40] In the case of PbO films, the authors are not aware of X-ray measurements reported in sufficient detail to determine the mechanism of carrier collection.

The applicability of various camera tube targets to medical X-ray detection can be assessed under the assumption that the generated carriers diffuse to the target surface and are collected there. The targets will be assumed to be as thick as possible so that as much of the incident radiation as possible can be used. Specifically, the target thickness will be taken to be ten times the diffusion length for minority carriers in the particular substrate being considered. This is as thick as can be allowed if each absorbed photon is to produce at least several collectable carriers, since $e^{-10} \approx 10^{-4}$ and since a 60 keV photon produces around 10^4 carriers in each of these materials. In any case, this manner of choosing the thickness is sufficiently general to provide some sort of meaningful comparison, particularly since the geometrical efficiency g should be similar for all four types of targets, as discussed in connection with Table III. A comparison of these types of camera tubes appears in Table II.

According to results obtained in Section 7.1, the resolution of such camera tubes would be expected to be better than the 0.4 mm obtainable with fluorescent screens, since such screens are subject to lateral

TABLE II — COMPARISON OF CAMERA TUBES FOR MEDICAL APPLICATIONS

Substrate Material	Diffusion Length μm	Target Thickness μm	X-ray Photon Energy			
			40 keV		60 keV	
			α, μm^{-1}	f	α, μm^{-1}	f
PbO (tetragonal)	1.2*	12	0.0132†	0.147	0.00492†	0.0573
Se (amorphous)	10‡	100	0.00365§	0.306	0.00115§	0.109
CdS (n-type)	6.4¶	64	0.00703†	0.362	0.00256†	0.151
Si (n-type)	110||	1100	0.000176§	0.176	0.00008§	0.084

* See Ref. 56.
† See Ref. 57.
‡ See Ref. 40, p. 352.
§ See Ref. 10.
¶ Reported values differ by about a factor of two, but the value given here is typical. It is obtained from the equation $L = (D\tau)^{1/2}$ using a hole diffusion constant $D = 0.27$ cm²/sec and hole lifetime $\tau = 1.5$ μsec. These values are given by I. Broser, *Physics and Chemistry of II-VI Compounds*, ed. M. Aven and J. S. Prener, New York: John Wiley and Sons—Interscience, 1967, p. 520.
|| Calculated from measurements reported in Fig. 2 of this paper.

light scattering. The values of absorption coefficient α for X-rays, as indicated, are given in inverse μm. The fraction of photons usefully detected is taken to be simply $f = 1 - \exp(-\alpha t)$ for thickness t.

The table indicates that only using CdS in a scanned image tube offers hope of improvement in usable fraction f over conventional optical image-intensifier systems as long as carrier collection depends upon diffusion. Its combination of high density and ease of fabrication makes it a possible candidate for medical applications. A silicon target has not only the disadvantage of a lower f, but the problems connected with a higher dark current, as discussed in the following section.

However, the very best imaging device for medical applications remains the final possibility considered here, the flying spot X-ray system. Although the production of X-radiation by such a system is necessarily very inefficient, about 90 percent of the photons transmitted by the patient can be detected with certainty, and thus this system is to be preferred if cutting the dose to the patient is the principal consideration. However, the practical difficulties of producing sufficient X-ray intensity in a scanned X-ray beam seem to still remain an essential limitation to the method. Discussions of this system appear in Refs. 23, 27, and 54.

7.3 *X-Ray Diffraction and Other Applications*

The type of application toward which this section is oriented is the case of an X-ray image of limited intensity which is to be detected as conveniently as possible. A typical application in mind here is that of Laue diffraction work. Another, usually applicable to higher energy X-radiation, is industrial radiography.

As in the case of many other applications, film is useful but not always the optimum detector. Its variable exposure time gives it effectively a very wide dynamic range, but it is highly nonlinear (gamma $\neq 1$)[55] and relative intensities cannot be easily measured.[28] The desire to see a picture more rapidly, either by reducing exposure time or eliminating the developing process, or both, provides motivation to consider other imaging systems. Moreover, the increased sensitivity provided by alternate systems for low energy X-radiation may permit imaging in cases where the required film exposure time would lead to excessive fogging.

Image intensifier systems have been used in the past in such applications as Laue diffraction work, to allow continuous monitoring of the diffraction pattern as a crystal is oriented.[23,35,47] The inherent limita-

tion in these systems is their limited resolution of $d \approx 0.4$ mm, owing in part to lateral scattering of light.[22]

Scanned-image tubes can improve upon resolution, permitting orientation of very small crystals (requiring more highly collimated beams) or more accurate measurement of larger crystals than would be possible with an image intensifier system. Because of unity gamma, relative intensities at a given X-ray energy may be measured electronically. In addition, the integration time during which the image is being accumulated in the charge pattern on the target can be varied electronically, corresponding to varying the exposure time when using film.

There are several ways in which scanned-image camera tubes may be compared. The points of comparison are charge storage time, sensitivity, and convenience. Since, in a tube without electron multiplication, amplifier noise usually dominates, comparison of sensitivity also constitutes an evaluation of signal-to-noise ratio or picture quality.

The difference between the applications currently under discussion and medical applications is that rather than there being a limitation upon total number of photons incident upon the viewed object, there is instead a limitation upon the total photon flux rate available to illuminate it. Thus the number of incident photons per picture element is proportional to the integration time τ_i which is used to accumulate the picture. Since the signal increases linearly with τ_i but the noise increases no faster than the square root of τ_i, it is advantageous to use the longest integration time that is consistent with linear system response and operator convenience. If changes in the image are to be observed, for example changes in a Laue pattern as a crystal is oriented, it is probably desirable that the integration time not exceed $\approx$1 second, and frequently preferable to make it even less, say 0.1 second.

Since the integration time may be arbitrarily increased without changing frame time by frame delay, as described in Section II, the maximum integration time that can be used is determined simply by the duration of time for which charge can be stored on a picture element. In the case of a photoconducting camera tube this time constant can be very long. Charge storage times longer than 2 minutes have been reported for tubes with amorphous selenium targets,[40] and similarly long storage times should apply to photoconductors with such high dark resistivities as PbO[56] and CdS.

In a diode array target, the dark leakage current determines the charge storage time. For tube No. TN-84, it was found that the dark

current was a linear function of the quantity (V_T − 1.5 volts) over the range $1.5 \leqq V_T < 5$ volts. It will be assumed that an appropriate model for the effect of the dark current is therefore a resistance R connected across the diode capacitance C. Because of the nature of the photo-process, absorbed photons may be represented by a current generator. The electron beam is represented by a battery of voltage $V = V_T - 1.5$ and a switch whose momentary closure represents the scan of the electron beam across the diode in question. The current through the battery is the video current. This extremely simple equivalent circuit is shown in Fig. 6.

Consider the following experiment: The electron beam is blanked off at $t = 0$, just after reading a frame, and after a time τ a source of optical or X-ray photons is flashed briefly on. This source is confined to a limited area of the target so that both light and dark signals are available for comparison. Now after an additional time T during which there is no photon source and still no electron beam, the electron beam is again turned on and allowed to scan. As the electron beam sweeps the target, the integrated current flowing to both those regions without photon input and those with photon input is measured. The difference in these quantities will be called the signal amplitude.

In terms of the equivalent circuit, consider that the circuit represents a diode or picture element. Some fraction p of a frame time prior to $t = 0$, the switch was briefly closed and the capacitor acquired the battery potential. Then at time τ the current generator furnished a unit pulse of charge. Then after time T plus an additional $(1-p)$ frame times, the switch was briefly closed again and the charge passing from the battery to charge the capacitor was measured. This constitutes a measurement of the video signal plus accumulated dark current. The experiment is also repeated, but without the current generator pulse, to measure only the accumulated

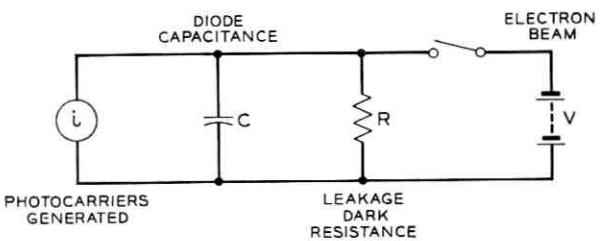

Fig. 6 — Equivalent circuit for one picture element in a diode array camera tube.

dark current. The difference of these two measurements is again the signal amplitude.

The reader may determine by a simple circuit analysis that T is varied the signal amplitude changes in proportion of $\exp(-T/RC)$. Thus by varying the frame delay time T it is possible the charge storage time $\tau_s = RC$ of the circuit.

Such an experiment was carried out with the tube just described, No. TN-84, and it was found that the signal amplitude did decay exponentially as a function of the frame delay time T. The only departure from exponential decay occurred at very long delays and was found to be caused by there being insufficient beam current available to completely charge down the target after such a long-time loss of charge. The results were that the charge storage time was 0.184 ± 0.027 seconds at 27.5°C, increasing to 1.197 ± 0.341 seconds in the range 7 to 11°C. Since this target did not have diodes with low leakage currents, showing instead the relatively large dark current of 70 nA/cm^2 at 32°C, other diode array targets should have even longer charge storage times. Charge storage times as long as $\approx$85 seconds seem to be possible with better targets (this assumes a cooled target with dark current 0.1 nA/cm^2 and a typical diode capacitance value of 2000 pF/cm^2). Storage times longer than about a minute are probably not needed in sequential imaging applications, since film is a convenient medium for such long exposure times.

The result is that for typical sequential imaging applications both the silicon diode array and potential X-ray photoconductive target materials (selenium, CdS, and PbO) have sufficiently long charge storage times to be used. The next point taken for comparison between different camera tubes will be sensitivity.

As before, camera tubes will be compared assuming blocking contacts, but only a relatively thin depletion region, so that carriers must diffuse to an electrode for collection. To compare sensitivity, it will be assumed that the photosensitive target material is chosen to have the thickness of one carrier diffusion length to insure high collection efficiency. In the case of silicon this implies a target thickness of 0.004 inch, which does lead to the very greatest sensitivity in the predicted curves of Fig. 4. For selenium this gives a target thickness of 10μ, which agrees with the optimum target thickness reported by Smith.[40] The same assumptions will be made about CdS and PbO for this comparison. Obviously the question of optimum target thickness depends upon not only the bulk and surface properties of the materials, but upon the energy of X-rays which it is desired to detect, and

the comparison here can only be qualitative. Nevertheless, it is instructive to consider how the sensitivities of various types of camera tubes would compare for use in the lower energy region such as that appropriate for crystal diffraction studies; these assumptions offer a simple and unbiased means for evaluation.

Another piece of information needed is the average energy, ΔE, required to free a carrier. Measured values are available for PbO, CdS, and silicon, but aparently not in the case of selenium. These energies typically seem to be roughly proportional to the band gap energy in the material, as shown in Table III and discussed somewhat in Ref. 57. Thus a value of ΔE for selenium is estimated that is consistent with the other values and tends to be optimistic in its predictions of sensitivity (that is, the value of ΔE is as small as would be consistent with other values in the table). The typical energies for these applications are taken to be 10 keV and 25 keV for this com-

TABLE III — COMPARISON OF CAMERA TUBES FOR LOW-ENERGY IMAGING

Substrate Material	PbO Tetragonal	Se Amorphous	CdS n-type	Si n-type
Absorption discontinuities between 5 and 30 keV*	13.03–15.86 L_{Pb}	12.65 K_{Se}	26.712 K_{Cd}	none
Target thickness t, μm(= diffusion length)†	1.2	10	6.4	110
Carrier production energy, ΔE, in eV	8‡	≈6.7§	≈8.3¶	3.5‖
Ratio of ΔE to band gap#	3.48	3.19	3.46	3.18
Absorption coef. α, $(\mu m)^{-1}$:†				
E = 10 keV	0.1117	0.0226	0.0496	0.00804
E = 25 keV	0.0465	0.0134	0.00431	0.000576
f = 1 − exp (−αt):				
E = 10 keV	0.125	0.202	0.272	0.586
E = 25 keV	0.054	0.126	0.027	0.060
Geometrical efficiency g	—	0.80**	—	0.88††
Relative response, S = fE/ΔE:				
E = 10 keV	156	302	328	1680
E = 25 keV	169	470	81	428

* *Handbook of Chemistry and Physics*, 48th ed., Chemical Rubber Company, p. E-125.

† See Table II for references.

‡ See Ref. 57.

§ Estimated to make the ratio of ΔE to band-gap the same as for silicon, which constitutes an optimistic estimate for the purpose of estimating the overall sensitivity.

¶ The average of the values 7.3 and 9.3 quoted by Lappe (Ref. 57).

‖ See Ref. 19.

Band gap energies are from R. H. Bube, *Photoconductivity of Solids*, New York: John Wiley & Sons, 1960, pp. 233–234.

** For target thickness 0.001″. See Ref. 39.

†† From Fig. 6 of this article, with t = 0.004″ and E = 10 and 25 keV.

parison, and the usable fraction of the incident photons $f = 1 - \exp(-\alpha t)$ can be calculated in terms of the absorption coefficient α and the thickness t of the target, as shown in Table III.

The relevant target parameter that determines the size of the video signal is the product ηf. Since η is the number of video electrons collected per usefully absorbed X-ray photon, and since each photon produces a number of carriers equal to $E/\Delta E$, it follows that

$$\eta = gE/\Delta E. \tag{5}$$

In this equation, g is the geometrical efficiency, the same quantity discussed in connection with Fig. 4, which was defined as the fraction of free carriers generated which lead to video current. Since the target thickness has been taken equal to the carrier diffusion length, the geometrical efficiency will be quite high, as may be determined from Fig. 4. Table III shows typical values for g for silicon and selenium. Because of the choice of target thicknesses, it is appropriate to assume that the geometrical efficiency will be close to unity for all the target materials here considered. Therefore, instead of comparing relative sensitivities on the basis of $\eta f = gfE/\Delta E$, a meaningful comparison of sensitivity can be made by simply comparing the quantity

$$S = fE/\Delta E. \tag{6}$$

Thus a comparison of sensitivity between various scanned camera tubes for low-energy imaging can be made in a semiquantitative way by comparing a single sensitivity number S at the X-ray energies of interest. This has been done in the last two lines of Table III for X-ray energies of 10 and 25 keV.

The PbO target performs poorly because of its extremely short carrier diffusion length, necessitating a very thin target. At 25 keV selenium is the most sensitive, followed closely by silicon; at 10 keV silicon is by far the most sensitive (selenium has less than 20 percent of its sensitivity). To emphasize the sensitivity of silicon, notice that X-ray imaging in the 10 keV range has been carried out with a silicon diode array with sensitivity approximately equal to that of Polaroid film (ASA 3000) using a standard cassette with internal fluorescent screen.

If it is possible to extend the depletion region to greater depths, then increased target thicknesses may be possible without loss of geometrical efficiency. In such a case the sensitivity of any of these possible camera tubes could be greatly increased. In the case of silicon

this could be done by reducing the substrate resistivity, providing that this did not also lead to increased dark current. With the other target materials this could be accomplished by fabricating effective blocking contacts which could remain blocking up to sufficiently high voltages to extend the depletion region, or by making good p-n junctions in material of low resistivity. The most progress along these lines has probably been made with PbO targets, although the published observations concerning X-ray detection with PbO camera tubes seem to be too sparse to permit detailed comparisons with the silicon camera tube.

A further point for comparison that is relevant is the uniformity of sensitivity over the energy range that it is desired to operate. For the materials discussed here, Table III shows the positions of any absorption discontinuities occurring in the range 5 to 30 keV. Since the absorption of the elements in question changes by a large factor (2 to 5) at the energies indicated, the presence of absorption discontinuities is reflected in a great difference in the sensitivity of the camera tube on either side of these energies. This can be an inconvenience, both because of the unfamiliar appearance it may give to familiar Laue diffraction patterns and because of the great variation in threshold sensitivities when X-ray flux intensities are to be measured. From this standpoint, both PbO and selenium seem undesirable for low-energy imaging. CdS is better, having only a discontinuity at 26.712 keV, but silicon is clearly the target material least contaminated with unwelcome discontinuities in absorption. In fact, silicon has no such discontinuities above 1.838 keV, which is too low in energy for open-air diffraction work anyway.

The final point for comparison was referred to as "convenience", which includes whatever practical considerations may be relevant to selection of a camera tube for particular applications. A disadvantage of silicon diode array tubes arises when very long integration times are required, since some form of target cooling must be supplied to presently produced targets to obtain integration times much longer than a second. Although tubes are now being designed incorporating internal solid-state cooling, it would still be desirable to eliminate this additional complication. Improvements in target processing will probably permit integration times as long as ten seconds, even at room temperature, when targets with lower dark current become available.

There are other respects in which the silicon diode array looks more desirable. It can withstand high temperatures without damage (at

least several hundred degrees Centigrade), whereas an amorphous selenium target tends to crystallize above 30°C.[58] Moreover, although the diode array requires some special techniques for diffusion, the resulting target is durable and can withstand the kind of high temperature bakeout that seems always to be required when producing vacuum tubes with high reliability and years of life.

Some other general advantages to scanned camera tubes are common to all the types considered here. The dc level on the television monitor can be adjusted to provide a threshold signal below which no image appears, which is useful in removing background noise from the image. The apparent magnification of the image may be varied electronically by changing the raster size. Finally, simple electronic techniques like triggering a time-delay oscilloscope at the beginning of a frame allow the video signal current to be accurately measured at any desired locations in the image.

The question of damage resulting from incident X-radiation is still open. Silicon diode array targets coated with a silicon resistive overlay show a slight increase in dark current where they have been exposed to a direct beam from an X-ray tube. No damage at all seems to occur below a certain X-ray intensity, although this qualitative judgment may not turn out to be genuine when properly measured. Finally, this damage tends to anneal out when the tube is left warmed up without incident X-rays for a few hours, although some damage can still be detected.

These descriptive features have mainly emphasized the silicon diode array camera tube since the authors have very little information on the practical aspects of the other types of X-ray camera tubes. Commercially available tubes* are of the selenium target variety; they have relatively short life and cannot withstand high temperatures. Some information is available in the literature concerning PbO tubes[21, 41] but apparently not on CdS.

VIII. CONCLUSIONS

The following are the distinguishing features of the silicon diode array camera tube as applied to X-ray imaging. This device has high sensitivity and a smooth spectral response in the range 5 to 30 keV. Electronic zooming can be used to vary picture magnification. Silicon is easy to work with and clean for vacuum tube use; good fabrication

* Westinghouse Type WX-5129 X-Ray Vidicon, Westinghouse Electric Corporation, Electronic Tube Division, Elmira, N. Y.

technology has been developed, especially locally. Silicon camera tubes can be baked out at high temperatures.

Among the less desirable features of the silicon diode array are its relatively high dark current, requiring not too high an operating temperature, and, for low-intensity detection, requiring cooling of the target. In addition, for very long charge storage times, cooling would be necessary. The silicon diode array seems to exhibit some damage at high X-ray flux rates. It requires competent photolithographic techniques to fabricate, and for certain applications (such as medical work) it seems to be less desirable than CdS.

Future lines of work will include both improvement of the device and pursuit of practical applications. Measurements will be made of the photoemission from the surfaces of silicon diode array targets that have gone through all the usual special surface processing used to lower the surface recombination velocity. Tubes will be constructed having larger sensitive areas, at least ¾ inch in diameter, by covering the silicon disk with diodes and using a beryllium or mylar window to hold the vacuum instead of the silicon itself. Thicker targets will be used to increase X-ray absorption, and attempts will be made to make fully depleted thick targets, making use of lithium drifted silicon substrates. The possibility of carrier injection from denser materials deposited on the silicon as an overlay to increase X-ray absorption will be pursued. Tubes with internal solid-state target cooling, now being assembled and developed, will be tested. In addition, tubes may be built using internal electron multiplication as well as target cooling in hopes of carrying out photon counting and pulse height discrimination of photon energy.

Practical applications to be pursued will include techniques for X-ray orientation of crystals by conventional Laue techniques and other approaches. Some preliminary results on crystal orientation, as well as some simple topographic studies of crystals using the diode array camera tube, are reported elsewhere.[4] X-ray imaging will prove useful in several health physics applications. With proper calibration of radiation dose rather than photon flux, and beam intensity profile determinations, this technique will be useful in establishing dose distributions in X-ray beams to which humans are exposed either accidentally or intentionally, as in X-ray radiotherapy. Such measurements are being made by M. M. Weiss. Use of the camera tube as a magnifying monitor in both X-ray and electron microscopy is being evaluated, the latter by Fabian Pease. Finally, the possibility of using denser target materials such as CdS will be considered for

further pursuing possible applications of the camera tube in medicine and radiography.

IX. ACKNOWLEDGMENTS

The authors are indebted to many persons who helped in essential ways in this work. The tube fabrication problems were solved and many of the measurements carried out by D. A. Brooks. K. H. Storks assisted by providing not only some essential X-ray equipment, but many enlightening suggestions and discussions. Technical conversations with E. I. Gordon, G. E. Smith, E. F. Labuda, M. H. Crowell, and B. Hakki contributed to the theoretical treatment presented here; computer programming by A. J. Chick made it possible to present the results in a very effective way. The authors are also grateful to J. V. Dalton, R. P. Hynes, and E. J. Zimany, Sr. for important contributions to the tube fabrication, to E. J. Zimany, Jr. and L. B. Hooker for assistance with technical problems, and to J. W. Harpster for discussing his work in advance of publication.

APPENDIX

Measurements of Silicon Diode Array Target Reflectivity

In Fig. 2 the measured collection efficiency of the camera tube is shown, as corrected using published values for the reflectivity of silicon.[16] The data points show a certain oscillation in magnitude as a function of wavelength. To understand this effect more fully, the reflectivity of the target was measured:

A Bausch & Lomb grating monochromator model No. 33-86-03 with 675 grooves per mm and 3-mm slits was used with a tungsten source and a Corning No. 2-64 infrared transmitting filter, the latter serving to remove second-order diffracted rays from the output beam. An aperture 2 mm in diameter as placed at the exit slit. Light from the monochromator passed through a 6.4-cm focal length lens and was reflected from a half-silvered mirror with an angle of incidence of about 45°, and the image of the 2-mm aperture was formed on the diode array target. The limiting aperture for this incident light was an 2-cm diameter aperture placed next to the lens, and the optical path length from this aperture to the target was 13 cm. Thus the incident light arrived at angles ranging up to $\tan^{-1}$ (1/13) = 4.41° with respect to the normal to the diode array target. Light reflected from the target again passed through the half-silvered mirror and

through another lens, which imaged the surface of the target on a solar cell. The diameter and placement of this lens were such that light was accepted leaving the target at any angle up to 14° with respect to the target normal. The light was chopped at 13 Hz and synchronously detected.

The reflectivity of the target was determined by comparing the 13-Hz light signal detected in the arrangement just described with the signal measured when the diode array target was replaced with a multilayer dielectric mirror. Two such mirrors, kindly loaned by L. B. Hooker, together furnished a reference reflectivity exceeding 99 percent in the wavelength range 0.85 to 1.5 microns. Care was taken not to saturate the solar cell during these measurements.

The reflectivity thus measured is plotted in Fig. 7. The data become increasingly less accurate at longer wavelengths because of the greatly reduced sensitivity of the solar cell at these wavelengths.

Fig. 7 reveals the same sort of oscillations previously observed in the collection efficiency data points of Fig. 2. Unfortunately it is not possible to correct the measured collection efficiency data using the reflectivity of Fig. 7 to verify that all the oscillations in Fig. 2 are spurious.

There are several reasons for this. First, the spectral width for the reflectivity measurement was about 100 Å, a significant fraction of the spacing between the reflectivity minima (≈700 Å), whereas the measurements of Fig. 2 were made with a considerably narrower spectral input. Second, since the oscillations presumably arise from

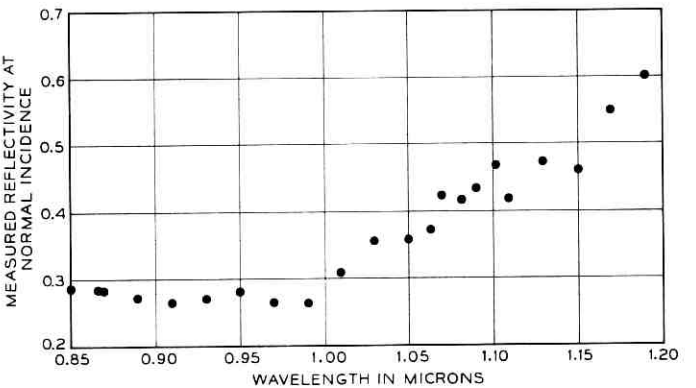

Fig. 7 — Measured reflectivity of the illuminated side of the target mounted in tube No. TN-84.

interference between multiple internal reflections in the target, their magnitudes should be strongly dependent upon the range of deviation of the incident light from the normal, which was also different in the two sets of measurements because of the different geometry used (a Perkin–Elmer monochromator was used for the collection efficiency measurements). Moreover, the collection efficiency measurements were made with the target newly mounted on the tube, but by the time the reflectivity measurements were made, the target surface had unavoidably become dirtier. These differences in surface cleanliness could easily have changed the amount of reflection either internally or externally at the silicon-air interface enough to change the magnitude of oscillations in the reflectivity from the values that would have been measured on a clean surface.

Moreover, it is not even possible to accurately compare the measured value of reflectivity (27.5 $\pm$ 1.0 percent) for wavelengths $0.80\mu\text{m} < \lambda < 1.0\mu\text{m}$ with published values of reflectivity, which amount to about 32 percent in this wavelength range.[16] It is quite possible that the scattering due to surface contamination was adequate to account for the discrepancy between the measured and the published values.

However, it is still possible to learn a lot of information from the reflectivity measurements. First they confirm the periodic behavior observed in the collection efficiency measurements. The minima in reflectivity observed at 0.91μm and 0.98μm could have arisen from interference between internal reflections in the target. Since the absorption coefficient is too great for much penetration to occur at these wavelengths, this would have to be caused by a thin surface layer of the target having slightly different optical properties from the rest of the target substrate. Its thickness may be estimated by setting

$$0.91(n + 1) = 0.98n, \tag{7}$$

from which

$$n = 13. \tag{8}$$

This gives an optical thickness for the layer of

$$\tfrac{1}{2}n(0.98) = 6.4\mu\text{m}. \tag{9}$$

Thus these oscillations in the reflectivity could be accounted for by a layer of thickness $\approx 2\mu$m since a typical refractive index for silicon in this wavelength range is ≈ 3.6.[59] It appears that this thickness of layer would also account for the oscillation in the collection efficiency dis-

played in Fig. 2. It is not known whether such a layer could be caused by impurities or dislocations near the surface.

Since the true magnitude of the oscillation cannot be accurately known, further remarks refer to Figs. 2 and 7 with the oscillating features replaced by slowly changing average values.

As previously pointed out, the discrepancy between the measured value of reflectivity of $\approx$27.5 percent and the published value of 32 percent in the wavelength range 0.85–1.0μm probably results from scattering. Since the factor needed to correct the measured values of collection efficiency to obtain Fig. 2 should really be $1/T$ (T = transmission of the silicon surface for entering photons) rather than $1/(1-R)$, the measured reflectivity values should really be augmented by the scattering if they were to be used to obtain Fig. 2. Thus it seems preferable to use the larger value 32 percent, as obtained from the literature, for this correction, at least for wavelengths shorter than 1.0μm.

For wavelengths beyond 1.0μm, the published values of reflectivity continue to decrease, approaching 30 percent,[10] but the values given in Fig. 7 rise significantly at longer wavelengths. Since the absorption coefficient of the silicon decreases sharply in this wavelength range, falling to only 4.24 cm^{-1} at 1.11μm,[11] the target rapidly becomes virtually transparent to light as the wavelength increases past 1.0μm. Thus the reflectivity of the target becomes the reflectivity of the front surface, augmented by the reflectivity of the back surface (measured to be $\approx$40 percent by a similar technique), finally complicated at sufficiently long wavelengths by multiple internal reflection if the front and back surfaces of the target are sufficiently parallel. Thus this rise in measured reflectivity at longer wavelengths is to be expected.

REFERENCES

1. Crowell, M. H., Buck, T. M., Labuda, E. F., Dalton, J. V., and Walsh, E. J., "A Camera Tube with a Silicon Diode Array Target," B.S.T.J. *46*, No. 2 (February 1967), pp. 491–495.
2. Gordon, E. I., unpublished work.
3. Chester, Arthur N., Loomis, Thomas C., and Weiss, M. M., "Direct Imaging of Low Energy X-Rays with a Diode Array Camera Tube," Conference on Electron Device Research, Boulder, Colorado, June 19–21, 1968, (unpublished).
4. Chester, Arthur N. and Koch, Fred B., "Instantaneous Display of X-Ray Diffraction Using a Diode Array Camera Tube," 17th Annual Denver X-Ray Conference: Applications of X-Ray Analysis, Estes Park, Colorado, August 21–23, 1968, (to be published in *Advances in X-ray, Analysis,* vol. XII, Plenum Press).
5. Benson, K. E., unpublished work.
6. Evans, Robley D., "Gamma Rays," *American Institute of Physics Handbook*, ed. Dwight E. Gray, New York: McGraw-Hill, 1963, 2nd ed., pp. 8–82 and 8–95.

7. Makhov, A. F., "The Penetration of Electrons Into Solids: I. The Intensity of an Electron Beam, Transverse Paths of Electrons," Soviet Physics—Solid State, *2*, No. 9 (March 1961), pp. 1934–1941.
8. Loomis, T. C. and Weiss, M. M., unpublished work.
9. Loomis, T. C., "Statistical Precision in X-Ray Spectrochemical Analysis," to be published by General Electric Company.
10. "Table of Mass-Absorption Coefficients," Instruments Division, Philips Electronic Instruments Company, Mt. Vernon, N. Y.
11. Runyan, W. R., *Silicon Semiconductor Technology,* New York: McGraw-Hill, 1965, p. 187.
12. Chester, Arthur N., unpublished work.
13. Crowell, M. H. and Labuda, E. F., unpublished work: "The Silicon Diode Array Camera Tube."
14. Buck, T. M., Casey, H. C., Jr., Dalton, J. V., and Yamin, M., "Influence of Bulk and Surface Properties on Image Sensing Silicon Diode Arrays," B.S.T.J., *47*, No. 9 (November 1968), pp. 1827–1854.
15. Gordon, E. I. and Crowell, M. H., "A Charged Storage Target for Electron Image Sensing," B.S.T.J., *10* (December 1968), pp. 1855–1874.
16. Runyan, W. R., *Silicon Semiconductor Technology,* New York: McGraw-Hill, 1965, p. 198.
17. Labuda, E. F., unpublished work. See also McKelvey, John P., *Solid State and Semiconductor Physics,* New York: Harper and Row, 1966, p. 402.
18. Kittel, Charles, *Introduction to Solid State Physics,* New York: John Wiley and Sons, 1937, 3rd ed., pp. 308 and 323.
19. Miller, G. L., Gibson, W. M., and Donovan, P. F., "Semiconductor Particle Detectors," Ann. Rev. Nuc. Sci., *12* (1962), pp. 189–220.
20. Harpster, J. W., unpublished work.
21. Jacobs, John and Berger, Harold, "Large-Area Photoconductive X-Ray Pickup-Tube Performance," Electrical Engineering, (February 1956), pp. 158–161.
22. Teves, M. C. and Tol, T., "Electronic Intensification of Fluoroscopic Images," Philips Technical Review, *14*, No. 2 (August 1952), pp. 33–43.
23. Bertin, Eugene P., "Visual Presentation of X-Ray Diffraction Patterns by Electronic Means," Analytical Chemistry, *25*, No. 5 (May 1953), pp. 708–721.
24. Tol, T. and Oosterkamp, W. J., "The Perception of Small Object-Detail," section II of "The Application of the X-Ray Image Intensifier," Philips Technical Review, *17*, No. 3 (September 1955), pp. 71–77.
25. Feddema, J., "Medical Aspects of the Image Intensifier," section V of "The Application of the X-Ray Image Intensifier," Philips Technical Review, *17*, No. 3 (September 1955), pp. 88–93.
26. Schott, Ottfried, "Bildverstärker und Fernsehen in der Röntgen-Diagnostik," Elektrotechnische Zeitschrift, *A85*, No. 19 (September 18, 1964), pp. 606–610.
27. Wegener, Arthur F., "An X-Ray Image Intensifier of the Closed Circuit Television Type," Nondestructive Testing, (January–February 1958), pp. 16–23.
28. *International Tables for X-Ray Crystallography,* Vol. III, ed. Caroline H. MacGillavry, Gerard D. Rieck, and Kathleen Lonsdale, Birmingham, England, The Kynoch Press, 1962, Sec. 3.1, pp. 133–156.
29. Herstel, W., "The Assessment of Image Quality in Medical Fluoroscopy," in *Photo-Electronic Image Devices,* proceedings of the third symposium held at Imperial College, London, September 20–24, 1965; *Advances in Electronics and Electron Physics,* Vol. 22A, ed. L. Marton, New York: Academic Press, 1966, pp. 363–368.
30. Harpster, J. W. and Jacoby, B. F., "Radiation Imaging with Electron Beam Scanning of *p-n* Junction Diode Arrays," Abstract No. D8 in Bull. Am. Phys. Soc., *13*, No. 7 (July 1968), p. 957.
31. Hoerlin, Herman and Mueller, F. W. H., "Gold Sensitization of X-Ray Films," J. Opt. Soc. Am., *40*, No. 4 (April 1950), pp. 246–251.
32. The Commission on Crystallographic Apparatus of the International Union of Crystallography, "A Comparison of Various Commercially Available X-Ray Films," Acta Cryst., *9*, part 6 (June 10, 1956), pp. 520–525.

33. Stahnke, Ingeborg and Heinrich, Hans, "Special Problems in Measuring the Modulation Transfer Function of X-Ray Image Intensifiers," in *Photo-Electronic Image Devices,* proceedings of the third symposium held at Imperial College, London, September 20–24, 1965; *Advances in Electronics and Electron Physics,* Vol. 22A, ed. L. Marton, New York: Academic Press, 1966, pp. 355–362.
34. Guyot, L. F. and Driard, B., "X-Rays Image Intensifiers Latest Developments: 3,000 gain 6" and 9" X-Rays C.F.T.H. Tubes," Le Vide, *85,* (January–February 1960), pp. 28–35.
35. Picker Special Products Catalog, publication No. 52–21 of Picker X-Ray Corporation, White Plains, New York.
36. Pierce, J. R., *Theory and Design of Electron Beams,* D. Van Nostrand Company, Princeton, New Jersey, 1954, 2nd ed., p. 121.
37. McNair, D., unpublished work.
38. Labuda, E. F., private communication.
39. Cope, A. D. and Rose, A., "X-Ray Noise Observation Using a Photoconductive Pickup Tube," J. Appl. Phys., *25,* No. 2 (February 1954), pp. 240–242.
40. Smith, C. W., "An X-Ray Sensitive Photoconductive Pick-up Tube," in *Photo-Electronic Image Devices,* proceedings of a symposium held at London, September 3–5, 1958, Vol. XII in *Advances in Electronics and Electron Physics,* ed. by L. Marton, Academic Press, New York, 1960, pp. 345–361.
41. Heijne, L., Schagen, P., and Bruining, H., "An Experimental Photoconductive Camera Tube for Television," Philips Technical Review, *16,* No. 1 (July 1954), pp. 23–25.
42. Bichsel, Hans., "Passage of Charged Particles Through Matter," section 8c of *American Institute of Physics Handbook,* ed. Dwight E. Gray, New York: McGraw-Hill, 1963, 2nd ed., pp. 8–43.
43. Verse, H. and Jensen, H., "Equipment for Spot Film Radiography Incorporating an Image Intensifier Fitted with a Periscope Optical System," section IV of "The Application of the X-Ray Image Intensifier," Philips Technical Review, *17,* No. 3 (September 1955), pp. 84–88.
44. Garthwaite, E., "X-Ray Image Intensifiers Using Image Orthicon Tubes," in *Photo-Electronic Image Devices,* proceedings of a symposium held at London, September 3–5, 1958; *Advances in Electronics and Electron Physics,* Vol. XII, ed. L. Marton, New York: Academic Press, 1960, pp. 379–387.
45. Rose, A., "Television Pickup Tubes and the Problem of Vision," in *Advances in Electronics,* ed. by L. Marton, New York: Academic Press, 1948, pp. 131–166.
46. DeHaan, E. F., "Signal-to-Noise Ratio of Image Devices," in *Photo-Electronic Image Devices,* proceedings of a symposium held at London, September 3–5, 1958; of *Advances in Electronics and Electron Physics,* Vol. XII, ed. L. Marton, New York: Academic Press, 1960, pp. 291–306.
47. Goetze, G. W. and Taylor, A., "Direct Viewing and Rapid Photographic Recording of X-Ray Diffraction Patterns," Rev. Sci. Inst., *33,* No. 3 (March 1962), pp. 353–359.
48. Harpster, J. W. and Jacoby, B. F., "Vidicon Optical and Nuclear Radiation Imaging Employing a Silicon Mosaic Array Target," Technical Conference on the Preparation and Properties of Electronic Materials, sponsored by Metallurgical Society of the AIME, Chicago, August 12–14, 1968, (proceedings to be published as March 1969 issue of Trans. Metallurgical Soc.)
49. Rose, Albert, *Concepts in Photoconductivity and Allied Problems,* New York: John Wiley and Sons, 1963, pp. 4–10 and 131–134.
50. Rose, A., "Maximum Performance of Photoconductors," Helv. Phys. Acta, *30,* No. 4 (August 15, 1967), pp. 242–244.
51. Redington, R. W., "Maximum Performance of High-Resistivity Photoconductors," J. Appl. Phys., *29,* No. 2 (February 1958), pp. 189–193.

52. van den Broek, J., "Physical Interpretation of a PbO-Photodetector," Solid State Commun., *4,* No. 6 (June 1966), pp. 295–297.
53. Spear, W. E. and Mort, J., "Electron and Hole Transport in CdS Crystals," Proc. Phys. Soc., *81,* part 1 (January 1963), pp. 130–140.
54. Greatorex, C. A., "Image Intensification Using a Flying-Spot X-Ray Tube," in *Photo-Electronic Image Devices,* proceedings of a symposium held at London, September 3–5, 1958; *Advances in Electronics and Electron Physics,* Vol. XII, ed. L. Marton, New York: Academic Press, 1960, pp. 327–344.
55. Dozier, C. M., Gilfrich, J. V., and Birks, L. S., "Quantitative Calibration of X-Ray Film Response in the 5-keV to 1.3-MeV Region," Appl. Opt., *6,* No. 12 (December 1967), pp. 2136–2139.
56. Schottmiller, John C., "Photoconductivity in Tetragonal and Orthorhombic Lead Monoxide Layers," J. Appl. Phys., *37,* No. 9 (August 1966), pp. 3505–3510.
57. Lappe, F., "The Energy of Electron-Hole Pair Formation by X-Rays in PbO," J. Phys. Chem. Solids, *20,* Nos. 3 and 4 (August 1961), pp. 173–176.
58. Weimer, Paul K. and Cope, A. Danforth, "Photoconductivity in Amorphous Selenium," RCA Review, *12,* No. 3 (September 1951), pp. 314–334.
59. Runyan, W. R., *Silicon Semiconductor Technology,* New York: McGraw-Hill, 1965, p. 200.

Approximate Large-Signal Analysis of IMPATT Oscillators

By J. L. BLUE

(Manuscript received August 11, 1968)

Insight into the large-signal operating characteristics of IMPATT oscillators has been obtained from detailed numerical calculations of D. L. Scharfetter and H. K. Gummel. However, their calculations are relatively expensive in computer time. Small-signal analyses of IMPATT diodes are much less expensive, but give little reliable information about oscillator performance.

This paper presents a model for large-signal analysis of IMPATT diodes which requires less than 1 percent of the computer time used by Scharfetter and Gummel's method, but still provides a realistic description of IMPATT oscillators in modes of operation which maintain carrier velocity saturation. We show graphical results, based on numerical computations, which provide information about phase relationships in IMPATT oscillators and improve understanding of the two-frequency mode of operation.

I. INTRODUCTION

Considerable insight into the large-signal operating characteristics of IMPATT oscillators has recently been obtained by D. L. Scharfetter and H. K. Gummel through numerical calculations involving a complete modeling of the physical processes taking place in the diode.[1] They solve the one-dimensional partial differential equations for the generation, diffusion, and drift of holes and electrons, as well as Poisson's equation and the differential equations for the circuit in which the diode is embedded. Their analysis, which has led to improved understanding of IMPATT diodes and insight into new modes of oscillation, includes most of the important physical effects. Since their model is so detailed and accurate, their analysis is a large-scale computer project. Even after the computer programs are debugged, analysis of IMPATT diodes is relatively expensive.

Another possible method is small-signal analysis, which is tractable numerically and more economical.[2-4] However, small-signal analysis gives only a limited amount of information about large-signal oscillation.

An intermediate model has been presented by W. J. Evans.[5] However, his simplified large-signal model requires short transit-time in the drift region. He obtained a single first-order differential equation for the diode current, and was able to solve analytically for the (large-signal) diode current and voltage as a function of time. Unfortunately, the restriction to short transit time and his use of other approximations severely limit the applicability of his results.

This paper presents a model for large-signal analysis of IMPATT diodes which incorporates most of the important physical processes in the diodes, but which is more tractable numerically than that of Scharfetter and Gummel. Because the new model requires far fewer computer hours than Scharfetter and Gummel's model, parameter studies are feasible; because the new model contains more physics than Evans' model or the small-signal models, the results are more reliable and more effects can be studied.

II. LARGE-SIGNAL IMPATT MODEL

We consider a one-dimensional diode, neglect diffusion, and assume that the electric field is large enough so that holes and electrons move at scatter-limited velocities. The latter assumption is essential for simplifying the calculations, but means that our model is not applicable to some important oscillator modes, such as analyzed by Scharfetter, Bartelink, and Johnston.[6]

The other important simplification is that in Poisson's equation we neglect the space charge of the ac component of the particle current in the avalanche region. The detailed calculations of Scharfetter and Gummel show that this is a good approximation for the classical Read mode of operation and other modes where the width of the avalanche region remains fairly constant during the oscillation cycle.[7] We include the space charge of the dc component of the particle current in the avalanche region, and both ac and dc components of the particle current in the drift region. This says that the shape of the electric field profile in the avalanche region does not change in time, although the magnitude of the field does; that is,

$$E_{aval}(x, t) = f(x) + E(t). \tag{1}$$

This is equivalent to the commonly-made assumption that the particle current is constant in the avalanche region.[2, 5, 7] Given a bias current and the doping in the diode, we can calculate $f(x)$ by solving a second-order differential equation by standard methods.[3, 4]

We can treat diodes in which holes and electrons have unequal scatter-limited velocities and unequal ionization coefficients, although the model we have chosen for computation assumes the same values for electrons as for holes. The ionization coefficients may be any given function of the electric field, such as $A \exp(-b/E)$.

Besides the simplifications resulting from our diode model, we obtain important simplifications by solving directly for a periodic solution, rather than solving for a transient solution which eventually becomes periodic. We save computation time both because we eliminate solving for the unneeded transient solution, and because we are able to use more advantageous numerical methods.

Notice that the essential approximations are constant carrier velocities and equation (1); many combinations of additional approximations may be made, so that we are describing a whole hierarchy of IMPATT models. The aproximation of equation (1) can be overcome by a recursive method of solution, the first step of which is the subject of this paper. However, for most purposes equation (1) is sufficiently accurate.

III. IDEALIZED DIODE

In the rest of this paper, we consider a fairly simple model of an IMPATT diode; we are able to emphasize the essential features of the method without becoming lost in algebra. (We plan to treat the most general case in a subsequent article.)

We consider a diode with a uniform electric field $[f(x) = 1]$ in the avalanche region (of length d_a), and one drift region (of length d_d). We assume equal hole and electron velocities and ionization coefficients, so that the continuity equations for holes and electrons in the avalanche region are

$$\partial p(x, t)/\partial t = v\alpha[E(t)][p(x, t) + n(x, t)] - v\, \partial p(x, t)/\partial x$$

$$\partial n(x, t)/\partial t = v\alpha[E(t)][p(x, t) + n(x, t)] + v\, \partial n(x, t)/\partial x.$$

The importance of the approximations discussed in Section II is that they enable us to avoid dealing with the hole and electron densities as functions of both space and time. We proceed much as did

Read[7] and Evans,[5] adding the two continuity equations to obtain an equation involving the particle current density

$$\partial I_p(x, t)/\partial t = 2v\alpha I_p - qv^2\,\partial(p - n)/\partial x. \tag{2}$$

The total current, particle plus displacement, is

$$I_T(t) = I_p(x, t) + \epsilon\,\partial E(x, t)/\partial t. \tag{3}$$

I_T is independent of x; since E in the avalanche region is independent of x, $I_p(x, t)$ is also independent of x. Using this fact, we integrate equation (2) over the avalanche region. Neglecting reverse saturation current, we obtain

$$\partial I_p/\partial t = \frac{2vI_p}{d_a}\{d_a\alpha[E(t)] - 1\}.$$

If we use $\alpha(E) = A\exp(-b/E)$, and define E_c as the "critical" field (that field necessary to maintain the dc current under static conditions) then $\alpha(E_c) = 1/d_a$. We obtain

$$\partial I_p/\partial t = \frac{2vI_p}{d_a}[(Ad_a)^{1-E_c/E(t)} - 1]. \tag{4}$$

(Evans linearized the electric field, and used

$$\partial I_p/\partial t = \frac{2v}{d_a} I_p m\left[\frac{E(t)}{E_c} - 1\right].$$

We retain the more nonlinear version.)

We treat the case in which there is an applied voltage* $V(t)$ in excess of that required to maintain the dc reverse bias current density I_o. The avalanche electric field is reduced by the space charge of the particle current in the drift region; as in Read, we have

$$E(t) = E_c + V(t)/(da + d_d) - \frac{1}{\epsilon}\int_{t-T_d}^{t} I_p(t')\left(1 - \frac{t' - t}{T_d}\right)dt' \tag{5}$$

where $T_d = d_d/v$ is the time for particles to pass through the drift region after leaving the avalanche region. In equation (5) and the remainder of this paper we specialize to the case $d_a \ll d_d$, as Read and Evans did.

Equations (4) and (5), together with suitable initial conditions, may be solved for $E(t)$ and $I_p(t)$. The total current, which is equal

* We could equally well treat the case where there is an applied terminal current $I_T(t)$. It is only slightly more difficult to embed the diode in a circuit; then we use Kirchoff's laws to write $V(t)$ in terms of $I_T(t)$ and the circuit parameters, generally as an integral over I_T.

to the terminal current, may be obtained from equation (3):

$$I_T(t) = \frac{\epsilon}{d_a + d_d} dV(t)/dt + \frac{1}{T_d} \int_{t-T_d}^{t} I_p(t')\, dt'. \tag{6}$$

The first term is the displacement current and the second is the particle-induced terminal current, I_{T_p}.

Instead of solving the initial-value equations for the transient solution, and extending the solution far enough in time for the limiting periodic solution to be obtained, it is preferable to solve directly for only the periodic solution. We assume $V(t)$ to be periodic (not necessarily sinusoidal) with period τ, and find solutions $E(t)$ and $I_p(t)$ which also have period τ. Now we need solve only for t in the interval $(0, \tau)$. It is more convenient to rewrite equation (4) as an integral equation; integrating equation (4) from 0 to t, we obtain ($T_a = d_a/v$)

$$I_p(t) = I_p(0) \exp\left\{\frac{2}{T_a} \int_0^t [(Ad_a)^{1-E_c/E(t')} - 1]\, dt'\right\}. \tag{7}$$

We substitute equation (5) for $E(t')$, and have a single integral equation for $I_p(t)$, which we shall not write explicitly; since $I_p(t + \tau) = I_p(t)$, we solve only for $0 \leqq t \leqq \tau$. Because of its complexity, it will be solved numerically; for our method to be useful, we must be able to find numerical solutions quickly and reliably. We solve this nonlinear integral equation by a standard iterative method, which converges quickly and stably.

We divide the interval $(0, \tau)$ into M intervals, let $t_n = n\tau/M$, and solve equation (7) approximately for the M values $I_p(t_n)$, $n = 1, 2, \ldots, M$. The integrals are evaluated by, for example, the trapezoidal rule, with integrands evaluated only at times t_n. We obtain a system of M nonlinear equations for the values $I_p(t_n)$, which are easily solved by, for example, the matrix analog of the Newton-Raphson method. More accurate integration rules than the trapezoidal rule may be used. They are more complicated to program, but save execution time because, for a given accuracy, fewer points need be used.

After the $I_p(t_n)$ are found, then the $I_T(t_n)$ may be found from equation (6). Then we Fourier-analyze I_T and V; the ratio of their fundamental components is the large-signal admittance at the frequency $\nu = 1/\tau$. The ac power delivered by the diode also is easily calculated.

The small-signal admittance can be calculated analytically. It is

$$Y(\omega) = \frac{\epsilon}{(d_a + d_d)T_d} \left[\frac{1 - \omega^2/\omega_a^2}{\xi(\omega) + i\omega/\omega_a^2 T_d}\right]$$

where

$$\xi(\omega) = \frac{\exp(-i\omega T_d) - 1 + i\omega T_d}{(-i\omega T_d)^2}$$

and

$$\omega_a^2 = \frac{2\alpha'(E_c)vI_0}{\epsilon}.$$

This admittance agrees with that of Gilden and Hines, when their "passive resistance of the inactive zone R_s" is neglected.[2]

IV. RESULTS

We analyze a germanium IMPATT oscillator similar to the one reported by Swan.[8] The results, which are presented graphically, are meant more as an illustration of typical results obtainable than as a comprehensive analysis of Swan's oscillator. In particular, the uniform avalanche region approximation is inadequate. However, even these preliminary results can clarify some aspects of IMPATT oscillator operation.

The diode we analyzed has an avalanche width $d_a = 1.5 \times 10^{-4}$ cm, a drift width $d_d = 3.5 \times 10^{-4}$ cm, and a carrier velocity $v = 5 \times 10^6$ cm per second. The ionization coefficient is $\alpha(E) = 5.9 \times 10^{+6}$ cm^{-1} exp[-1.2×10^6 (V/cm)/E].

Figure 1 shows typical solutions for the ac components of $V(t)$, $I_p(t)$, and $I_{T_p}(t)$. Two cycles are shown; we plot I_{T_p} instead of I_T, because the displacement current component of I_T delivers no power. The frequency is 5 GHz, and the ac voltage amplitude is 10 volts. The avalanche region particle current is extremely nonsinusoidal, and becomes more so with increasing ac voltage amplitude. The fundamental component of $I_p(t)$ lags the ac voltage by about 49.5 degrees; this phase angle also increases with increasing ac voltage, approaching 90 degrees. The phase is closer to 90 degrees for higher frequencies; this may be attributed to the lessened effect of drift region space charge on the avalanche region field. (Read showed that the phase is 90 degrees when the space charge can be neglected, so that the electric field in the avalanche region is in phase with the terminal voltage.) The phase will be discussed further in connection with Fig. 3.

Figure 2 is a complex-plane admittance plot; the dc component of I_T is fixed at 500 A/cm^2, and the ac component of $V(t)$ is a pure sine wave, as it would be if the diode were embedded in a high-Q parallel

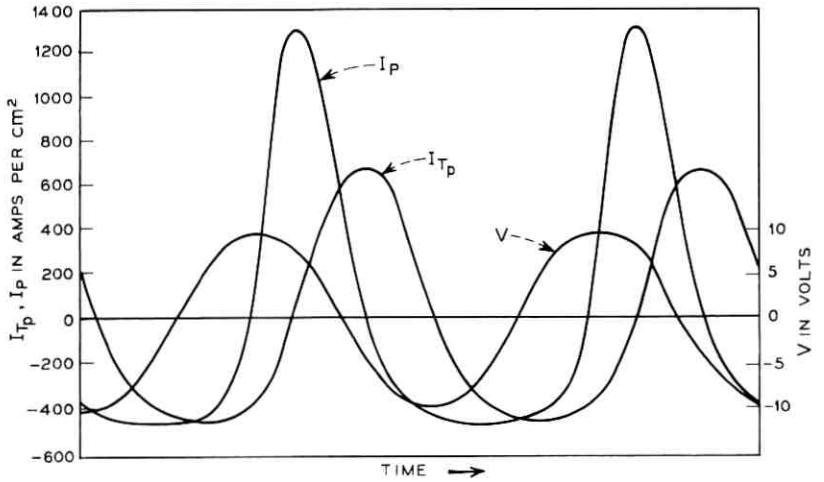

Fig. 1 — AC components of V, I_p, I_{T_p} at frequency 5 GHz, current density 500 A/cm², ac voltage amplitude 10 V. Two cycles shown.

resistance-impedance-capacitance (RLC) circuit with only one resonant frequency. The solid curves are curves of constant ac voltage amplitude; the dashed lines are curves of constant frequency. For frequencies about 6 GHz and above, the negative conductance decreases with increasing ac voltage amplitude. For lower frequencies, the negative conductance first increases, then decreases with increasing ac voltage amplitude. For some low frequencies, for example 4 GHz, the diode has positive small-signal conductance, but negative large-signal conductance for large enough ac voltage. This type of behavior agrees with that found at low frequencies by the detailed calculations of Scharfetter and Gummel.[9]

Insight into this type of behavior may be obtained from Fig. 3, which shows the amplitude and phase (with respect to the ac voltage) of the fundamental component of $I_p(t)$. Curves of constant ac voltage amplitude are solid and curves of constant frequency are dashed. To transform any point on this plot to a complex admittance plot, one first multiplies the complex number representing the point by

$$[\exp(-i\omega T_d) - 1]/(-i\omega T_d)$$

to give the fundamental component of I_{T_p}. (For small ωT_d, this is approximately the same as rotating the phase plot point of I_p clockwise

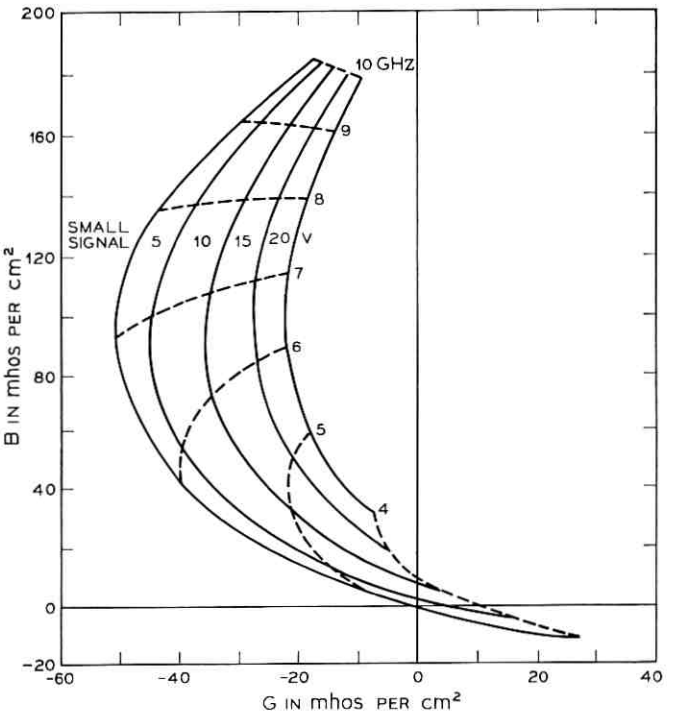

Fig. 2 — Complex-plane plot of diode admittance as a function of frequency and ac voltage amplitude. AC component of $V(t) = A \cos \omega t$. Current density 500 A/cm².

by $\frac{1}{2}\omega T_d$.) If the resulting point is in the second or third quadrant, then the diode has negative conductance at that frequency and ac voltage amplitude. Then the amplitude is divided by the magnitude of the fundamental component of the ac voltage amplitude; finally the point is moved directly upwards by $\epsilon\omega/(d_a + d_d)$ to add in the displacement current component.

At low frequencies, increased ac voltage amplitude improves the avalanche current phase considerably; at 4 GHz, where the small-signal conductance is positive, the improvement is sufficient so that the approximately $\frac{1}{2}\omega T_d$ rotation puts the phase plot point into the third quadrant, and negative conductance results for amplitudes above about 12 volts.

Figure 4 shows output power in the fundamental, in watts per square centimeter. Maximum output power is obtained near the fre-

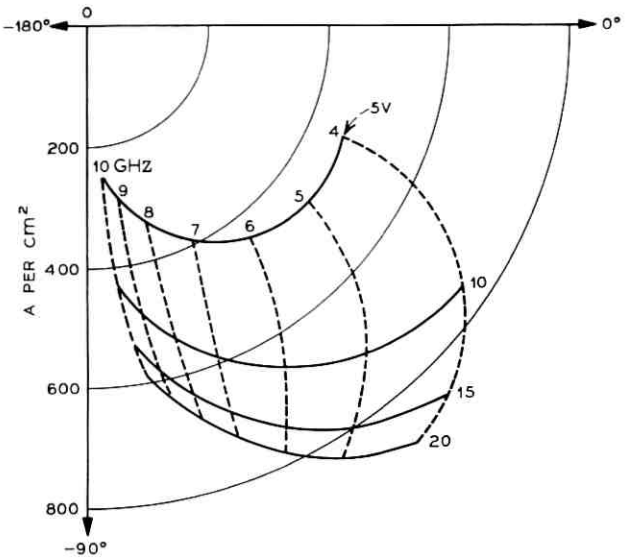

Fig. 3 — Magnitude and phase plot of fundamental component of avalanche particle current, $I_p(t)$, as a function of frequency and ac voltage amplitude. Current density 500 A/cm².

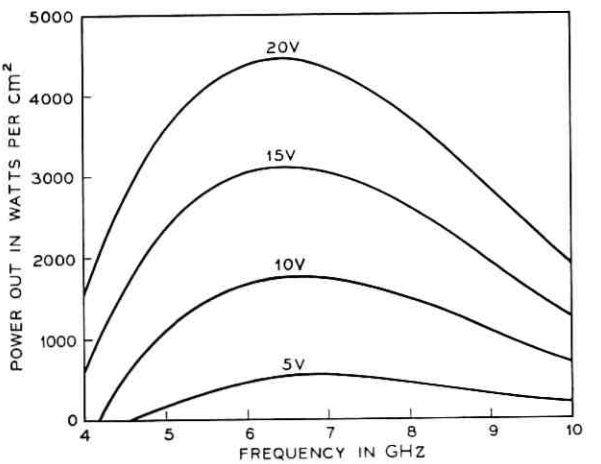

Fig. 4 — Output power vs frequency for various ac voltage amplitudes. Current density 500 A/cm².

quency with largest small-signal negative conductance. Efficiency depends upon the dc voltage across the diode, and therefore on the dc electric field in the drift region. The idealized model merely assumes this field large enough to maintain scatter-limited velocity. A better lower bound is obtained by calculating, at each point in the diode, the reduction in field resulting from the space charge of the current pulse drifting away from the avalanche region. Since I_T is independent of x,

$$\epsilon\, dE(x, t)/dt = I_p(t) + \epsilon\, dE_{aval}(x, t)/dt - I_p(t - x/v).$$

Integrate from 0 to t and subtract the dc component to obtain

$$\Delta E(x, t) = \Delta E_{aval}(t) + \int_0^t [I_p(t') - I_p(t' - x/v)]\, dt'.$$

Requiring the dc field at x to be as least as large as

$$\max_t [-\Delta E(x, t)]$$

gives the minimum field in the drift region allowable, and thus gives the minimum drift voltage and maximum efficiency. The maximum ΔE is also of interest, since in our model it is assumed that no avalanching takes place in the drift region. If E_a is the minimum electric field for which appreciable avalanche ionization can take place, then we must require that

$$\max [\Delta E(x, t)] + \max [-\Delta E(x, t)] < E_a$$

for all x. This limits the allowable ac voltage amplitude. Numerical results indicate that, for a given current density, the allowable ac voltage amplitude depends only weakly on the frequency of oscillation and the shape of the voltage waveform $V(t)$. For our sample diode, if $E_a \approx 10^5$ volt/cm, 20 volts ac amplitude is, approximately, the limiting voltage for the simple diode model used. A more general model, with a nonuniform avalanche region, could partially include avalanche-broadening, and thus be used to analyze diode modes of operation with larger ac voltage amplitudes.

Swan, Lee, and Standley recently reported marked improvement in the performance of an IMPATT oscillator embedded in a microwave circuit resonant at two frequencies, the fundamental and its second harmonic.[8, 10] As an aid in understanding their results, in the rest of this section we present calculations in which $V(t)$ has the form $V_o \cos \omega t + \frac{1}{2} V_o \sin 2\omega t$. (This particular waveform is not the

optimum form, but is illustrative.) "Best" values of the magnitude and phase of the second harmonic depend on the frequency and magnitude of the fundamental, the bias current, the particular diode used, and the standards of performance to be applied to the diode.

Figures 5 to 8 correspond to Figs. 1 to 4; V_o is now chosen so that half the peak-to-peak value of $V(t)$ is 5, 10, 15, or 20 volts. In comparing the oscillations resulting from a two-frequency $V(t)$ with a one-frequency $V(t)$, we have chosen to compare voltage waveforms with equal ac peak-to-peak amplitudes, not with equal amplitudes in the fundamental, because of the ac amplitude limitation discussed earlier.

Figure 5 shows solutions for the ac components of $V(t)$, $I_p(t)$, and $I_{T_p}(t)$; the frequency of the fundamental is 5 GHz, and the maximum ac voltage is 10 volts. The fundamental component of $I_p(t)$ lags the fundamental component of the ac voltage by about 60 degrees instead of 49.5 degrees.

Figure 6 is a complex-plane admittance plot; for clarity, the lines of constant ac voltage are omitted, and dots are placed at 0, 5, 10, 15, and 20 volts. For nonsinusoidal ac voltages, the admittance at the fundamental can move to the left of the small-signal admittance line, resulting in a better negative conductance-to-susceptance ratio. This is especially apparent at 4 GHz; comparison of the 4 GHz, 20

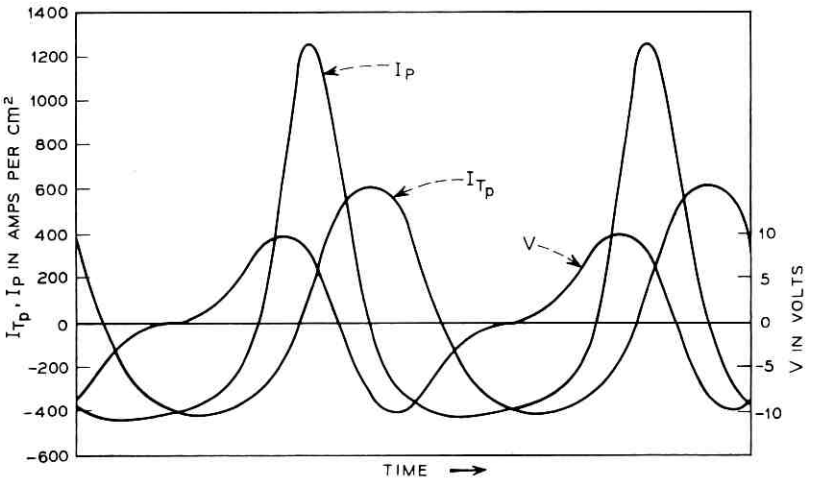

Fig. 5—AC components of V, I_p, I_{T_p} at frequency 5 GHz, current density 500 A/cm², ac voltage amplitude 10 V. Two cycles shown.

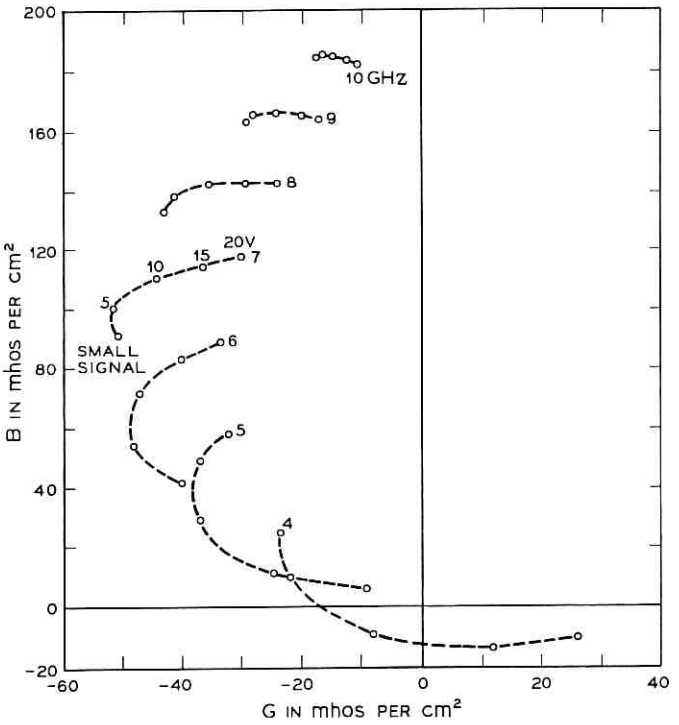

Fig. 6 — Complex-plane plot of diode admittance at fundamental frequency as a function of frequency and maximum ac voltage. AC component of $V(t) = V_o \cos \omega t + \frac{1}{2} V_o \sin 2\omega t$. Current density 500 A/cm².

V points in Figs. 2 and 6 indicates that the addition of a second harmonic component has improved the diode negative conductance by a factor of three, and the negative conductance-to-susceptance ratio by a factor of four.

Figure 7, corresponding to Fig. 3, shows in more detail the phase improvement obtained with addition of the harmonic component to the ac voltage.

Figure 8 shows output power in the fundamental. At higher frequencies, maximum output power is less than that shown in Fig. 4. At 5 GHz, maximum output power is about the same as in Fig. 4, but occurs at an improved negative conductance-to-susceptance ratio. This ratio is important when the diode's parasitic resistance R_p, which we have neglected, is included, since the power is proportional to

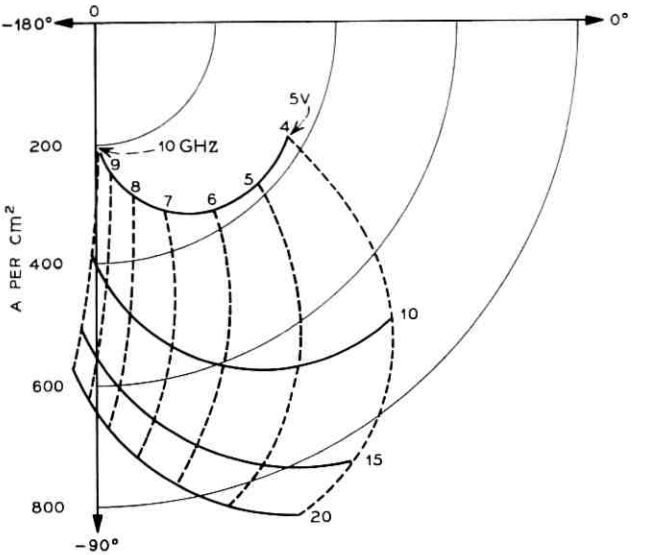

Fig. 7 — Magnitude and phase plot of fundamental component of avalanche particle current, $I_p(t)$, as a function of frequency and ac voltage amplitude. Current density 500 A/cm².

$- G/(G^2 + B^2) - R_p$. At 4 GHz, maximum output power is substantially better than that shown in Fig. 4. The nonsinusoidal form of $V(t)$ improves the phase of $I_T(t)$ sufficiently so that, even though $V(t)$ contains less of the fundamental, the output power in the fundamental remains about the same.

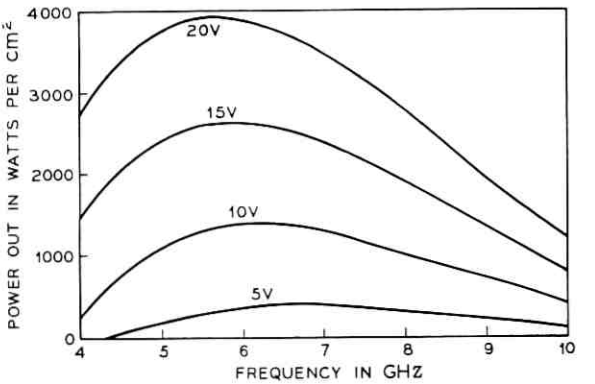

Fig. 8 — Output power in fundamental vs frequency for various maximum ac voltages. Current density 500 A/cm².

V. CONCLUSIONS

We have presented a numerically tractable method for analyzing large-signal IMPATT oscillators. It requires less than 1/100 of the computer time used by Scharfetter and Gummel's method, but still provides a realistic description of IMPATT oscillators in modes of operation which maintain carrier velocity saturation. (One solution takes about one second of computation time on the GE 645 computer, if we use 15 time steps per period.) Numerical calculations based on a simplified version of the model have provided information about the phase relationships in an IMPATT oscillator and improved understanding of the two-frequency mode of operation.

REFERENCES

1. Scharfetter, D. L. and Gummel, H. K., "Large-Signal Analysis of a Silicon Read Diode Oscillator," to be published in IEEE Trans. Elec. Devices, *ED-16*, No. 1 (January 1969).
2. Gilden, M. and Hines, M. B., "Electronic Tuning Effects in the Read Microwave Avalanche Diode," IEEE Trans. Electron Devices, *ED-13*, No. 1 (January 1966), pp. 169–175.
3. Gummel, H. K. and Scharfetter, D. L., "Avalanche Region of IMPATT Diodes," B.S.T.J., *45*, No. 10 (December 1966), pp. 1797–1827.
4. Gummel, H. K. and Blue, J. L., "A Small-Signal Theory of Avalanche Noise in IMPATT Diodes," IEEE Trans. Electron Devices, *ED-14*, No. 9 (September 1967), pp. 569–580.
5. Evans, W. J., "Nonlinear and Frequency Conversion Characteristics of IMPATT Diodes," Technical Report No. 104, Electron Physics Laboratory, Department of Electrical Engineering, The University of Michigan, February 1968. Also see: Evans, W. J., and Haddad, G. I., "A Large-Signal Analysis of IMPATT Diodes," IEEE Trans. Elec. Devices, *ED-15*, No. 10 (October 1968), pp. 708–716.
6. Scharfetter, D. L., Bartelink, D. J., and Johnston, R. L., "High Efficiency Subtransit Time Oscillations in Germanium Avalanche Diodes," Proc. IEEE, *56*, No. 9 (September 1968), pp. 1611–1612.
7. Read, W. T., Jr., "A Proposed High-Frequency, Negative Resistance Diode," B.S.T.J., *37*, No. 3 (March 1958), pp. 401–446.
8. Swan, C. B., "IMPATT Performance Improvement with Second Harmonic Tuning," Proc. IEEE, *56*, No. 9 (September 1968), pp. 1616–1617.
9. Scharfetter, D. L., private communication.
10. Lee, T. P. and Standley, R. D., "Frequency Modulation of a Millimeter-wave IMPATT Diode Oscillator and Related Harmonic Generation Effects," B.S.T.J., *48*, No. 1 (January 1969), pp. 143–161.

Digital PM Spectra by Transform Techniques

By LEIF LUNDQUIST

(Manuscript received September 10, 1968)

We derive an expression for the power spectrum of a class of nonstationary processes with periodicity in the two-dimensional autocorrelation function such that $R(t_1, t_2) = R(t_1 + T, t_2 + T)$. *Such a class includes many of the common digital signals. The method of derivation is based on the double Fourier transform which relates the spectrum of any signal to its autocorrelation function. This points to a very simple method of finding digital spectra.*

The results are applied to derive the general expression for the power spectrum of a wave phase modulated with a pulse stream $\sum_{-\infty}^{\infty} a_n g(t - nT)$. *The only restrictions on the pulse stream are that the* a_n*'s are independent and have identical probability distributions, and* $g(t)$ *is integrable and of finite length.*

I. INTRODUCTION

The power spectrum of a signal $x(t)$ can be defined in many ways. Every definition, however, has to yield some measure of the expected power at the output of a narrow bandpass filter, as a function of the center frequency of the filter.

If $x(t)$ is deterministic then the square of the magnitude of its Fourier transform represents energy density as a function of frequency. If the signal has finite length the energy is finite and we can define the power density to be the energy density divided by the length of the signal. If the signal has infinite length the energy may be infinite, but for realizable signals we can still define the power spectrum by operating on a finite time interval and finding the limit as the interval approaches infinity. This limit may include a set of δ-functions.

If $x(t)$ is a random signal the direct way of defining the power spectrum

is to find the Fourier transform of a sample function $x_o(t)$ on a finite time interval T_o, take the magnitude square, divide by T_o, average over all possible $x_o(t)$, and finally take the limit as $T_o \to \infty$.[1]

If $x(t)$ is stationary, the power spectrum is proportional to the Fourier transform of the autocorrelation function. This is a very useful property which often simplifies the task of finding the power spectrum.

The use of transform techniques can be extended to nonstationary processes by means of a double Fourier transform.[2] There is a very simple relationship between the double Fourier transform of the autocorrelation function $R(t_1, t_2)$ of $x(t)$ and the expected energy (or power) as a function of frequency. Through the proper definitions this technique includes both stationary and deterministic processes as special cases.

One would not expect that the term power spectrum would have much meaning in the general case of nonstationary processes. For one thing it would require infinite observation time to measure the spectrum. For some special classes of nonstationary processes we can talk about power spectra. For instance if the autocorrelation function is a function of the time difference and only slowly varying with time we can talk about locally stationary processes.

Another class of signals where power spectrum has a meaning is where periodicity in $R(t_1, t_2)$ exists. We will study signals for which

$$R(t_1, t_2) = R(t_1 + T, t_2 + T). \tag{1}$$

We will show that for this class of signals the transform technique can be used to derive a simple expression, equation (26), for the power spectrum. It is believed that this method of arriving at the power spectrum is simpler than the direct way used by Anderson and Salz in their treatment of digital FM spectra.[3]

Equation (26) is given in such a form that it can easily be used for many of the common digital signals. It should be especially useful when the digital pulses are overlapping. We apply it to digital PM which was not included in Ref. 3.

II. GENERAL CONSIDERATIONS

A signal $x(t)$ has the autocorrelation†

$$R(t_1, t_2) = E[x(t_1) \cdot x^*(t_2)]. \tag{2}$$

† The symbol* denotes complex conjugation.

We define†

$$\Gamma(\omega_1 , \omega_2) = \int_{-\infty}^{\infty} \int_{-\infty}^{\infty} R(t_1 , t_2) \exp (-j\omega_1 t_1 + j\omega_2 t_2) \, dt_1 \, dt_2 . \quad (3)$$

Papoulis has derived a number of properties for the transform pair (see Chapter 12 of Ref. 2).

Define

$$\rho(\tau) = \int_{-\infty}^{\infty} R(t + \tau, t) \, dt \quad (4)$$

and

$$W(\omega) = \frac{1}{2\pi} \int_{-\infty}^{\infty} \rho(\tau) e^{-j\omega\tau} \, d\tau. \quad (5)$$

$W(\omega)$ is the average energy spectrum and it can be shown that

$$W(\omega) = \frac{1}{2\pi} \Gamma(\omega, \omega). \quad (6)$$

If $x(t)$ has infinite length we can define the average power spectrum as

$$S(\omega) = \lim_{T_o \to \infty} \frac{W_o(\omega)}{T_o} \quad (7)$$

where $W_o(\omega)$ is the energy spectrum of $x(t)$ taken over an interval of length T_o.

Combining equations (2), (3), (6), and (7) we have

$$S(\omega) = \lim_{T_o \to \infty} \frac{\int_{-T_o/2}^{T_o/2} \int_{-T_o/2}^{T_o/2} E[x(t_1) \cdot x^*(t_2)] \exp [-j\omega(t_1 - t_2)] \, dt_1 \, dt_2}{2\pi T_o}. \quad (8)$$

If we change the order of integration and expectation and observe that the double integral is separable and that one integral is the conjugate of the other we get

$$S(\omega) = \lim_{T_o \to \infty} \frac{E\left[\left| \int_{-T_o/2}^{T_o/2} x(t) e^{-j\omega t} \, dt \right|^2\right]}{2\pi T_o} \quad (9)$$

which is the definition of power spectrum given by Rice.[1]

A large class of digital signals has the property

$$R(t_1 , t_2) = R(t_1 + T, t_2 + T). \quad (10)$$

Papoulis has shown that in this case $\Gamma(\omega_1 , \omega_2)$ consists of line masses

† Notice the signs in the exponential.

in the (ω_1 , ω_2)-plane. The line mass on $\omega_1 = \omega_2$ gives the average power spectrum $S(\omega)$ such that

$$\Gamma(\omega_1 , \omega_2) = \Gamma_r(\omega_1 , \omega_2) + (2\pi)^2 S(\omega_1)\, \delta(\omega_1 - \omega_2) \tag{11}$$

where $\Gamma_r(\omega_1 , \omega_2)$ has no line masses on $\omega_1 = \omega_2$. From the definition of $\Gamma(\omega_1 , \omega_2)$, equation (3), we get

$$\Gamma(\omega_1 , \omega_2) = \int_{-\infty}^{\infty} \int_{-\infty}^{\infty} R(t_1 , t_2) \exp(-j\omega_1 t_1 + j\omega_2 t_2)\, dt_1\, dt_2 . \tag{12}$$

Let

$$t_1 = t + \tau \tag{13}$$

$$t_2 = t \tag{14}$$

then

$$\Gamma(\omega_1 , \omega_2) = \int_{-\infty}^{\infty} \int_{-\infty}^{\infty} R(t + \tau, t) \cdot \exp[-j\omega_1 \tau - j(\omega_1 - \omega_2)t]\, d\tau\, dt. \tag{15}$$

We divide the t-axis in intervals of length T and get

$$\Gamma(\omega_1 , \omega_2) = \sum_{q=-\infty}^{\infty} \int_{t=qT}^{(q+1)T} \int_{\tau=-\infty}^{\infty} R(t + \tau, t) \cdot \exp[-j\omega_1 \tau - j(\omega_1 - \omega_2)t]\, d\tau\, dt. \tag{16}$$

From equation (10) it follows that we have periodicity in t; in each interval $t \in \{qT, (q + 1)T\}$ we let

$$t \to t + qT$$

and equation (16) becomes

$$\Gamma(\omega_1 , \omega_2) = \sum_{q=-\infty}^{\infty} \int_{t=0}^{T} \int_{\tau=-\infty}^{\infty} R(t + \tau, t) \exp(-j\omega_1 \tau) \cdot \exp[-j(\omega_1 - \omega_2)(t + qT)]\, d\tau\, dt \tag{17}$$

or

$$\Gamma(\omega_1 , \omega_2) = \int_{t=0}^{T} \int_{\tau=-\infty}^{\infty} R(t + \tau, t) \exp[-j\omega_1 \tau - j(\omega_1 - \omega_2)t]\, d\tau\, dt \cdot \frac{2\pi}{T} \sum_{-\infty}^{\infty} \delta\left(\omega_1 - \omega_2 - \frac{2\pi n}{T}\right). \tag{18}$$

The set of δ-functions gives us the line masses mentioned earlier. $S(\omega)$ is

the mass on $\omega_1 = \omega_2$, and from equations (18) and (11)

$$S(\omega) = \frac{1}{2\pi T} \int_{t=0}^{T} \int_{\tau=-\infty}^{\infty} R(t + \tau, t) e^{-j\omega\tau} \, d\tau \, dt. \tag{19}$$

We return to the original variables t_1 and t_2 which are absolute times. Using equations (13) and (14) we get

$$S(\omega) = \frac{1}{2\pi T} \int_{t_2=0}^{T} \int_{t_1=-\infty}^{\infty} R(t_1 , t_2) \exp [-j\omega(t_1 - t_2)] \, dt_1 \, dt_2 . \tag{20}$$

We segment the t_1-axis in intervals of length T

$$S(\omega) = \frac{1}{2\pi T} \sum_{q=-\infty}^{\infty} \int_{t_1=qT}^{(q+1)T} \int_{t_2=0}^{T} R(t_1 , t_2) \cdot \exp [-j\omega(t_1 - t_2)] \, dt_2 \, dt_1 . \tag{21}$$

The kth term of the sum is

$$S_k(\omega) = \frac{1}{2\pi T} \int_{t_1=kT}^{(k+1)T} \int_{t_2=0}^{T} R(t_1 , t_2) \exp [-j\omega(t_1 - t_2)] \, dt_1 \, dt_2 . \tag{22}$$

From the definition of autocorrelation of equation (2):

$$R(t_1 , t_2) = R^*(t_2 , t_1). \tag{23}$$

Substitute equation (23) into equation (22) and change the variables such that

$$t_1 \rightarrow t_2 - kT \quad \text{and} \quad t_2 \rightarrow t_1 - kT.$$

Because $R(t_1, t_2)$ is periodic as shown by equation (10) it follows that

$$S_k(\omega) = \frac{1}{2\pi T} \int_{t_1=-kT}^{(-k+1)T} \int_{t_2=0}^{T} R^*(t_1 , t_2) \exp [j\omega(t_1 - t_2)] \, dt_2 \, dt_1 \tag{24}$$

or

$$S_k(\omega) = S^*_{(-k)}(\omega). \tag{25}$$

We can then combine terms in equation (21) where $q > 0$ in pairs and equation (21) becomes

$$S(\omega) = \frac{1}{2\pi T} \left\{ \int_0^T \int_0^T R(t_1 , t_2) \exp [-j\omega(t_1 - t_2)] \, dt_1 \, dt_2 + 2 \operatorname{Re} \left[\sum_{q=1}^{\infty} \int_{t_1=qT}^{(q+1)T} \int_0^T R(t_1 , t_2) \exp [-j\omega(t_1 - t_2)] \, dt_1 \, dt_2 \right] \right\}. \tag{26}$$

III. DIGITAL PHASE MODULATION

Represent the signal by

$$x(t) = V_c \cos(\omega_c t + \phi(t)) \tag{27}$$

where

$$\phi(t) = \sum_{n=-\infty}^{\infty} a_n g(t - nT). \tag{28}$$

We assume that the a_n's are independent with identical probability distribution and $g(t)$ is integrable and of finite length such that $g(t) \equiv 0$ outside the time interval $\{0, pT\}$. Otherwise $g(t)$ is arbitrary.

The Appendix shows by means of transforms that the one sided spectrum of $x(t)$ is

$$S(\omega_c + \omega) = \frac{V_c^2}{2} \Gamma(\omega, \omega) \tag{29}$$

where ω is the difference between the actual frequency and the carrier frequency. $\Gamma(\omega_1, \omega_2)$ is defined by equation (3) with

$$R(t_1, t_2) = E\{\exp[j\phi(t_1) - j\phi(t_2)]\}. \tag{30}$$

If we substitute equation (28) into equation (30) and use the fact that the a_n's are independent we get

$$R(t_1, t_2) = \prod_{n=-\infty}^{\infty} E[\exp\{ja_n[g(t_1 - nT) - g(t_2 - nT)]\}]. \tag{31}$$

To show that $R(t_1 + T, t_2 + T) = R(t_1, t_2)$ let $t_1 \to t_1 + T$ and $t_2 \to t_2 + T$ and reindex such that $n \to n + 1$.

$$R(t_1 + T, t_2 + T) = \prod_{n=-\infty}^{\infty} E[\exp\{ja_{n+1}[g(t_1 - nT) - g(t_2 - nT)]\}]. \tag{32}$$

Since we assumed identical probability distributions the periodicity follows.

In order to use equation (26) we now have to evaluate $R(t_1, t_2)$ for

$$0 \leqq t_1 \leqq \infty \quad \text{and} \quad 0 \leqq t_2 \leqq T.$$

Since $t_2 \in \{0, T\}$, $g(t_2 - nT)$ will contribute in the factors when

$$-(p - 1) \leqq n \leqq 0.$$

Now $t_1 \in \{qT, (q+1)T\}$ and $g(t_1 - nT)$ will contribute when

$$-(p-1) + q \leqq n \leqq q.$$

In order to determine for which n's only one will contribute and for which n's both will contribute to the factors in equation (31) let us look at Fig. 1. We see that if $q < p$ then there will be factors where both contribute. Equation (21) becomes

$$R(t_1, t_2) = \prod_{-p+1}^{-p+q} E\{\exp[-jag(t_2 - nT]\} \cdot \prod_{-p+q+1}^{0} E(\exp\{ja[g(t_1 - nT) - g(t_2 - nT)]\}) \cdot \prod_{1}^{q} E\{\exp[jag(t_1 - nT)]\}. \tag{33}$$

In the first product we let $n \to n - p$ and in the second $n \to n - p + q$. We also let $t_1 \to t_1 + qT$ and this part of equation (26) becomes

$$\frac{1}{\pi T} \operatorname{Re}\left\{\sum_{q=1}^{p-1} e^{-iq\omega T} \int_0^T \int_0^T \prod_{n=1}^{q} [E(\exp\{jag[t_1 + (q-n)T]\}) \cdot E(\exp\{-jag[t_2 + (p-n)T]\})] \cdot \prod_{n=1}^{p-q} E[\exp(ja\{g[t_1 + (p-n)T] - g[t_2 + (p-q-n)T]\})] \cdot \exp[-j\omega(t_1 - t_2)]\, dt_1\, dt_2\right\}. \tag{34}$$

The first double integral in equation (26) we get from equation (33) with $q = 0$. Let $n \to -n$,

$$\frac{1}{2\pi T} \int_0^T \int_0^T \prod_{n=0}^{p-1} E(\exp\{ja[g(t_1 + nT) - g(t_2 + nT)]\}) \cdot \exp[-j\omega(t_1 - t_2)]\, dt_1\, dt_2\,. \tag{35}$$

We have yet to find the terms where $p \leqq q \leqq \infty$. If we look at Fig. 1, we see that

$$R(t_1, t_2) = \prod_{-p+1}^{0} E\{\exp[-jag(t_2 - nT)]\} \cdot \prod_{-p+q+1}^{q} E\{\exp[jag(t_1 - nT)]\}. \tag{36}$$

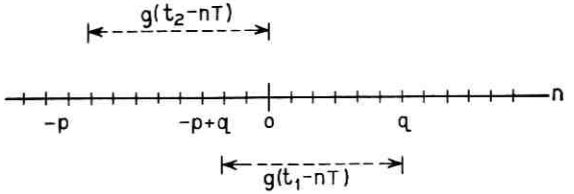

Fig. 1 — Contributions to $R(t_1, t_2)$.

In the first product let $n \to -n$, and in the second let $n \to -n + q$, and finally $t_1 \to t_1 + qT$. Substituting the result into terms in equation (26) where $q \geqq p$ we get

$$\frac{1}{\pi T}\left|\int_0^T \prod_{n=0}^{p-1} E\{\exp\,[jag(t+nT)]\}\cdot e^{-i\omega t}\,dt\right|^2 \cdot \mathrm{Re}\cdot\left[\sum_{q=p}^{\infty} e^{-iq\omega T}\right]$$

$$= \frac{1}{\pi T}\left|\int_0^T \prod_{n=0}^{p-1} E\{\exp\,[jag(t+nT)]\}e^{-i\omega t}\,dt\right|^2$$

$$\cdot\left\{\mathrm{Re}\left[\sum_{q=1}^{\infty} e^{-iq\omega T} - \sum_{q=1}^{p-1} e^{-iq\omega T}\right]\right\} \tag{37}$$

which becomes

$$\frac{1}{\pi T}\left|\int_0^T \prod_{n=0}^{p-1} E\{\exp\,[jag(t+nT)]\}e^{-i\omega t}\,dt\right|^2$$

$$\cdot\left\{\frac{\pi}{T}\sum_{m=-\infty}^{\infty}\delta\left[\omega - \frac{2\pi m}{T}\right] + \frac{1}{2} - \cos\left[\frac{(p-1)\omega T}{2}\right]\frac{\sin\left(\frac{p\omega T}{2}\right)}{\sin\frac{\omega T}{2}}\right\} \tag{38}$$

Substituting equations (35), (34), and (38) into equations (29) and (26)

$$S(\omega_c + \omega) = \frac{V_c^2}{2}\left\{\frac{1}{2\pi T}\left[\int_0^T\int_0^T \prod_{n=0}^{p-1} E(\exp\,\{ja[g(t_1+nT) - g(t_2+nT)]\}\right.\right.$$

$$\left.\cdot\exp\,[-j\omega(t_1 - t_2)]\,dt_1\,dt_2 + \left|\int_0^T \prod_{n=0}^{p-1} E\{\exp\,[jag(t+nT)]\}e^{-i\omega t}\,dt\right|^2\right.$$

$$\left\{1 - 2\cdot\cos\left[\frac{(p-1)\omega T}{2}\right]\frac{\sin\left(\frac{p\omega T}{2}\right)}{\sin\left(\frac{\omega T}{2}\right)}\right\} + 2R_e\left\{\sum_{q=1}^{p-1} e^{-iq\omega T}\right.$$

$$\cdot \int_0^T \int_0^T \prod_{n=1}^{q} [E(\exp\{jag[t_1 + (q-n)T]\})$$

$$\cdot E(\exp\{-jag[t_2 + (p-n)T]\})] \prod_{n=1}^{p-q} E[\exp(ja\{g[t_1 + (p-n)T]$$

$$- g[t_2 + (p-q-n)T]\})] \exp[-j\omega(t_1 - t_2)]\, dt_1\, dt_2 \Bigg\} \Bigg]$$

$$+ \frac{1}{T^2} \sum_{m=-\infty}^{\infty} \left| \int_0^T \prod_{n=0}^{p-1} E\{\exp[jag(t+nT)]\} \right.$$

$$\left. \cdot \exp\left(-j\frac{2\pi mt}{T}\right) dt \right|^2 \delta\left(\omega - \frac{2\pi m}{T}\right) \Bigg\} \tag{39}$$

IV. EXAMPLE OF PM SPECTRA

A complete evaluation of equation (39) is not attempted here. We compute $S(\omega_c + \omega)$ for the case when $g(t)$ is a rectangular pulse of duration $\tau < T$, and height 1. We assume that a has r levels which are equidistant and equally probable such that

$$a^{(k)} = \alpha_0 + \frac{k-1}{r}\alpha \tag{40}$$

$$P\{a^{(k)}\} = \frac{1}{r}. \tag{41}$$

First we rewrite equation (39) with p = 1:

$$S(\omega_c + \omega) = \frac{V_c^2}{2}\left[\frac{1}{2\pi T}\int_0^T \int_0^T E(\exp\{ja[g(t_1) - g(t_2)]\}) \right.$$

$$\cdot \exp[-j\omega(t_1 - t_2)]\, dt_1\, dt_2$$

$$+ \frac{1}{T^2}\left| \int_0^T E[e^{jag(t)}] \exp[-jwt]\, dt \right|^2$$

$$\left. \cdot \left(\sum_{m=-\infty}^{\infty} \delta\left\{\omega - \frac{2\pi m}{T}\right\} - \frac{T}{2\pi}\right)\right]. \tag{42}$$

The expected values in equation (42) will be

$$E(\exp\{ja[g(t_1) - g(t_2)]\})$$

$$= \frac{1}{r}\sum_{k=1}^{r} \exp\left\{j\left[\alpha_0 + \frac{k-1}{r}\alpha\right][g(t_1) - g(t_2)]\right\} \tag{43}$$

and

$$E[e^{ja_0(t)}] = \frac{1}{r}\sum_{k=1}^{r} \exp\left[j\left(\alpha_o + \frac{k-1}{r}\alpha\right)g(t)\right]. \tag{44}$$

From equations (43) and (44) it follows that

$$\int_0^T \int_0^T E(\exp\{ja[g(t_1) - g(t_2)]\}) \exp[-j\omega(t_1 - t_2)]\, dt_1\, dt_2$$
$$= \frac{1}{r}\sum_{k=1}^{r} \left| \int_0^T \exp\left[j\left(\alpha_o + \frac{k-1}{r}\alpha\right)\right]g(t) - j\omega t\, dt \right|^2 \tag{45}$$

since we can separate the integrals and because the integral over t_2 is the conjugate of the integral over t_1. Also

$$\left| \int_0^T E[e^{ja_0(t)}]e^{-j\omega t}\, dt \right|^2$$
$$= \frac{1}{r^2}\left| \sum_{k=1}^{r} \int_0^T \exp\left[j\left(\alpha_o + \frac{k-1}{r}\alpha\right)\right]g(t) - j\omega t\, dt \right|^2. \tag{46}$$

Let us set

$$\int_0^T \exp\left[j\left(\alpha_o + \frac{k-1}{r}\alpha\right)g(t) - j\omega t\right] dt = F_k(\omega) \tag{47}$$

Then equation (42) becomes

$$S(\omega_c + \omega) = \frac{V_c^2}{2}\left\{\frac{1}{2\pi T}\left[\sum_{k=1}^{r}\frac{1}{r} \mid F_k(\omega) \mid^2 - \left| \sum_{k=1}^{r}\frac{1}{r}F_k(\omega) \right|^2\right]\right.$$
$$\left. + \frac{1}{T^2}\sum_{m=-\infty}^{\infty}\left| \sum_{k=1}^{r}\frac{1}{r}F_k\left(\frac{2\pi m}{T}\right)\right|^2 \delta\left(\omega - \frac{2\pi m}{T}\right)\right\}. \tag{48}$$

With $g(t) = 1$ for $t \in \{0, \tau\}$ and 0 for $t \in \{\tau, T\}$ we get (after some trigonometric manipulations)

$$S(\omega_c + \omega) = \frac{V_c^2}{2}\left[\frac{\tau^2}{2\pi T}\left[\frac{\sin\left(\frac{\omega\tau}{2}\right)}{\frac{\omega\tau}{2}}\right]^2\left\{1 - \frac{1}{r^2}\left[\frac{\sin\left(\frac{\alpha}{2}\right)}{\sin\left(\frac{\alpha}{2r}\right)}\right]^2\right\}\right.$$
$$\left. + \sum_{m=-\infty}^{\infty}\left[\frac{\tau^2}{r^2T^2}\left[\frac{\sin\left(\frac{m\pi\tau}{T}\right)}{\frac{m\pi\tau}{T}}\right]^2\left[\frac{\sin\left(\frac{\alpha}{2}\right)}{\sin\left(\frac{\alpha}{2r}\right)}\right]^2 + \left(1 - \frac{\tau}{T}\right)^2\right.\right.$$

$$\cdot\left[\frac{\sin m\pi\left(1-\frac{\tau}{T}\right)}{m\pi\left(1-\frac{\tau}{T}\right)}\right]^2+\frac{2}{r}\frac{\tau}{T}\left(1-\frac{\tau}{T}\right)\frac{\sin\left(\frac{m\pi\tau}{T}\right)}{\frac{m\pi\tau}{T}}\cdot\frac{\sin\left[m\pi\left(1-\frac{\tau}{T}\right)\right]}{m\pi\left(1-\frac{\tau}{T}\right)}$$

$$\cdot\frac{\sin\left(\frac{\alpha}{2}\right)}{\sin\left(\frac{\alpha}{2r}\right)}\cdot\cos\left[m\pi+\alpha_o+\frac{\alpha(r-1)}{2r}\right]\delta\left[\omega-\frac{2\pi m}{T}\right]\Bigg]\Bigg]\cdot \tag{49}$$

The continuous part of the spectrum is independent of α_o. Only the random deviations from α_o, and the pulse length determine the continuous part of the spectrum. The term α_o is related to the periodicity of the signal and consequently the spectrum spikes will be functions of α_o.

There are some interesting special cases of equation (49). If $(\alpha/r) = n\cdot 2\pi$ then the continuous part of the spectrum disappears. We would expect this because from equation (40) it follows that during each pulse a phase excursion of α_o plus an integer number of 2π is made. This is the same as modulating with a periodic signal where in one period we have $\alpha_o g(t)$.

If $\tau \to T$ all spikes except the carrier spike go to zero; this gives

$$S(\omega_c+\omega)=\frac{V_c^2}{2}\left[\frac{T}{2\pi}\left[\frac{\sin\left(\frac{\omega T}{2}\right)}{\frac{\omega T}{2}}\right]^2\left\{1-\frac{1}{r^2}\left[\frac{\sin\left(\frac{\alpha}{2}\right)}{\sin\left(\frac{\alpha}{2r}\right)}\right]^2\right\}\right.$$

$$\left.+\frac{1}{r^2}\left[\frac{\sin\left(\frac{\alpha}{2}\right)}{\sin\left(\frac{\alpha}{2r}\right)}\right]^2\delta(\omega)\right] \tag{50}$$

which is a familiar result. This is independent of α_o because in this case α_o is just a constant phase angle added to the carrier at all times.

It is interesting to note that if $\alpha = n\cdot 2\pi$, the carrier spike will also disappear.

V. CONCLUSION

There is a large class of nonstationary processes which yield signals with periodicity in the two dimensional autocorrelation function such that $R(t_1+T, t_2+T) = R(t_1, t_2)$. Such a class includes many of the common digital signals.

A simple expression has been derived for the power spectrum of such a signal. It was done by means of the double Fourier transform which relates the spectrum of any signal to its autocorrelation function. For this class of signals the method is very powerful.

The results were applied to get the general expression for the power spectrum of a wave phase modulated with a pulse stream $\sum_{-\infty}^{\infty} a_n g(t - nT)$. The only restrictions on the pulse stream are that the a_n's are independent and have identical probability distributions and, $g(t)$ is integrable and of finite length. As an example a rectangular pulse of length $\tau < T$ was considered.

The same method can be used for digital FM to arrive at the expression given by Anderson and Salz.[3] It can also be shown that the expression given here for PM goes into the one for FM given in Ref. 3 with the accrued phase per pulse equal to 0. This corresponds to $\alpha_r = 0$ in Ref. 3, a case which was not treated there. We get this FM case by substituting

$$\omega_d \int_0^t g(t')\, dt'$$

for $g(t)$ in our equation (39) where ω_d is a frequency deviation parameter defined in Ref. 3.

APPENDIX

Carrier Translation

An angle modulated signal is represented by

$$x(t) = V_c \cos [\omega_c t + \phi(t)]. \tag{51}$$

The autocorrelation function of $x(t)$ is

$$R_x(t_1 , t_2) = E[x(t_1) \cdot x^*(t_2)] \tag{52}$$

which becomes

$$\begin{aligned} R_x(t_1 , t_2) = \frac{V_c^2}{4} &(\exp [j\omega_c(t_1 + t_2)]E\{\exp [j\phi(t_1) + j\phi(t_2)]\} \\ &+ \exp [-j\omega_c(t_1 + t_2)]E\{\exp [-j\phi(t_1) - j\phi(t_2)]\} \\ &+ \exp [j\omega_c(t_1 - t_2)]E\{\exp [j\phi(t_1) - j\phi(t_2)]\} \\ &+ \exp [-j\omega_c(t_1 - t_2)]E\{\exp [-j\phi(t_1) + j\phi(t_2)]\}). \end{aligned} \tag{53}$$

The average energy in the two first terms will for most practical cases of modulation go to zero. To show this we take the double Fourier transform of the first term

$$\Gamma_1(\omega_1 , \omega_2) = \frac{V_c^2}{4} \mathfrak{F}_2\{\exp [j\omega_c(t_1 + t_2)]\} * \mathfrak{F}_2(E\{\exp [j\phi(t_1) + j\phi(t_2)]\}) \tag{54}$$

or

$$\Gamma_1(\omega_1 , \omega_2) = \frac{V_c^2}{4} (2\pi)^2 \cdot \delta(\omega_1 - \omega_c) \cdot \delta(\omega_2 + \omega_c) * \mathfrak{F}_2(E\{\exp [j\phi(t_1) + j\phi(t_2)]\}) \tag{55}$$

where $\mathfrak{F}_2$ is a double Fourier transform operator and * means convolution in both t_1 and t_2 . The plus sign in the second δ-function comes from the plus sign in front of ω_2 in the definition of the double Fourier transform of equation (3). Equation (55) shows that we can find $\Gamma_1(\omega_1 , \omega_2)$ by first finding

$$\mathfrak{F}_2(E\{\exp [j\phi(t_1) + j\phi(t_2)]\})$$

and then move it in the (ω_1 , ω_2)-plane so that the point (0, 0) falls at $(\omega_c , -\omega_c)$. (See Fig. 2.) To find the average energy we set $\omega_1 = \omega_2$. We see then, if

$$\mathfrak{F}_2(E\{\exp [j\phi(t_1) + j\phi(t_2)]\})$$

does not have any significant mass density for frequencies of the order of ω_c there will be no contribution from $\Gamma_1(\omega_1 , \omega_2)$ falling on the line $\omega_1 = \omega_2$. This will be the assumption here, that is, the modulating functions do not produce sidebands as far as ω_c away from the carrier. Then it also follows that the second term in equation (53) will not contribute.

Now let us set

$$E\{\exp [j\phi(t_1) - j\phi(t_2)]\} = R(t_1 , t_2). \tag{56}$$

Thus

$$E\{\exp [-j\phi(t_1) + j\phi(t_2)]\} = R^*(t_1 , t_2). \tag{57}$$

If

$$\Gamma(\omega_1 , \omega_2) = \mathfrak{F}_2[R(t_1 , t_2)] \tag{58}$$

then from equation (3) it follows

$$\mathfrak{F}_2[R^*(t_1 , t_2)] = \Gamma(-\omega_2 , -\omega_1). \tag{59}$$

Taking the double Fourier transform of equation (53) then yields

$$\Gamma_x(\omega_1 , \omega_2) = \frac{V_c^2}{4} (2\pi)^2 \cdot [\delta(\omega_1 - \omega_c) \cdot \delta(\omega_2 - \omega_c) * \Gamma(\omega_1 , \omega_2) + \delta(\omega_1 + \omega_c) \cdot \delta(\omega_2 + \omega_c) * \Gamma(-\omega_2 , -\omega_1)]. \quad (60)$$

If we look at Fig. 2 we see that the convolution just means sliding $\Gamma(\omega_1 , \omega_2)$ and $\Gamma(-\omega_2 , -\omega_1)$ along the line $\omega_1 = \omega_2$. We want the portion of $\Gamma_x(\omega_1 , \omega_2)$ that is located on the line. The sliding process takes the portions of $\Gamma(\omega_1 , \omega_2)$ and $\Gamma(-\omega_2 , -\omega_1)$ that are already on the line and moves them to the points (ω_c , ω_c) and $(-\omega_c , -\omega_c)$, respectively. Setting $\omega_1 = \omega_2 = \omega_c + \omega$ in equation (60) and performing the convolution we get

$$\Gamma_x(\omega_c + \omega, \omega_c + \omega) = \frac{V_c^2}{4} [\Gamma(\omega, \omega) + \Gamma(-\omega, -\omega)]. \quad (61)$$

The second part in equation (61) is just the mirror image of the first and the one-sided spectrum becomes

$$S(\omega_c + \omega) = \frac{V_c^2}{2} \Gamma(\omega, \omega) \quad (62)$$

where

$$\Gamma(\omega_1 , \omega_2) = \mathfrak{F}_2(E\{\exp [j\phi(t_1) - j\phi(t_2)]\}).$$

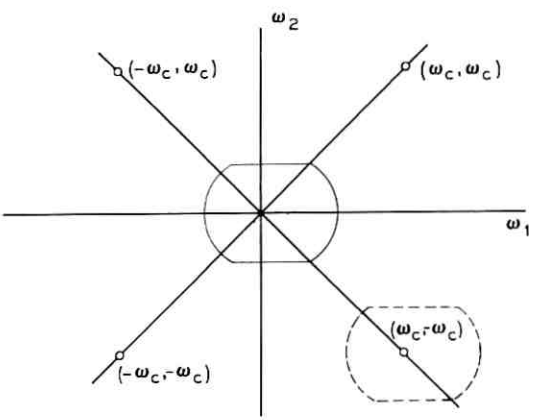

Fig. 2 — Carrier translation.

REFERENCES

1. Rice, S. O., "Mathematical Analysis of Random Noise," B.S.T.J., *23*, No. 3 (July 1944), pp. 282–332.
2. Papoulis, A., *Probability, Random Variables, and Stochastic Processes*, New York: McGraw-Hill, 1965, pp. 440–451.
3. Anderson, R. R. and Salz, J., "Spectra of Digital FM," B.S.T.J., *44*, No. 6 (July–August 1965), pp. 1165–1189.

PSK Error Performance with Gaussian Noise and Interference

By ARNOLD S. ROSENBAUM

(Manuscript received September 13, 1968)

A single, constant amplitude, in-band, additive interference is included in the analysis of detecting phase shift keyed signals in gaussian noise. For coherent detection we give a method applicable to any M-phase system, and evaluate the symbol error probability for $M = 2, 3$, and 4. For differential detection we treat the important cases $M = 2, 4, 8$, and 16, offering comprehensive numerical results for each.

The analysis in each case is based on a single sinusoid with random phase adding to the noisy phase shift keyed signal. The results are then interpreted to include an angle modulation impressed on the continuous wave interferer. The receiver consists of an ideal phase discriminator with a perfect slicer. The channel is also assumed ideal in that intersymbol interference is not considered.

I. INTRODUCTION

Phase shift keying (psk) is becoming more popular as a modulation scheme for transmitting digital information. Lately much analysis has been done for both coherent and differentially coherent detection. Unfortunately the analyses done to date have generally considered only two signal degradations: channel anomalies (such as distortion, gain and delay variations, and so on) and thermally generated noise modeled by a gaussian random process. This article considers the effects of a spurious signal, or interference, falling in the band of the desired signal, as well as gaussian noise. It is understood that both the noise and the interference additively corrupt the desired signal; these are the only perturbing factors.

For coherent detection, the phase probability density function for the received composite of signal, noise, and interference is found. From this, the theoretical error probability may be evaluated for

any M-phase system. We give comprehensive numerical results for the important cases, $M = 2, 3, 4$.

For differential detection we present analysis and results for $M = 2$, 4, 8, and 16. In the binary case a simple closed form solution was found which yields both a good approximation and exact bounds to the actual error probability. The solutions to the multilevel $M > 2$ differential detection problem, which are exact, required machine computation of a double integral; complete numerical results are given.

Finally, we draw general comparisons between coherent and differential detection error performance as affected by interference.

II. SIGNALS, NOISE, AND INTERFERENCE

A phase shift keyed signal has the form (ignoring any amplitude function)

$$s(t) = \cos [2\pi f_s t + \phi_s(t)] \tag{1}$$

where we choose to normalize the peak signal amplitude to unity. The digital modulation is carried in the angle of s by $\phi_s(t)$, which assumes discrete values from a set of M equally spaced points in $[0, 2\pi]$ at the sample times T seconds apart. Thus the Nth message or baud is modulated by

$$\phi_s(NT) = \frac{2\pi k}{M}, \qquad k = 0, 1, 2, \cdots, M - 1 \tag{2}$$

where each of the M values of k is equally probable.

For a coherent receiver an M-ary symbol is transmitted in one baud by the value of k. For a differential detection receiver the information is transmitted by the changes in k (or carrier phase) between adjacent bauds.

The noise is presumed to originate thermally and is therefore modeled in the usual fashion by a stationary zero mean gaussian random process with uniform spectral density. At the output of a symmetrical bandpass filter the noise voltage may be written as[1]

$$n(t) = u(t) \cos (2\pi f_s t) - v(t) \sin (2\pi f_s t) \tag{3}$$

where u and v are low-pass, stationary, independent, zero mean gaussian random processes with ensemble averages

$$\langle n^2 \rangle_{av} = \langle u^2 \rangle_{av} = \langle v^2 \rangle_{av} = \sigma^2, \tag{4}$$

equal to the noise power.

In the differential detection analysis we make the further restriction that the noise process autocorrelation vanish at the baud interval, thus

$$R_{nn}(T) = 0. \tag{5}$$

This assures the four gaussian random variables

$$u(t_0),\ u(t_0 + T),\ v(t_0),\ v(t_0 + T)$$

to be uncorrelated and hence independent.[2]

Interference shall consist of a constant amplitude, possibly angle modulated, sinusoid which lies within the bandwidth of the detector. It is assumed to originate independently of the signal, and so it is natural that its phase relationship to the signal is random with all angles equally probable. Therefore let

$$i(t) = b \cos [2\pi f_i t + \phi_i(t) + \Gamma] \tag{6}$$

which has a peak value of b, and is angle modulated by ϕ_i. The arbitrary phase angle Γ, independent of ϕ_i, is a random variable whose probability density function is $(2\pi)^{-1}$ when reduced modulo 2π.

For coherent detection, where the interference is observed only once per symbol, the random phase variable Γ vitiates the modulation ϕ_i because the sum $(\phi_i + \Gamma)$ is distributed exactly as if it were uniform. This is discussed in Section III.

III. COHERENT DETECTION

An ideal phase discriminator is assumed which compares the received wave (composed of signal, noise, and interference) with the unmodulated signal carrier (the reference) and produces instantly the signed phase difference between the two inputs.

The detector examines the discriminator output and announces an estimate of the transmitted symbol. The detector operates with no timing error and with zero width decision thresholds. Using maximum likelihood detection based on equal *a priori* symbol probabilities, the thresholds are at π/M, $(3\pi)/M$, . . . , $[(2M - 1)\pi]/M$. In a phasor diagram these thresholds correspond to $(2\pi)/M$ angular sections centered about the M signal positions.

The approach used to find Pe, the probability of a symbol error, is to find the probability density function of the phase of the received composite $(s + n + i)$, and then integrate the density over the error regions.

We first notice that the phase angle of the interference relative to the signal is, from equations (1) and (6),

$$\Phi(t) \equiv 2\pi(f_i - f_s)t + \phi_i(t) - \phi_s(t) + \Gamma \tag{7}$$

where Γ is independent of the other terms on the right-hand side. Since Γ is uniformly distributed modulo 2π, the relative interference phase process $\Phi(t)$ is also uniformly distributed modulo 2π. This is a general result for the modulo addition of several variables, one of which is uniform.[3]

Figure 1 is a phasor diagram of the receiver input components, signal, interference, and noise, at a sample time t_0. The phase reference is $2\pi f_s t + \phi_s$ so that the signal lies along the reference (vertical) axis. The orthogonal noise phasors are assumed to be at angles 0 and $\pi/2$, relative to the signal. We seek the probability density function of the resultant angle A, and begin by considering the two dimensional joint probability density function of the cartesian coordinates of the resultant phasor. Conditioned on Φ, it is clearly jointly gaussian with means

$$\langle x \rangle_{av} = b \sin \Phi, \qquad \langle y \rangle_{av} = 1 + b \cos \Phi \tag{8}$$

so that

$$f_{XY}(x, y \mid \phi) = \frac{1}{2\pi\sigma^2} \exp\left\{-\frac{1}{2\sigma^2}[(x - b\sin\phi)^2 + (y - 1 - b\cos\phi)^2]\right\}. \tag{9}$$

Eliminating the Φ dependency gives

$$f_{XY}(x, y) = \frac{\exp\left\{-\frac{1}{2\sigma^2}[x^2 + (y-1)^2 + b^2]\right\}}{(2\pi\sigma)^2} \cdot \int_0^{2\pi} \exp\left\{\frac{b}{\sigma^2}[x^2 + (y-1)^2]^{\frac{1}{2}} \cos(\phi + \eta)\right\} d\phi \tag{10}$$

where $\eta = \tan^{-1}[(y-1)/x]$ is not a function of ϕ.

This integrates directly to

$$f_{XY}(x, y) = \frac{1}{2\pi\sigma^2} \exp\left\{-\frac{1}{2\sigma^2}[x^2 + (y-1)^2 + b^2]\right\} \cdot I_0\left\{\frac{b}{\sigma^2}[x^2 + (y-1)^2]^{\frac{1}{2}}\right\} \tag{11}$$

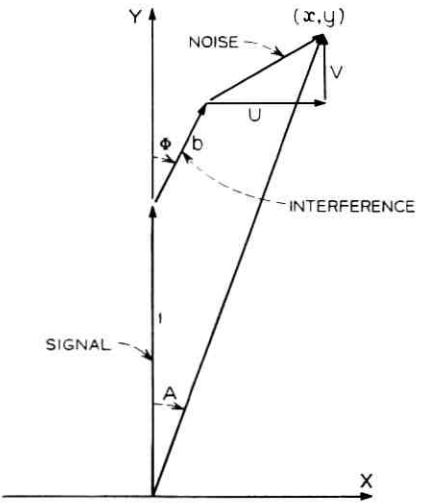

Fig. 1 — Phasor diagram of the signal, noise, and interference components at a sample time t_0.

where I_0 is the zero order modified Bessel function of the first kind.

We now convert equation (18) to polar coordinates through the usual transformation

$$x = r \sin \alpha \quad \text{and} \quad y = r \cos \alpha \tag{12}$$

which has the Jacobian r. Then the polar coordinate two-dimensional density is integrated over all radius values to yield the desired probability density function of the angle.

$$f_A(\alpha) = \frac{1}{2\pi\sigma^2} \int_0^\infty \exp\left\{-\frac{1}{2\sigma^2}[r^2 + b^2 + 1 - 2r\cos\alpha]\right\} \cdot I_0\left[\frac{b}{\sigma^2}(r^2 + 1 - 2r\cos\alpha)^{\frac{1}{2}}\right] r\, dr. \tag{13}$$

The above integration has been done numerically to generate exact $f_A(\alpha)$ curves for several values of

$-20 \log_{10}[2^{\frac{1}{2}}\sigma]$ = carrier to noise ratio in dB (CNR),

$-20 \log_{10} b$ = carrier to interference ratio in dB (CIR).

It is clear from equation (13) that $f_A(\alpha)$ has at least the symmetries of cos α.

Figure 2 offers typical families of f_A probability density function

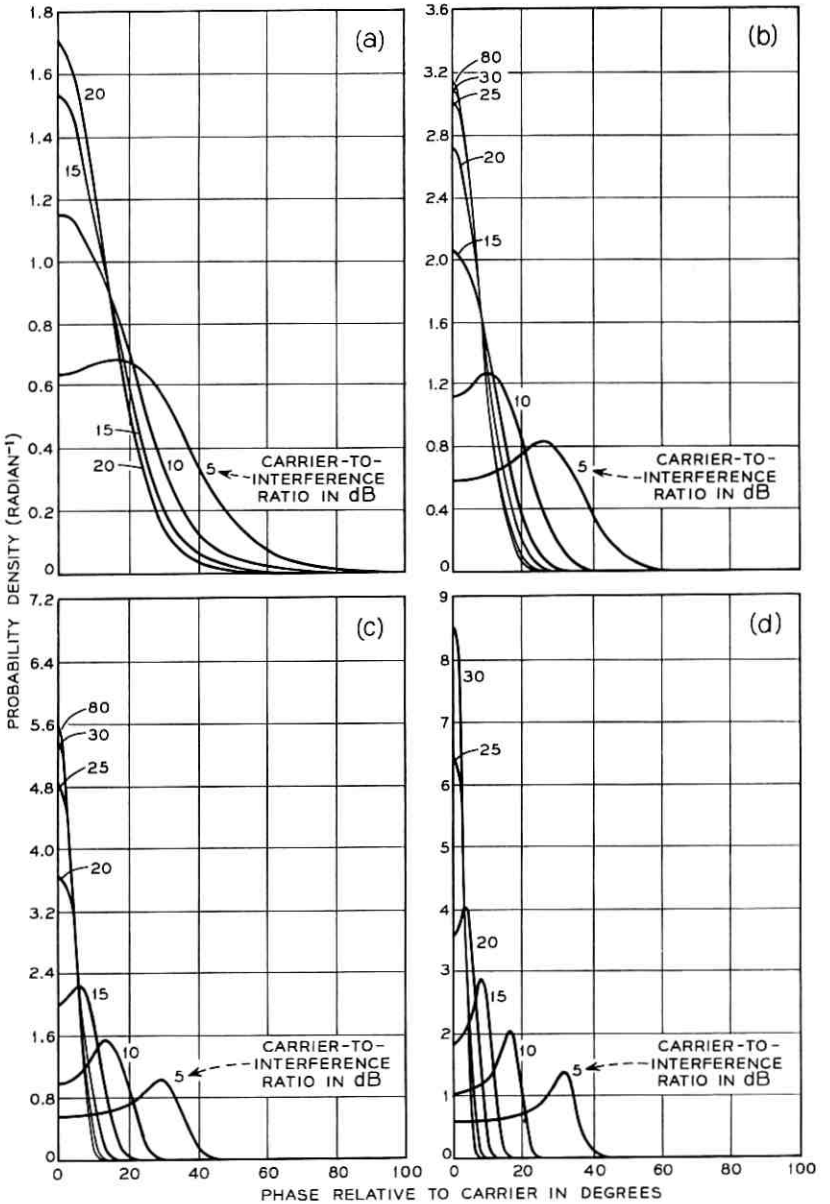

Fig. 2 — Probability density function of the phase of $s + n + i$ for various CIR values. (a) CNR = 10 dB, (b) CNR = 15 dB, (c) CNR = 20 dB, (d) CNR = 25 dB.

curves for representative CNR values. As the interference amplitude increases it is seen to control or to affect the shape of the curve to a greater degree. At high interference levels a saddle-like shape appears with peaks at roughly $\tan^{-1}b$, as one would expect in the absence of noise.

Since equation (13) is the probability density function of the angle of the complete receiver input, and since the probability of a symbol error is the probability that A lies outside the region $[-\pi/M, \pi/M]$ at t_0, we have

$$\mathrm{Pe} = \int_{-\pi}^{-\pi/M} f_A(\alpha)\, d\alpha + \int_{\pi/M}^{\pi} f_A(\alpha)\, d\alpha \tag{14}$$

which by symmetry is

$$\mathrm{Pe} = 2 \int_{\pi/M}^{\pi} f_A(\alpha)\, d\alpha. \tag{15}$$

Again, integral (15) was done numerically (a simple summation of the f_A data) for practical combinations of CNR, CIR, and for $M = 2, 3$, and 4. The results appear in Figs. 3–5.*

The above method, which employs two (rather simple) machine integrations, yields exact results but at the expense of not generating useful expressions for Pe. Therefore we now indicate one approach which yields Pe for $M = 2$, and bounds Pe for $M > 2$, as a convergent series. We begin by considering binary reception.

Referring back to Fig. 1, an error is made if $|\alpha| > 90°$ or, equivalently, if the resultant resides in the lower half plane $y < 0$. Then for fixed Φ,

$$\mathrm{Pe} \mid \Phi = (2\pi\sigma^2)^{-\frac{1}{2}} \int_{-\infty}^{0} \exp\left[-\frac{1}{2\sigma^2}(y - 1 - b\cos\phi)^2\right] dy$$

$$= \tfrac{1}{2}\,\mathrm{erfc}\left(\frac{1 + b\cos\phi}{(2)^{\frac{1}{2}}\sigma}\right). \tag{16}$$

Averaging over the uniformly weighted Φ gives

$$\mathrm{Pe} = \frac{1}{\pi}\int_0^{\pi} \tfrac{1}{2}\,\mathrm{erfc}\left(\frac{1 + b\cos\phi}{(2)^{\frac{1}{2}}\sigma}\right) d\phi. \tag{17}$$

This integral, which is virtually the cumulative distribution function of a sine wave of amplitude b plus gaussian noise of variance σ^2

* The abscissa values are true carrier-to-noise power ratios, and are not adjusted to reconcile bandwidth to bit-rate differences. One may do this by subtracting 2 dB (3 dB) from the abscissa values for $M = 3(4)$.

(evaluated at -1), has been examined by Rice[4] and others. It can be evaluated by expanding the integrand in a Taylor series about $(2\sigma^2)^{-\frac{1}{2}}$ and then integrating term by term. If the interference is small, $b \ll 1$, only the first several terms need be retained for reasonable accuracy.

The Pe values obtained for Binary may be used to bound the symbol Pe for $M > 2$. The decision thresholds are at $\pm\pi/M$ for the M-ary receiver. The error region consists of the union of two half planes formed by the extended detector thresholds. The probability that the resultant

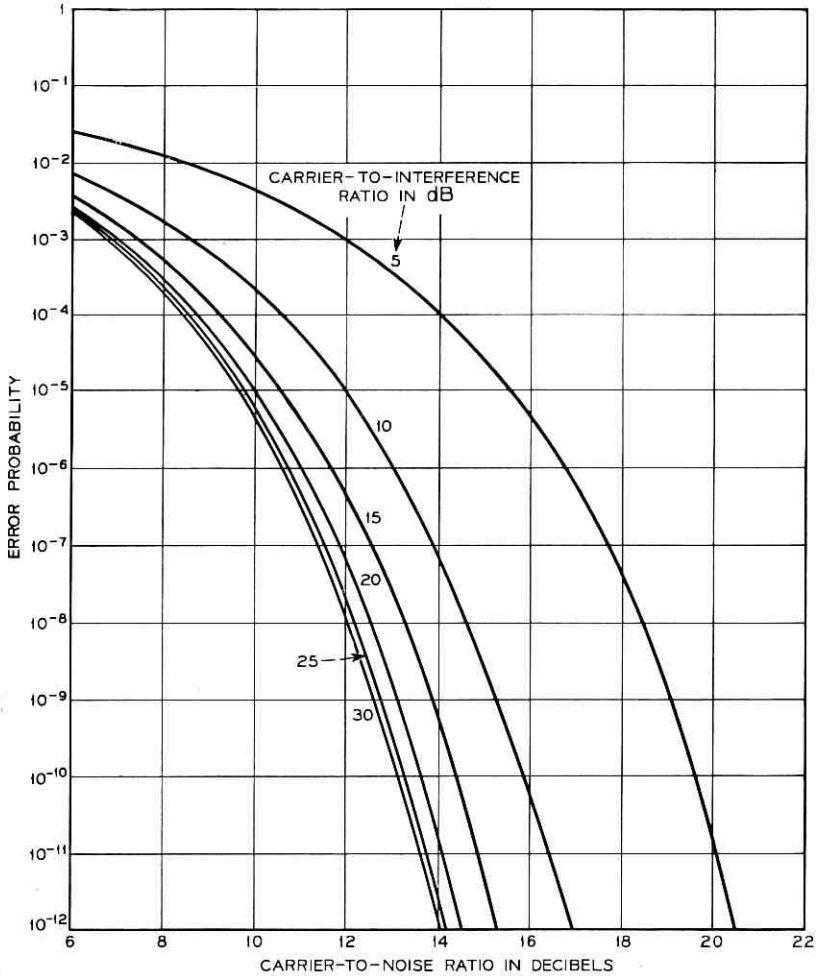

Fig. 3 — Binary ($M = 2$) Pe versus CNR. Coherent detection.

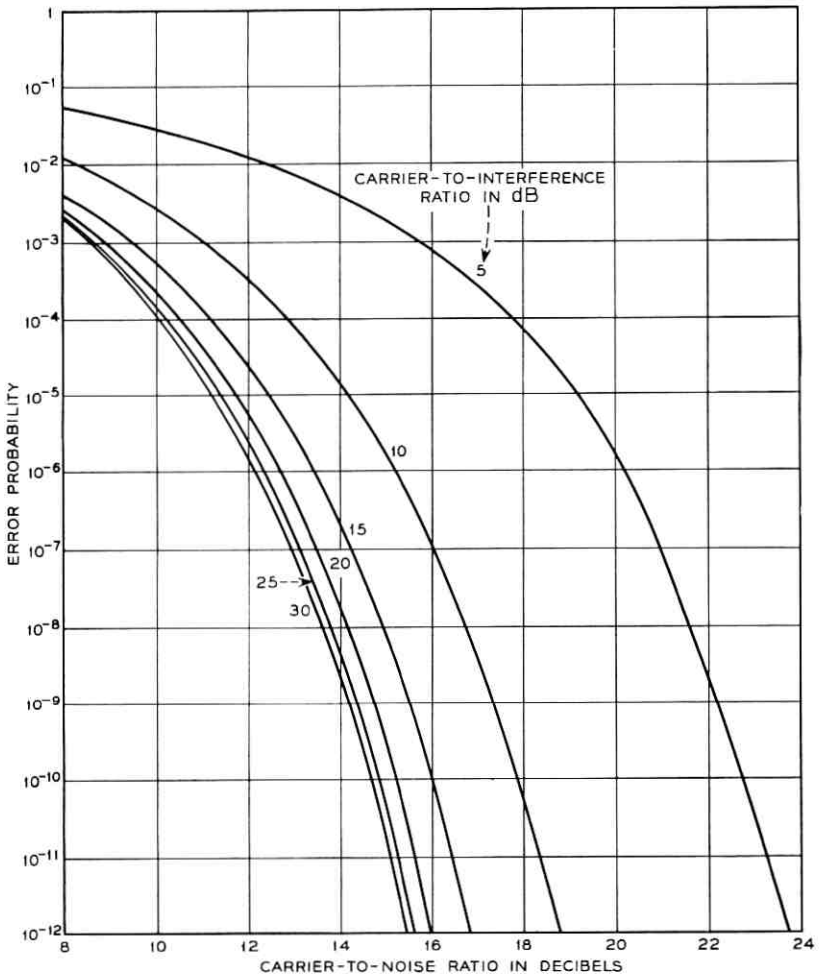

Fig. 4 — Ternary ($M = 3$) Pe versus CNR. Coherent detection.

phasor terminates in the error region, Pe, is thus bounded by the probability of terminating in either half plane. As M increases, the bound becomes a good approximation* because the size (hence the relative probability) of the doubly counted intersection decreases rapidly with M.[5] By symmetry, the probability of terminating in either half plane is twice that of one half plane.

* The approximation improves with CNR also.

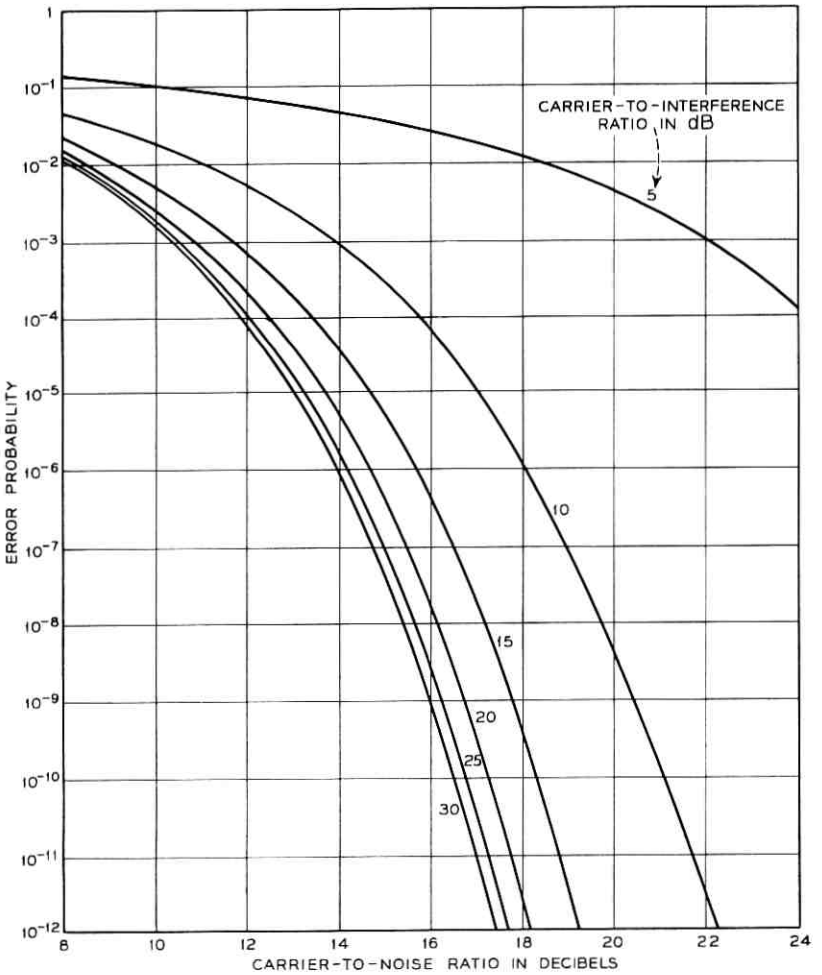

Fig. 5 — Quaternary ($M = 4$) Pe versus CNR. Coherent detection.

The probability of one half plane is related to the binary Pe very simply. The distance to the boundary from (0, 1) is sin (π/M). If now the interference phasor and noise phasor were scaled by the same factor, we see that the probability of the half plane is just the binary Pe with interference amplitude b sin (π/M) and noise variance $[\sigma \sin (\pi/M)]^2$.*

* The author is grateful to S. O. Rice for suggesting this notion.

Therefore we have the interesting relationship

$$\text{Pe}\left(M > 2,\ \sigma \sin \frac{\pi}{M},\ b \sin \frac{\pi}{M}\right) \leqq 2\ \text{Pe}\ (M = 2,\ \sigma, \pm b) \qquad (18)$$

which means that twice a given binary Pe value is an upper bound (or approximation) to an M-ary Pe where the binary CNR and CIR values are each increased by $-20 \log \sin (\pi/M)$ dB.

IV. DIFFERENTIAL DETECTION—BINARY

This type of detection has become widely considered lately because it eliminates the requirement of phase synchronism between the transmitter and receiver. The price one pays for nonsynchronous detection, however, is poorer performance.

The analysis for differential detection is complicated by the fact that the phase reference, being the previous signal, is subject to the same corruptions as the present signal being phase detected. (For the noise-only case, an exact solution in closed form is available for binary, and good approximations exist for $M \geqq 4$.) We begin with an analysis for binary differential psk (d-psk), considering again a single CW interference in addition to noise, which yields in closed form both bounds on Pe and a good approximation.

We are concerned with the reception of two successive bauds, where the data is encoded in the phase change of the signal. Arbitrarily, let no phase change represent a "0" and a π phase change represent a "1." For convenience, we will refer to the signal during a baud interval as a "pulse" of carrier at a certain phase angle, although in a pure phase modulated (PM) system the signal would not consist of carrier pulses.

From previous assumptions, the noise corrupting each signal pulse acts independently; the interference at two adjacent sample times t_0 and $t_0 + T$ does not. This dependency may be summarized by an angle

$$\theta \equiv 2\pi(f_i - f_s)T$$

which is the relative phase slip of the interference from one sample instant to the next. Assume, for the present, that the interference modulation is absent.

We will use the same equally spaced detection thresholds as in the coherent psk analysis. Ignoring interference, the probability of error in d-psk is not data dependent because of obvious symmetries.

However, the addition of interference destroys that symmetry, and causes Pe to be strongly data dependent for a given θ. Fortunately, however, the error probability for only one symbol (that is, "0" or "1") needs to be found because the probability of error for the other symbol(s) is derived directly from it. An over-all probability of error is then found by averaging the individual symbol error probabilities with equal weighting.

Consider the transmission of a "0" whereby two carrier pulses of the same phase are sent. A "double exposure" phasor diagram, Fig. 6, pictures the signal, noise, and interference components at the two successive sample instants t_0 and $t_0 + T$. The interference at t_0 assumes an angle ϕ relative to the signal, where ϕ is random and uniformly distributed in $[0, 2\pi]$. At time $t_0 + T$ the interference has progressed to an angle $\phi + \theta$.

The noise phasor amplitudes are the random variables

$$U_d \equiv u(t_0), \quad V_d \equiv v(t_0), \quad U \equiv u(t_0 + T), \quad \text{and} \quad V \equiv v(t_0 + T) \tag{19}$$

which we recall are independent, equal variance, zero mean gaussians.

The two resultant phasors, Z and Z_d, are the actual phase discriminator inputs; the output being their phase difference, δ. Since a

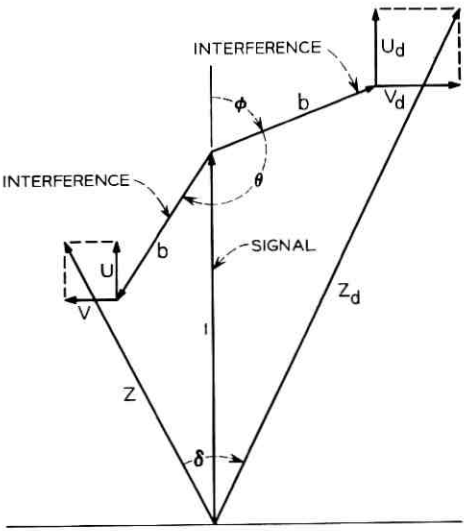

Fig. 6 — Signal, interference, and noise phasors at successive sample times t_0 and $t_0 + T$ for a transmitted "0."

"0" is transmitted, the probability of error is

$$\text{Pe} \mid \text{"0"} = \Pr\left\{ \mid \delta \mid > \frac{\pi}{2} \right\}, \qquad -\pi < \delta \leqq \pi \tag{20}$$

which is equivalent to $\Pr\{\cos \delta < 0\}$.

Also, because

$$\cos \delta = \frac{\text{Re}\,[ZZ_d^*]}{\mid Z \mid \mid Z_d \mid} \tag{21}$$

and the denominator is nonnegative, we have alternatively

$$\text{Pe} \mid \text{"0"} = \Pr\{\text{Re}\,[ZZ_d^*] < 0\}. \tag{22}$$

We now employ a technique used by Stein which leads to a closed form solution to equation (22).[6] Based on the simple identity

$$\text{Re}\,[ZZ_d^*] = \left| \frac{Z + Z_d}{2} \right|^2 - \left| \frac{Z - Z_d}{2} \right|^2 \tag{23}$$

we see that

$$\text{Pe} \mid \text{"0"} = \Pr\{\mid Z + Z_d \mid < \mid Z - Z_d \mid\} \tag{24}$$

For economy of notation we let

$$\begin{aligned} \Sigma &\equiv Z + Z_d = U + U_d + i(V + V_d) + C(\Sigma) \\ \Delta &\equiv Z - Z_d = U - U_d + i(V - V_d) + C(\Delta) \end{aligned} \tag{25}$$

where $C(\,)$ denotes the nonrandom components,* that is,

$$\begin{aligned} C(\Sigma) &= b[\sin \phi + \sin (\phi + \theta)] \\ &\quad + i\{2 + b[\cos \phi + \cos (\phi + \theta)]\} \\ C(\Delta) &= b[\sin (\phi + \theta) - \sin \phi] + ib[\cos (\phi + \theta) - \cos \phi]. \end{aligned} \tag{26}$$

Thus Σ and Δ are complex (two dimensional) random variables whose jointly gaussian orthogonal components have equal variance $2\sigma^2$. We are concerned with the magnitudes, $\mid \Sigma \mid$ and $\mid \Delta \mid$, often referred to as a Ricean random variable.

The probability density function (of $\mid \Sigma \mid$, for example) is the well known result for the envelope of sine wave plus noise[4]

$$f_{\mid \Sigma \mid}(r) = \frac{r}{2\sigma^2} \exp\left[- \frac{r^2 + \mid C(\Sigma) \mid^2}{4\sigma^2} \right] I_0\left[\frac{r \mid C(\Sigma) \mid}{2\sigma^2} \right]. \tag{27}$$

* θ is constant and we have conditioned the solution on ϕ.

Furthermore, $|\Sigma|$ and $|\Delta|$ are independent by the following argument. $U + U_d$ is independent of $V - V_d$. Consider $U + U_d$ and $U - U_d$. They are uncorrelated, hence independent, by virtue of their equal variance.

$$\langle[(U + U_d)(U - U_d)]\rangle_{av} = [U^2 - U_d^2] = 0 \tag{28}$$

Therefore all four random components of Σ and Δ are independent, from which the independence of $|\Sigma|$ and $|\Delta|$ follows.

The advantage of this approach is that equation (24), the probability that the amplitude of one complex gaussian (that is, a Ricean) exceeds another, is expressible in terms of the function[7]*

$$Q(A, B) \equiv \int_B^\infty \tau \exp\left(-\frac{A^2 + \tau^2}{2}\right) I_0(A\tau)\, d\tau. \tag{29}$$

One formulation is[8]

$$\Pr\{|\Sigma| < |\Delta|\} = \frac{1}{2}\left\{1 - Q\left[\frac{|C(\Sigma)|}{2\sigma}, \frac{|C(\Delta)|}{2\sigma}\right] + Q\left[\frac{|C(\Delta)|}{2\sigma}, \frac{|C(\Sigma)|}{2\sigma}\right]\right\}. \tag{30}$$

Evaluating the magnitudes of the means from equation (26),

$$\begin{aligned} |C(\Sigma)| &= 2\left[1 + 2b\cos\frac{\theta}{2}\cos\left(\phi + \frac{\theta}{2}\right) + b^2\cos^2\frac{\theta}{2}\right]^{\frac{1}{2}} \\ |C(\Delta)| &= 2b\sin\frac{\theta}{2}. \end{aligned} \tag{31}$$

We have thus far found Pe|"0" exactly, conditioned on the initial interference angle ϕ. The desired result is obtained by averaging equation (30) over ϕ. However, inserting equation (31) into equation (30) leaves an expression which offers little promise for analytically performing the integration. As an alternative, the integral is both approximated and bounded in what follows, thereby avoiding a machine integration.

The integration parameter ϕ appears in $|C(\Sigma)|$ but is not a factor of $|C(\Delta)|$. Then with the identification

$$\begin{aligned} B &\equiv |C(\Sigma)|/2\sigma \\ A &\equiv |C(\Delta)|/2\sigma \end{aligned} \tag{32}$$

* Q functions are tabulated, but not adequately in the argument ranges needed for these problems. Their usefulness lies in having good approximations which lead to easy machine calculations. See Ref. 8.

we are led to consider the behavior of the integrand

$$F(A, B) \equiv \tfrac{1}{2}[1 - Q(B, A) + Q(A, B)] \tag{33}$$

as a function of B only (fix A). Familiarity with $F(A, B)$ suggests that it is roughly exponential in $-B^2/2$.

To affirm this supposition we first show that

$$\frac{\partial F(A, B)}{\partial B} = -BK(A, B)F(A, B) \tag{34}$$

where $K(A, B)$ is bounded near 1:

$$1 \geqq K(A, B) \geqq 1 - \epsilon. \tag{35}$$

This approach is motivated by the recognition that if $F(A, B)$ could be approximated by an exponential in B^2, the integral of $F(A, B)$ over ϕ would be simple.

The derivation of equations (34) and (35) consists of elementary manipulations of the series and integral representations for $Q(A, B)$ which are given in Ref. 8. Henceforth, a prime designates partial differentiation with respect to B. For brevity, let

$$E \equiv \exp\left[-\frac{A^2 + B^2}{2}\right]. \tag{36}$$

Then using the series representations

$$Q(A, B) = E \sum_{m=0}^{\infty} \left(\frac{A}{B}\right)^m I_m(AB) \tag{37}$$

$$1 - Q(B, A) = E \sum_{m=1}^{\infty} \left(\frac{A}{B}\right)^m I_m(AB) \tag{38}$$

we see that

$$2F(A, B) = 2Q(A, B) - EI_0(A, B). \tag{39}$$

Then

$$2F'(A, B) = 2Q'(A, B) - EI_0'(AB) - E'I_0(AB) \tag{40}$$

$$= 2Q'(A, B) - EAI_1(AB) + BEI_0(AB). \tag{41}$$

Referring to the integral representation for the Q function we inspect

$$Q'(A, B) = -BEI_0(AB). \tag{42}$$

Therefore, from equations (42) and (41) we have

$$2F'(A, B) = -BE\left[I_0(AB) + \frac{A}{B} I_1(AB) \right]. \tag{43}$$

But from equations (37) and (38),

$$1 - Q(B, A) + Q(A, B) = E\left[I_0(AB) + 2 \sum_{m=1}^{\infty} \left(\frac{A}{B}\right)^m I_m(AB) \right]. \tag{44}$$

So that equation (34) is true for

$$K(A, B) = \frac{I_0(AB) + \left(\frac{A}{B}\right) I_1(AB)}{I_0(AB) + 2\left(\frac{A}{B}\right) I_1(AB) + 2 \sum_{m=2}^{\infty} \left(\frac{A}{B}\right)^m I_m(AB)}. \tag{45}$$

Since A, B, and the $I_m(x)$ are nonnegative the unity upper bound in equation (35) is obvious. For the lower bound, invert equation (45) and notice that

$$K(A, B)^{-1} \leqq 1 + 2 \sum_{m=1}^{\infty} \left(\frac{A}{B}\right)^m \frac{I_m(AB)}{I_0(AB)} \tag{46}$$

$$\leqq 1 + 2 \sum_{m=1}^{\infty} \left(\frac{A}{B}\right)^m \tag{47}$$

since the $I_m(x)$ decrease with the order m.

Referring to the definitions of equations (32) and (31) it can be shown that $A < B$ whenever $b < 1/(2)^{1/2}$, so that the summation converges for reasonable interference levels (CIR $>$ 3 dB). Then

$$K(A, B)^{-1} \leqq 1 + \frac{2A}{B - A} \tag{48}$$

so that

$$\epsilon \leqq \frac{2A}{B + A}. \tag{49}$$

In most cases $B \gg A$ so that $K(A, B)$ is near 1.

We now solve the linear, first order differential equation (34) to obtain

$$F(A, B) = \mathrm{Pe}_0 \exp\left[\int_{B_0}^{B} - \tau K(A, \tau)\, d\tau \right] \tag{50}$$

with initial data $F(A, B_0) = \mathrm{Pe}_0$. The above expression for $F(A, B)$

is exact. We now approximate the exp argument by approximating $K(A, B)$ with a constant K_0. Then we are able to carry out the integration in equation (50) to obtain

$$F(A, B) \approx \mathrm{Pe}_0 \exp\left[-\frac{K_0}{2}(B^2 - B_0^2)\right]. \tag{51}$$

We know the function at B_0, and we extrapolate to the function using an approximation of its derivative. Now the ϕ integration will range over some section of the exponentially varying $F(A, B)$ in equation (51) above. Because it is exponential, the significant contribution to the integral occurs over a relatively small range of B where $F(A, B)$ is near its maximum. This suggests that the initial data be specified at a maximum so that the approximation function is best in the important range of integration. Therefore we let

$$B_0 = B_{\min} \tag{52}$$

so that

$$\mathrm{Pe}_0 = F(A, B_0) \geqq F(A, B), \qquad 0 \leqq \phi \leqq 2\pi. \tag{53}$$

We notice from equation (31) that

$$B_{\min} = \frac{1}{\sigma}\left(1 - b\cos\frac{\theta}{2}\right) \tag{54}$$

and so

$$B^2 - B_0^2 = \frac{2b}{\sigma^2}\cos\frac{\theta}{2}\left[1 + \cos\left(\phi + \frac{\theta}{2}\right)\right]. \tag{55}$$

In addition, we slope-match at B_0, approximating $K(A, B)$ by $K_0 = K(A, B_0)$. From equation (45)

$$K(A, B_0) \approx \frac{1 + \left(\frac{A}{B_0}\right)\frac{I_1(AB_0)}{I_0(AB_0)}}{1 + 2\left(\frac{A}{B_0}\right)\frac{I_1(AB_0)}{I_0(AB_0)}}. \tag{56}$$

Inserting equation (55) into equation (51) and integrating,

$$\frac{1}{2\pi}\int_0^{2\pi} F(A, B)\, d\phi = F(A, B_0)\exp\left[-\frac{bK_0}{\sigma^2}\cos\frac{\theta}{2}\right] \cdot \int_0^{2\pi}\frac{d\phi}{2\pi}\exp\left[-\frac{bK_0}{\sigma^2}\cos\left(\phi + \frac{\theta}{2}\right)\right] \tag{57}$$

gives the desired result

$$\text{Pe} \mid \text{"0"} = \tfrac{1}{2}[1 - Q(B_0, A) + Q(A, B_0)] \cdot \exp\left[-\frac{bK_0}{\sigma^2}\cos\frac{\theta}{2}\right] I_0\left[\frac{bK_0}{\sigma^2}\cos\frac{\theta}{2}\right]. \tag{58}$$

Exact bounds are now easily obtained by bounding $K(A, B)$. With B_0 still chosen to be $B_{\min}$, clearly

$$\int_{B_0}^{B} -\tau K(A, \tau)\, d\tau \leqq \int_{B_0}^{B} -\tau K_{\min}\, d\tau = -\tfrac{1}{2}(B^2 - B_0^2)K_{\min} \tag{59}$$

where $K_{\min}$ is the minimum value of $K(A, B)$ in $[B_0, B]$. Similarly,

$$\int_{B_0}^{B} -\tau K(A, \tau)\, d\tau \geqq -\tfrac{1}{2}(B^2 - B_0^2)K_{\max}\,. \tag{60}$$

Therefore

$$F(A, B) \gtrless \text{Pe}_0 \exp\left[-\tfrac{1}{2}(B^2 - B_0^2)K_{\min}\right] \tag{61}$$

so that

$$\text{Pe} \mid \text{"0"}, \theta \lessgtr \text{Pe}_0 \exp\left[-K_{\min}\frac{b}{\sigma^2}\cos\frac{\theta}{2}\right] I_0\left[K_{\max}\frac{b}{\sigma^2}\cos\frac{\theta}{2}\right]. \tag{62}$$

The ratio of the bounds in equation (62) may be bounded in order to ascertain their closeness. We omit the cumbersome derivation, but state the result below.

$$\frac{\text{Upper Bound}}{\text{Lower Bound}} \leqq \left[\frac{\frac{1}{b} - \cos\frac{\theta}{2} + \sin\frac{\theta}{2}}{\frac{1}{b} - \cos\frac{\theta}{2} - \sin\frac{\theta}{2}}\right]^{0.65} \tag{63}$$

For CIR $\geqq$ 10 (15) dB, the ratio is less than 1.6 (1.25).

The symbol "1" is transmitted as two pulses of carrier 180° apart. Then correct reception results if $90° < |\delta| < 180°$. If an analysis quite similar to the preceding were carried out for this case, the resulting expressions would be identical with those above except that θ is replaced by $\pi - \theta$. It follows that

$$\text{Pe} \mid \text{"1"}, \theta = \text{Pe} \mid \text{"0"}, \pi - \theta. \tag{64}$$

We will elaborate on the relationship of Pe for the different data symbols in Section V.

Notice that Pe|"0" is symmetric in θ about 0 and π. The symmetry follows from the averaging of ϕ, and the insignificance of which of the two pulses occurs first as far as the detector is concerned.

Since the overall error probability

$$\text{Pe}\ (\theta) = \tfrac{1}{2}[\text{Pe} \mid \text{"1"}, \theta + \text{Pe} \mid \text{"0"}, \theta] \tag{65}$$

we use equation (64) to write

$$\text{Pe}\ (\theta) = \tfrac{1}{2}[\text{Pe} \mid \text{"0"}, \theta + \text{Pe} \mid \text{"0"}, \pi - \theta] \tag{66}$$

which is easily shown to be evenly symmetric about 0, π and $\pi/2$. We therefore need examine Pe only in the range $0 \leqq \theta \leqq 90°$.

Pe(θ) does vary considerably as seen in Fig. 7. Here the maximum and minimum values of Pe(θ), which happen to occur at $\pi/2$ and 0 respectively, are given for interesting combinations of interference and noise levels. To further illustrate the effects of interference, we present curves of decibel degradation versus θ in Fig. 8. Degradation is defined as the dB reduction in carrier-to-noise ratio which is allowed to maintain the same Pe after removing the interference.

Finally, consider an angle modulation impressed on the interference. This situation may be viewed simply as a time varying θ. Then one may average the Pe(θ) results given here over the variations of θ. If this is undesirable, the curves of Fig. 7 are certainly bounds on Pe averaged over the θ variation.

V. DIFFERENTIAL DETECTION—QUATERNARY

We now examine the effect of a single interference on a differentially detected quaternary (4-phase) signal. We will refer to the four symbols as "0", "1", "2", and "3", where the associated baud to baud phase shifts are 0, $\pi/2$, π, and $-\pi/2$ respectively. As before, the phase discriminator examines the two composite phasors, Z and Z_d, and reports their angle difference δ. The ordering of the bauds is important, since we must distinguish between $\delta = \pi/2$ and $\delta = -\pi/2$. The "0" symbol possesses the same symmetry as in the binary case; we therefore base the analysis on Pe|"0". Then in an analogous fashion we relate Pe|"0" to the probability of error for the other symbols.

In the binary case the receiver tested for the sign of Re $[ZZ_d^*]$. This test was transformable to a test between the amplitudes of two Ricean random variables, one which enjoys a closed form solution. Unfortunately, in the present case the test, which is for a "0"

$$\text{Pe} \mid \text{“0”} = \Pr\left\{\cos\,\delta = \frac{\text{Re}\,[ZZ_d^*]}{\mid Z \mid \mid Z_d \mid} \leqq \frac{(2)^{\frac{1}{2}}}{2}\right\}$$

is not known to be transformable to one which has a closed solution. On the other hand, we offer a very straightforward analysis which is exact and amenable to machine computation.

Figure 9 is a “double exposure” of the signal, noise, and interference components for a “0”. The two carrier pulses are, of course, coincident and lie along the reference axis. We recall that the angle of

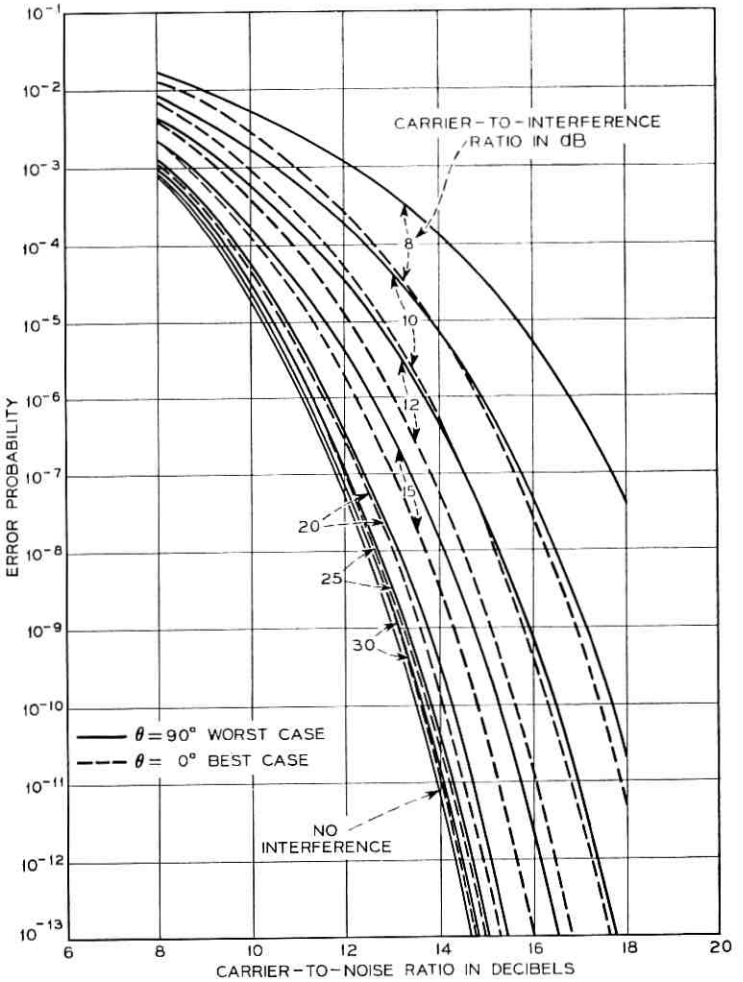

Fig. 7 — Binary Pe versus CNR. Differential detection.

the interference at t_0 is ϕ, and at $t_0 + T$ is $\phi + \theta$. We will again average over ϕ, leaving θ as a parameter.

At time t_0 the resultant of signal and interference, shown by a dashed line, has length W and angle ξ which by inspection are

$$W = (1 + b^2 + 2b \cos \phi)^{\frac{1}{2}} \tag{67}$$

$$\xi = \tan^{-1}\left[\frac{b \sin \phi}{1 + b \cos \phi}\right]. \tag{68}$$

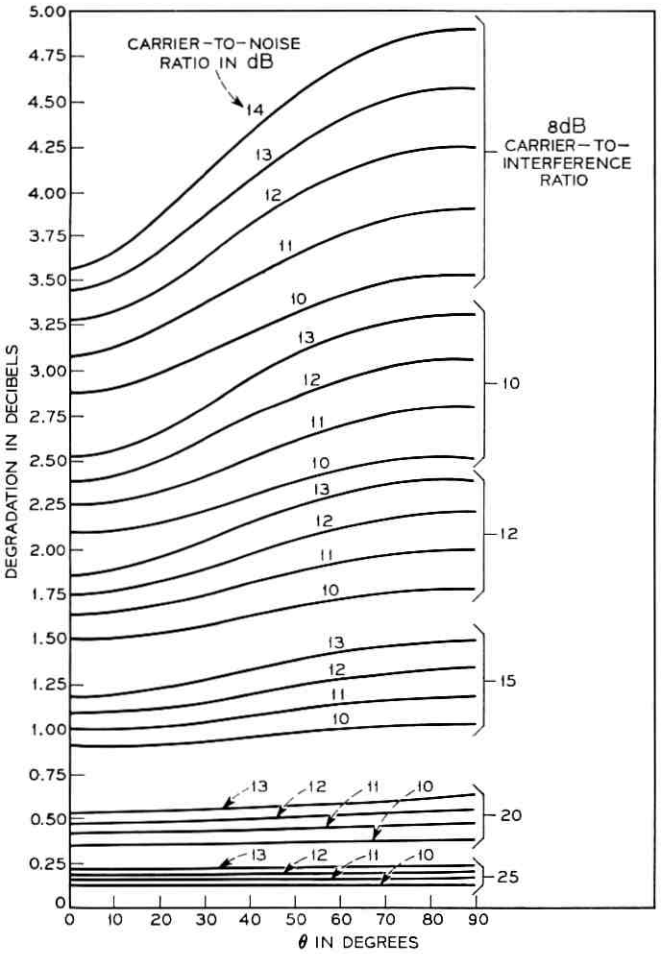

Fig. 8 — Degradation in CNR caused by interference versus θ for binary differential detection.

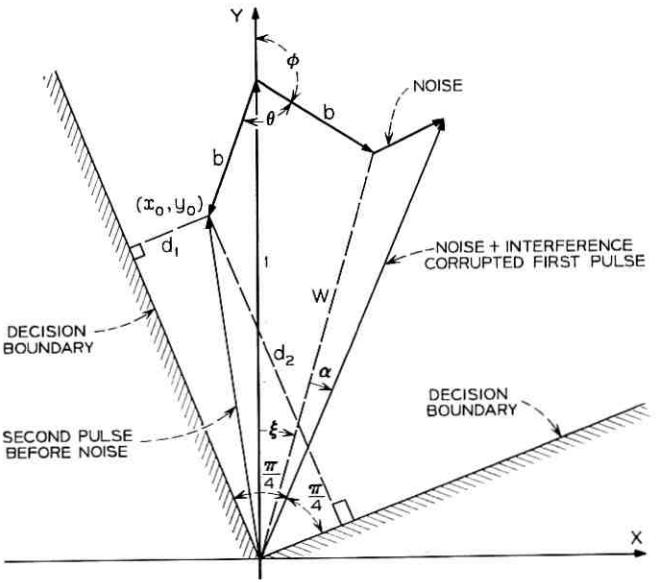

Fig. 9 — Phasor diagram for quaternary differential detection.

To the resultant of signal and interference adds a Rayleigh amplitude, uniform angle noise phasor. The resultant W is perturbed both in amplitude and angle by the noise. The resulting amplitude is unimportant, but the angle, $\xi + \alpha$, establishes the reference for detecting the second pulse. The probability density function of α is well known to be

$$f_\alpha(\alpha) = \frac{1}{2\pi} \exp(-\Psi)\{1 + \Psi^{\frac{1}{2}}\pi \cos\alpha \cdot \exp(\Psi \cos^2\alpha)[1 + \operatorname{erf}(\Psi^{\frac{1}{2}} \cos\alpha)]\} \quad (69)$$

where

$$\operatorname{erf}(x) \equiv \frac{2}{\pi^{\frac{1}{2}}} \int_0^x \exp(-u^2)\, du \quad (70)$$

is the usual error function integral and

$$\Psi = \frac{W^2}{2\sigma^2} \quad (71)$$

is the power ratio (signal plus interference)/noise.

At $t_0 + T$ the second pulse is examined. It is disturbed by interference to the point (x_0, y_0),

$$\begin{aligned} x_0 &= b \sin(\phi + \theta) \\ y_0 &= 1 + b \cos(\phi + \theta). \end{aligned} \tag{72}$$

The decoding region is a quarter plane bisected by the direction of the first pulse as shown by the orthogonal decision boundaries. The probability of correct reception is simply the probability that a random noise phasor originating at (x_0, y_0) will terminate inside this quadrant. Using the independent orthogonal phasor representation for noise, and choosing the components to lie alongside the perpendicular distances d_1 and d_2 from (x_0, y_0) to the boundaries, we write directly

$$1 - \text{Pe} \mid \text{“0”}, \phi, \alpha = \frac{1}{2}\left[1 + \operatorname{erf}\left(\frac{d_1}{2^{\frac{1}{2}}\sigma}\right)\right]\frac{1}{2}\left[1 + \operatorname{erf}\left(\frac{d_2}{2^{\frac{1}{2}}\sigma}\right)\right]. \tag{73}$$

Now using erf + erfc = 1 we have

$$\begin{aligned} \text{Pe} \mid \text{“0”}, \phi, \alpha = {} & \tfrac{1}{2}\operatorname{erfc}\left(\frac{d_1}{2^{\frac{1}{2}}\sigma}\right) \\ & + \tfrac{1}{2}\operatorname{erfc}\left(\frac{d_2}{2^{\frac{1}{2}}\sigma}\right) - \tfrac{1}{4}\operatorname{erfc}\left(\frac{d_1}{2^{\frac{1}{2}}\sigma}\right)\operatorname{erfc}\left(\frac{d_2}{2^{\frac{1}{2}}\sigma}\right). \end{aligned} \tag{74}$$

The distances d_1 and d_2 may be verified to be

$$\begin{aligned} d_1 &= -y_0 \sin\left(\alpha + \xi - \frac{\pi}{4}\right) + x_0 \cos\left(\alpha + \xi - \frac{\pi}{4}\right) \\ d_2 &= y_0 \sin\left(\alpha + \xi + \frac{\pi}{4}\right) - x_0 \cos\left(\alpha + \xi + \frac{\pi}{4}\right) \end{aligned} \tag{75}$$

such that they take the positive sign if (x_0, y_0) lies on the correct reception side of the respective boundary.

Eliminating the ϕ and α dependency results in a finite limits double integral

$$\text{Pe} \mid \text{“0”} = \int_0^{2\pi} \frac{d\phi}{2\pi} \int_{-\pi}^{\pi} f_\alpha(\alpha)\, \text{Pe} \mid \text{“0”}, \phi, \alpha \, d\alpha \tag{76}$$

which was machine evaluated.

The relationship between Pe | “0” and the other symbols is easily demonstrated graphically. Figure 10 is a phasor diagram illustrating a typical noise and interference corrupted first pulse, and the four

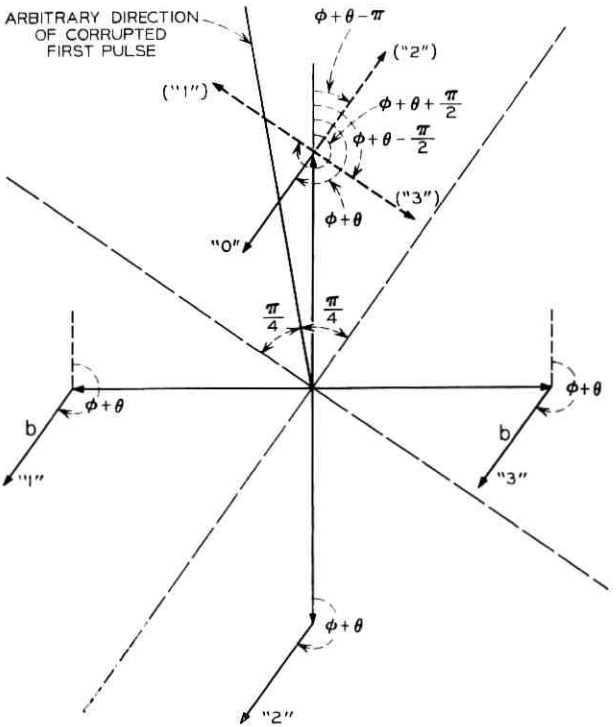

Fig. 10 — The relationship of $Pe|\theta$ for the individual symbols.

possible positions of the pre-interference second pulse. Decoding quadrants determined by the angle of the first pulse are shown by dashed lines. Adding to each of the possible second pulse carrier phasors, which correspond to the four data symbols, is an interference phasor having some angle $\phi + \theta$.

If a "0" had been sent, the probability of error conditioned on the present geometry (that is, the values of ϕ, α, and θ) is the probability that a noise phasor originating at the tip of the solid interference phasor (labeled "0") terminates outside the "0" quadrant. This probability is a function of σ and the distances from the tip of the interference phasor to the boundaries.

Now assume that a "3" had been sent instead. The associated second carrier pulse is shifted clockwise by $\pi/2$, but the interference phasor at $t_0 + T$ is still at $\phi + \theta$ relative to the diagram reference. Returning to the "0" quadrant, consider an interference phasor hav-

ing the angle $\phi + \theta - \pi/2$, shown by the dashed line labelled "3". It is apparent (and trivial to show) that the distances of the dashed "3" phasor to the "0" quadrant boundaries are identical with the distances of the actual "3" interference phasor to the "3" quadrant boundaries. We conclude, therefore, that

$$\text{Pe} \mid \text{"3"}, \phi, \alpha, \theta = \text{Pe} \mid \text{"0"}, \phi, \alpha, \theta - \frac{\pi}{2}. \tag{77}$$

Now integrating both sides of the equality over all ϕ, α yields the desired relationship

$$\text{Pe} \mid \text{"3"}, \theta = \text{Pe} \mid \text{"0"}, \theta - \frac{\pi}{2}. \tag{78}$$

Similarly we have

$$\text{Pe} \mid \text{"2"}, \theta = \text{Pe} \mid \text{"0"}, \theta - \pi \tag{79}$$

$$\text{Pe} \mid \text{"1"}, \theta = \text{Pe} \mid \text{"0"}, \theta + \frac{\pi}{2} \tag{80}$$

so that the average symbol error probability becomes

$$\text{Pe}(\theta) = \frac{1}{4}\left[\text{Pe} \mid \text{"0"}, \theta + \text{Pe} \mid \text{"0"}, \theta - \frac{\pi}{2} + \text{Pe} \mid \text{"0"}, \theta + \frac{\pi}{2} + \text{Pe} \mid \text{"0"}, \theta - \pi\right] \tag{81}$$

which is solely in terms of Pe | "0".

Notice that equation (79) is exactly the result obtained for a "1" in binary. This is not surprising, since a "2" constitutes a 180° phase shift of the second pulse. In fact, the arguments relating to Fig. 10 may be generalized for an M-phase d-psk signal with a "J" symbol phase shift of $(2\pi J)/M$, to be

$$\text{Pe} \mid \text{"}J\text{"}, \theta = \text{Pe} \mid \text{"0"}, \theta + \frac{2\pi J}{M}. \tag{82}$$

Averaging over the symbols in equation (81) produces a $\text{Pe}(\theta)$ which is evenly symmetric about 0, $\pi/4$, $\pi/2$, . . . ; points half as far apart as in binary. Also, while Pe|"0" still varies over a considerable range, when four symbols are averaged instead of two the range of $\text{Pe}(\theta)$ is significantly decreased. This is evidenced by the numerical results plotted in Fig. 11. Again, the solid and dashed lines represent

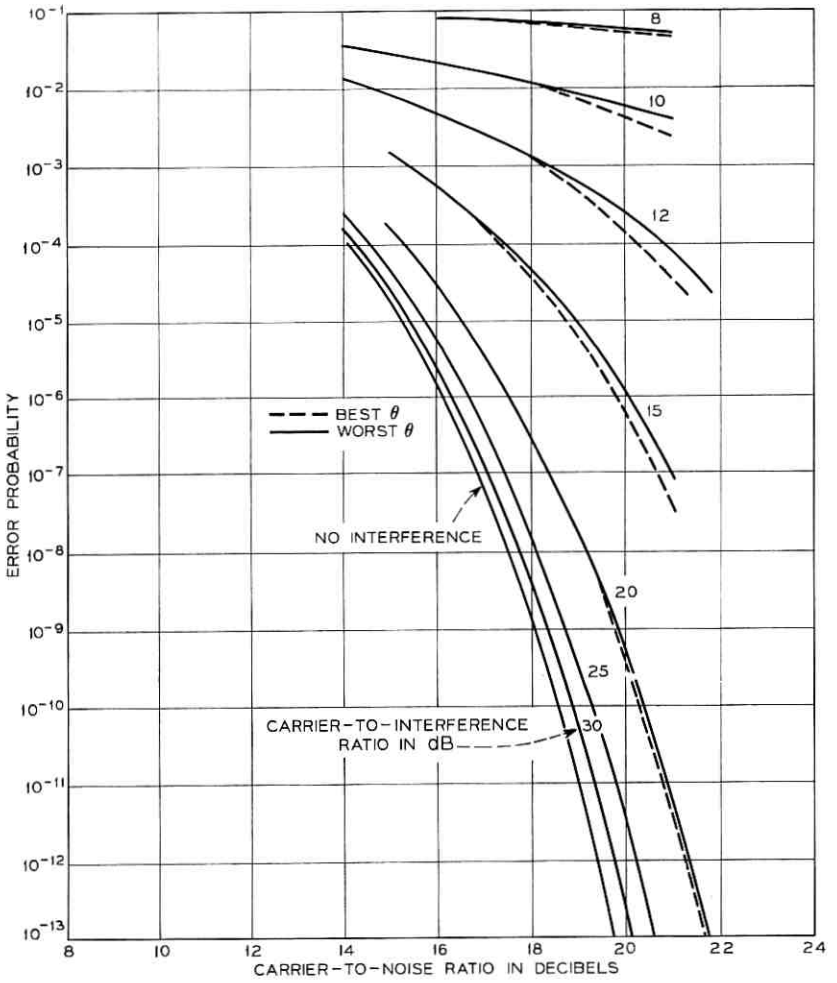

Fig. 11 — Quaternary symbol Pe versus CNR. Differential detection.

maximum and minimum values of the symbol Pe. The values of θ which correspond to the maximum and minimum are not the same for all noise and interference level combinations. However, $\mathrm{Pe}(\theta)$ is generally lowest near 0, $\pi/2$, π . . . and highest near $\pi/4$, $3\pi/4$, . . . , and so on.

Since $\mathrm{Pe}(\theta)$ fluctuates less severely for quaternary, it is more meaningful to average over θ. This was done, and the average used as a base for computing the degradation curves of Fig. 12.

VI. DIFFERENTIAL DETECTION — M > 4

For large M systems, for example $M \geqq 8$, we compute the average error probability

$$\mathrm{Pe} = \frac{M}{\pi} \int_0^{\pi/M} \mathrm{Pe}\,(\theta)\, d\theta \tag{83}$$

assuming now that θ is a uniformly distributed random variable. Because of the rapidly diminishing θ dependency noted in Section V, the average over θ is a useful measure of error performance. The choice of a uniform distribution for θ allows an approach which relies on the previously obtained $f_A(\alpha)$ data, rather than finding $\mathrm{Pe}(\theta)$ and then integrating.

Let the interference phase angles at t_0 and $t_0 + T$ be random variables Φ and $\Phi + \Theta$, respectively. We first note that the sum $\Phi + \Theta$ modulo 2π is uniformly distributed since Φ (or Θ) is uniform. Hence both interference angles, Φ and $\Phi + \Theta$, are uniformly distributed. Furthermore, since for any $\Phi = \phi$ the sum $\phi + \Theta$ (modulo 2π) is uniform, we conclude that Φ and $\Phi + \Theta$ are independent. The adjacent interference angles then are independent; and consequently the phase angle, A, of $s + n + i$ is independent from sample to sample.

We therefore obtain the probability density function of the differ-

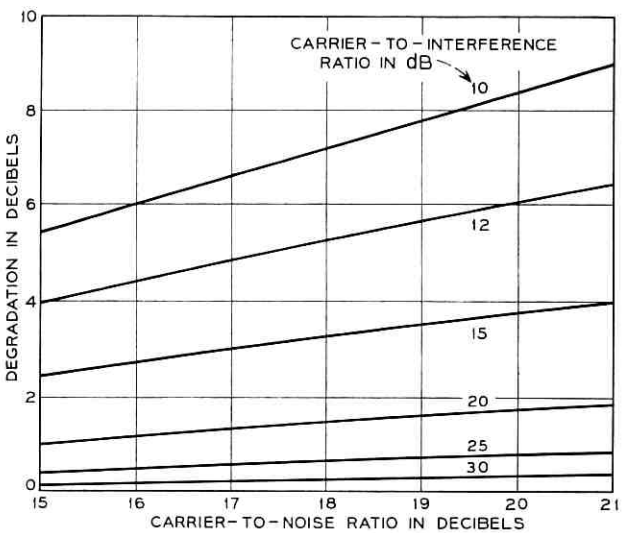

Fig. 12 — Degradation in CNR caused by interference for quaternary differential detection.

ence angle $\delta = A(t_0 + T) - A(t_0)$ as the modulo 2π convolution of $f_A(\alpha)$ with itself. Then the integral of the probability density function of δ over $|\delta| > (\pi/M)$ yields Pe. Numerical results were obtained in this fashion for $M = 4$, 8, and 16. The $M = 4$ data was in excellent agreement with Fig. 11. Pe for $M = 8$ and $M = 16$ is displayed in Fig. 13. When $b > \sin(\pi/2M)$ the interference alone can exceed the thresholds and cause errors. This is seen as a Pe floor for low CIR

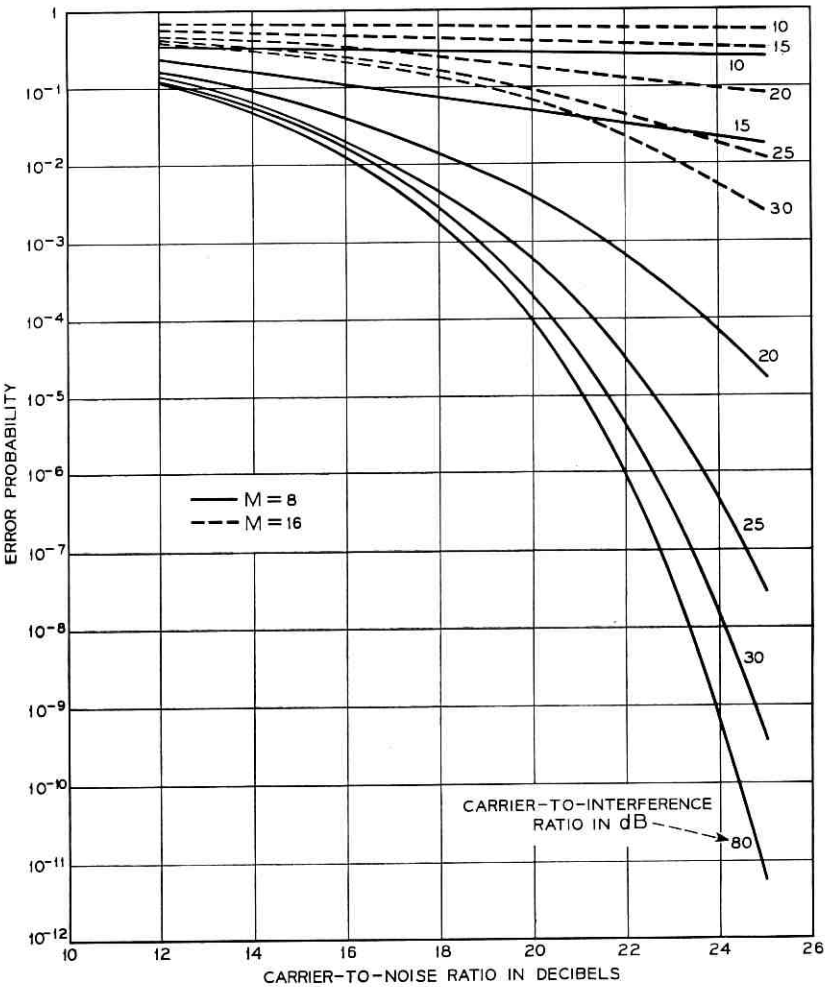

Fig. 13 — Symbol Pe versus CNR for 8 and 16 phase differential detection.

values; increasing CNR does not cause Pe to tend toward zero.

Finally, we remark that the averaging of Pe over the M symbols was implicitly done in the θ averaging. We see from equation (82) that all symbols have equal error probability when θ is uniformly distributed.

VII. SUMMARY AND CONCLUSIONS

We have evaluated the symbol error probabilities for both coherent and differential detection of low M psk signals in the presence of interference. The effect of the interference is readily observed in the curves of Figs. 3–5, 7, 11, and 13. Although the increase in Pe resulting from interference is large, it is considerably less than if the interference were replaced by gaussian noise of the same power, especially at low Pe levels.

Comparing Figs. 3, 4, and 5, we see that vulnerability increases with M. That is, at a given CNR, the Pe is raised least for $M = 2$ and greatest for $M = 4$ by the addition of interference. For example, without interference the error performance of $M = 2$ versus $M = 4$ differs by 3 dB. When a -10 dB interferer is added, it differs by approximately 5 dB, indicating a 2 dB CNR penalty for equal *Pe* values.

Drawing comparisons between coherent and differential detection reveals that differential detection clearly suffers more degradation. Binary differential, however, performs about as well with interference at optimum θ values as does binary coherent. This is in contrast with the performance disparity between the two $M = 4$ systems. With a -10 dB interference, differential detection suffers a degradation ranging from 5½ to 8 dB; coherent detection is degraded only 4 to 4½ dB for the same CNR range.

We use degradation rather than the raw Pe versus CNR curves to make the above comparisons because of the inherent difference in performance between differential and coherent psk for noise alone. That is, the degradation comparisons automatically reconcile any disparities in the noise-only performances of the various systems.

REFERENCES

1. Davenport, W. B. and Root, W. L., *Random Signals and Noise,* New York: McGraw-Hill, 1958, pp. 158–159.
2. Papoulis, A., *Probability, Random Variables and Stochastic Processes,* New York: McGraw-Hill, 1965, pp. 182–183.
3. Scire, F. J., "A Probability Density Function Theorem for the Modulo y Values of the Sum of Two Statistically Independent Processes," Proc. IEEE, *56,* No. 2 (February 1968), pp. 204–205.

4. Rice, S. O., "Statistical Properties of a Sine Wave Plus Random Noise," B.S.T.J., *27*, No. 1 (January 1948), pp. 109–114.
5. Arthurs, E. and Dym, H., "On the Optimum Detection of Digital Signals in the Presence of White Gaussian Noise—a Geometric Interpretation and a Study of Three Basic Data Transmission Systems," IRE Trans. on Communication Systems, *CS-10*, No. 4 (December 1962), pp. 336–372.
6. Stein, S., "Unified Analysis of Certain Coherent and Noncoherent Binary Communications Systems," IEEE Trans. on Information Theory, *IT-10*, No. 1 (January 1964), pp. 43–51.
7. Marcum, J. I., "Tables of the Q Function," Rand Corporation Memorandum RM-399 (January 1950).
8. Schwartz, M., Bennett, W. R., and Stein, S., *Communication Systems and Techniques*, New York: McGraw-Hill, 1966, Appendix A.

New Time Division Switch Units for No. 101 ESS

By T. E. BROWNE, D. J. WADSWORTH, and R. K. YORK

(Manuscript received September 11, 1968)

The No. 101 ESS provides centrex service utilizing stored program common control located in the central office and time-division switching units located on the customer's premises. The 2A and 3A switch units serve a wide range of customers (up to 820 lines) using a PAM time-division switching network with lossless through switching, high return loss, and high crosstalk attenuation. System operation, time-division transmission, logic and control, maintenance features, and physical characteristics of the switch units are described.

I. INTRODUCTION

The initial development of the No. 101 Electronic Switching System to provide commercial private branch exchange (PBX) service was completed in November 1963.[1] This system utilizes a stored program common control located in the central office and time-division switching units located on customers premises, connected to the common control by data links and trunks. This initial system design included a time-division switch unit, which served customers having a maximum of 200 extensions and 40 trunks.[2] Although this line capacity meets the requirements of a large percentage of the PBX customers of the Bell System, there are a significant number of customers who require service for more than 200 lines. These customers may now be served by No. 101 ESS through the use of the 2A (364 lines), 3A (820 lines), and 4A[3] (800 to 4000* lines) switch units in concert with the control unit. This paper describes the 2A and 3A switch units; the 4A is described in a separate article in this issue.

* The 4A switch unit capacity is 2000 lines. Expansion to a 4000 line capacity is under development.

II. SYSTEM DESCRIPTION OF NO. 101 ESS

2.1 *System Plan*

The control unit, by means of a stored program, provides the logic and memory required for call processing and for system maintenance. The switch units, by means of wired logic and memory, provide the switching paths between subscribers, supervisory scanning of subscriber lines, and ringing and signaling sources for alerting subscribers and attendants. In addition, maintenance circuits in the switch units, in conjunction with a maintenance program operating in the control unit, provide for rapid detection of equipment malfunction. Component and circuit redundancy is included in both the control unit and the switch units to minimize service degradations which would otherwise result from equipment failures.

Information transfer between the control unit and switch units is accomplished by a voiceband data facility and a set of trunks for carrying dialed digits. Each switch unit has its own data channels connecting it to the control unit.

In addition to controlling the switch units connected to it, the control unit, by means of direct association with a central office switching system, provides an interface between No. 101 ESS switch units and the Bell System switching network. The No. 101 ESS provides the entire range of centrex services and memory features available to PBX customers.

2.2 *Basic System Operation*

In the interest of economy of program storage, each switch unit served by a control unit is handled in the same way. Thus, for call processing and maintenance, one basic program is contained in the control unit. Administrative variables provide information needed for processing calls according to the requirements of each customer. The switch units being served by the same control units are independent of each other and therefore, from the point of view of switch unit operation, the system may be accurately discussed in terms of a single switch unit operating with a control unit.

Connections to lines and trunks are provided on a time-division basis at the switch units. The identities of the parties being connected are held in successive words of a sequential memory. The period of the memory operation establishes the period of the sampling process. In the 2A switch unit, a maximum of 60 simultaneous con-

nections can be established. The 3A switch unit may provide a maximum of 240 simultaneous connections.

Figure 1 is a block diagram of the switch unit. Time-division connecting paths are shown as heavy lines. To illustrate, let us describe a typical intra-PBX call. When the calling party goes off-hook, the supervisory state of the associated line circuit is interrogated by the scanner and registered in the scanner logic via the scanner bus. The last-look state, or supervisory state when last interrogated, is extracted from memory and compared with the present state. Noting a change in state, the scanner ceases to interrogate other circuits and formulates a message which the switch control sends to the control unit. The control unit recognizes this message as an origination service request and sends a message to the switch unit to establish a dial tone connection. A *Touch-Tone*® telephone subset will be assumed as the calling party's instrument. The *Touch-Tone* dialing signals by the station user are transmitted through the switch unit on a time-division basis, then by conventional transmission to the control unit.

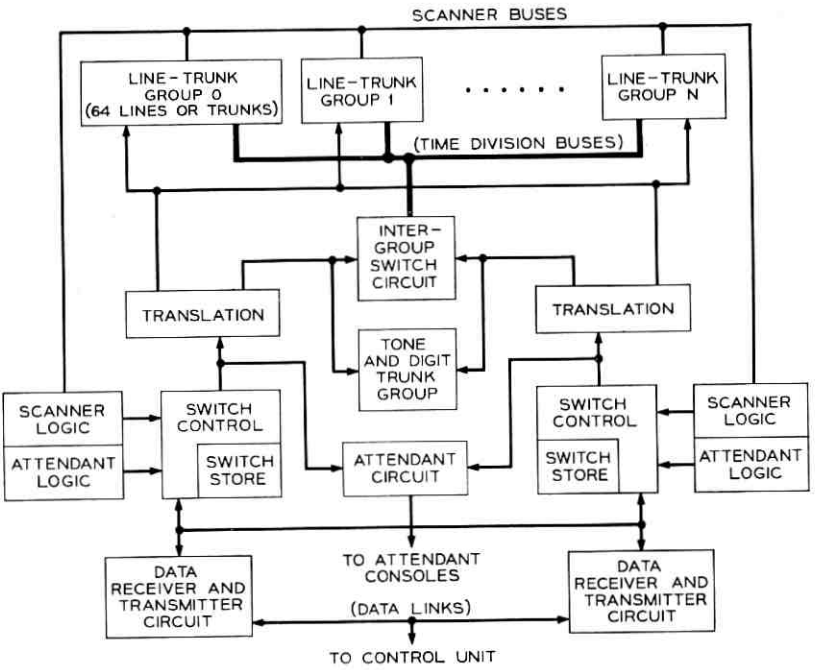

Fig. 1 — 2A and 3A switch unit block diagram.

At the completion of dialing, the control unit establishes a ringing connection in the switch unit between the calling and called parties. When the called party answers, the change of state is noted and the off-hook message is sent to the control unit. The control unit then sends a message to change the ringing connection to a normal talking connection. When the call is terminated, the on-hook state of either party is detected and the message is sent to the control unit. A disconnect message is then sent to the switch unit, removing the connection.

In the Section III, we describe in detail the manner in which these various functions are implemented in the 2A and 3A switch units. The basic system design is the same for both switch units, but differences do exist in the particular realizations of the design. We describe some of these in Sections IV and V. As a direct result of the similarities in the switch units, a high degree of component and circuit package compatibility between the two has been achieved, leading to long-term savings in manufacturing costs and ease of maintenance. In Section VI we discuss the equipment aspects of the systems.

III. ORGANIZATION AND DESCRIPTION

3.1 *Time-Division Transmission*

The essence of time-division transmission is that properly spaced periodic samples of a band limited information signal (for example, speech) completely define the signal. Sampling switches and suitable filters establish a bilateral transmission path as shown in Fig. 2. A connection is established by synchronously operating the selected switches for a time τ every T seconds. During τ, charges on the low pass filter capacitors C are efficiently interchanged by resonant transfer.[4] The high frequency sampling components are suppressed by the low pass filters resulting in a bilateral transmission of baseband signals.

By making τ a small fraction of T, a common bus can be shared by many connections. It is necessary to provide a "guard" interval between adjacent connection time intervals. A connection or "talking" interval and a "guard" interval is termed a time slot. During the guard interval, residual energies left on the bus at the end of the talking interval are dissipated by a resistance in series with a bus clamp to ground. In the 2A and 3A switch units, the timing values

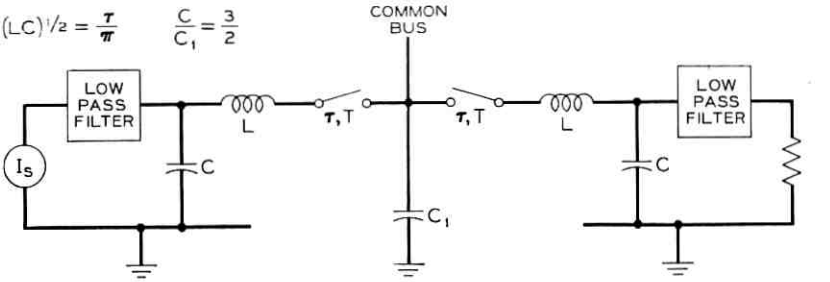

Fig. 2 — Time-division transmission path.

are 0.8 μsec for talking interval (τ), 0.432 μsec for the guard interval, and 85 μsec for the sampling period (T).

The low pass filter and filter response are shown in Fig. 3. The filter design provided by Thomas is modified to include an antiresonant circuit at the sampling frequency.[6] Without this, the normal filter attenuation of about 40 dB will not adequately suppress signals at the sampling frequency. With it, greater than 42 dB of suppression of the first lower sideband is realized. The 8.1 KHz attenuation peak is a result of the M-derived terminating section ($M = 0.7$), and is required to suppress the half sampling rate frequency components present during a ringing connection.

Negative impedance converters are used in two areas of the transmission network. A common negative impedance converter is connected to each time division bus to reduce the shunt losses from other transmission components. Improved system return loss results and a small amount (0.2 dB) of insertion gain is realized. In order to pro-

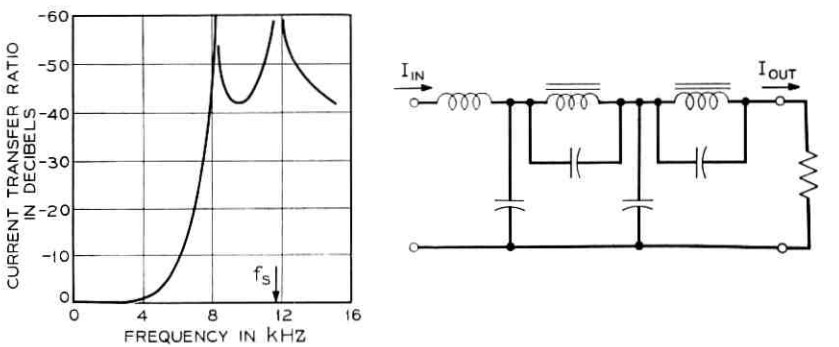

Fig. 3 — Low-pass filter and response.

vide a lossless through-switched connection (trunk to trunk), a switchable negative impedance converter gain circuit is provided with each tie trunk circuit (see Fig. 4). As required, control signals switch in the trunk negative impedance converter to reduce the 2.0 dB system insertion loss to near zero. Table I lists the typical transmission performance characteristics of the switch units.

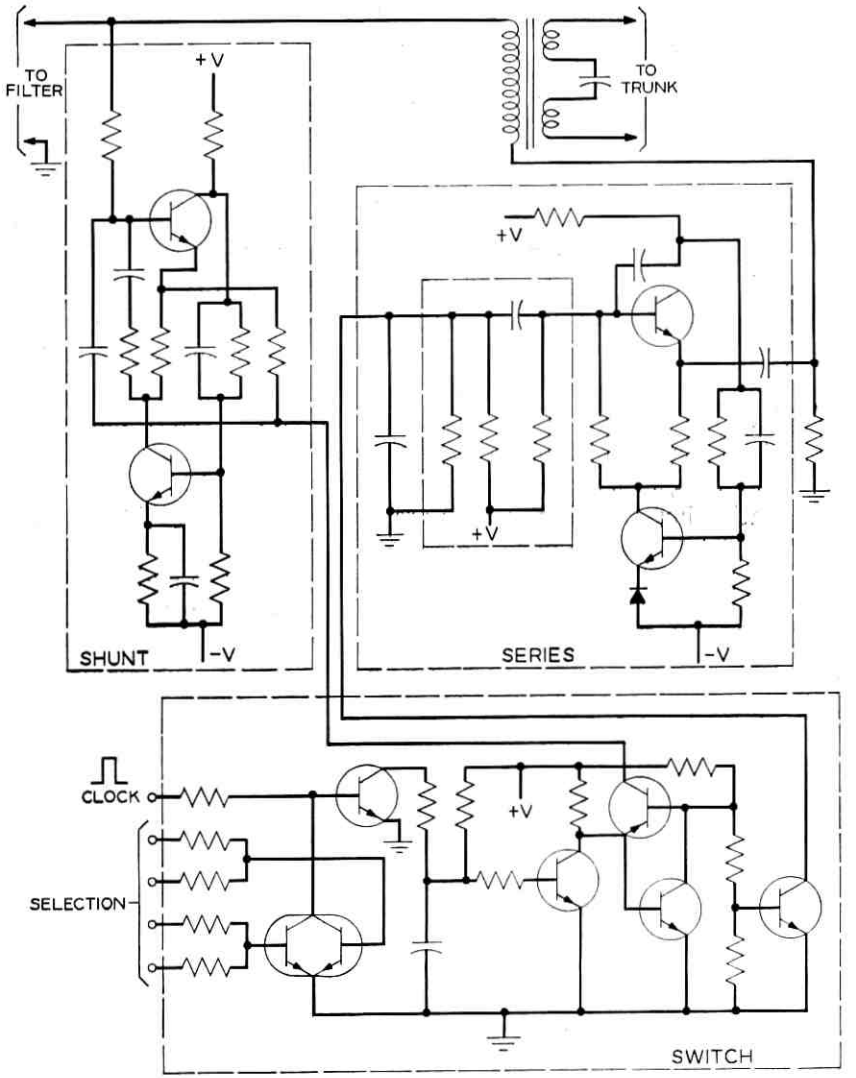

Fig. 4 — Switched-gain negative resistance amplifier circuit.

TABLE I—2A AND 3A SWITCH UNIT TYPICAL TRANSMISSION PERFORMANCE

Insertion loss (dB)	
Trunk to trunk	0.35
Trunk to line	2.0
Line to line	2.2
Echo return loss (dB)	30
Crosstalk (dB)	−90
Noise (dBrnc)	18
Signal overload	
6 dBm	no compression
9 dBm	1.8 dB compression
12 dBm	2.6 dB compression

In the 2A and 3A switch units, the time slots provide talking connections and data functions, such as scanning of the supervisory states of line, trunk, attendant, and maintenance circuits; sending and receiving data messages; and lighting the attendant console lamps.

3.2 *Line and Trunk Arrangement*

In a time-division switching system, a few common buses are being time shared by a relatively large number of lines and trunks. Therefore, the design must take into account the possibility of at least single component failures, and try to eliminate the possibility of the loss of a bus resulting from a single line or trunk component failure. Also, since the actual number of lines and trunks served by a switch unit in a given installation is variable, the parasitic loading of the buses is also variable. This loading and variations in it have a significant effect on the transmission performance of a time division system.

In the 2A and 3A switch units, control of system failure modes and control of parasitic bus loading is achieved by segregating the lines and trunks into groups of 64 as shown in Fig. 1. In each group, lines and trunks occupy positions in an 8-by-8 matrix; this provides for efficient use of access circuitry which is duplicated to preclude a total group failure. To further control parasitics, there are two time-division buses for each group, each serving 32 lines or trunks. A duplicated intergroup switch provides time-division connections between these group buses, such that during any time slot, any group can be connected to any other group. Since there are no restrictions on the time slots in which lines or trunks may be selected, any line or trunk may be connected to any other line or trunk during any time slot.

An additional benefit of line and trunk groups is that a switch

unit may be installed with fewer groups equipped than will be ultimately required by the customer. As his needs grow, additional lines and trunks may be plugged in without disturbing the transmission performance of the system.

3.3 *Logic and Control*

3.3.1 *Store Control*

The switch store operation is cyclic in nature, providing the rate of sampling for talking connections and the rate of scanning. During talking time slots and some data time slots, information is read and written back into the memory in the same form. In the execution of some of the system control functions, the information read from the store is written back in the same word, but shifted one bit position. Repetitive operation in this mode involving a particular word of storage makes that word a shift register. This technique is used during the data time slots for scanning, sending messages to the control unit, and processing messages received from the control unit.

3.3.2 *Scanning*

The first two data time slots are used for scanning (see Fig. 5): the first for interrogating the scan points to determine their present state and the second for reading their past state from memory. Since

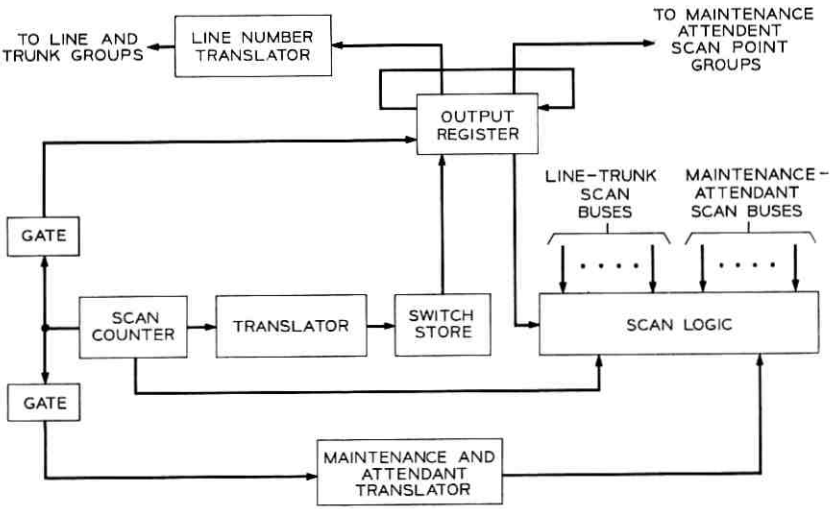

Fig. 5 — Scanner block diagram.

no talking signals are sampled during these time slots, the same line number translation circuitry is used to interrogate scan points as is used to operate time division switches. A separate translator provides access to the maintenance and attendant scan points.

3.3.2.1 *Line and Trunk Scanning*

The scan counter generates the address of each line and trunk circuit sequentially. To interrogate a line or trunk scan point, the address in the scan counter is gated into the output register bits normally used for the called party address in a talking time slot. As shown in Fig. 5, these bits are then translated by the line number translator to select the line or trunk circuits. The supervisory state is interrogated by pulsing the time-division switch driver, which in turn drives the scan point circuitry. The time-division switch current is inhibited during this scan time slot to eliminate false sampling of the talking signal. If the line is off-hook, a pulse is generated by the supervisory circuit and gated to a scanner logic flip-flop via the scan bus. During the second scan time slot, the past state of the scan point is obtained from the switch store and gated to the scanner logic where it is compared with the present state bit previously stored. If no difference is recognized, scanning continues by incrementing the scan counter and repeating the sequence. If a difference between present and past states is detected and does persist for a time interval sufficient to discriminate against line noise, the scan point change is assumed valid; a message is formulated in the switch store and the past state bit is updated. The switch control then sends the message to the control unit.

3.3.2.2 *Maintenance and Attendant Scanning*

Requests for service by an attendant or operation of maintenance circuits cause their assigned scan point circuits to change state. Scanning of these circuits differs from line and trunk scanning; for each scan point, a binary address is assigned, which also identifies a last-look bit in the switch store. The scan address is gated to a translator that selects a group of 16 scan points. The particular scan point in the group is interrogated by a ring counter consisting of a single "one" circulating in a word of the switch store. The position of the one is determined by the scan counter. The last-look bit is extracted from memory in the same manner as the line and trunk scanning. When a change in state occurs, a message is formulated for transmission to the control unit.

3.3.3 *Message Transmission*

When a message is to be sent to the control unit, the scanner is stopped and the message sending circuitry is activated (see Fig. 6). The word in the switch store which was used to contain the address of the interrogated scan point is also used to outpulse the data message. This message contains a start bit, the address of the circuit interrogated, a present state bit, and a parity bit. Each bit duration is timed by a crystal oscillator and a counter in the data receiver. The message is gated one bit at a time to the data transmitter. After each bit, the contents of the message word and counter word are shifted one position and, if the bit was a one, the parity counter is advanced. After 13 bits have been transmitted, the position of the counter bit is recognized, and the proper parity bit is transmitted. The scanner is then signaled to begin its normal scanning sequence.

3.3.4 *Incoming Message Control*

Communication between the control unit and the switch unit is accomplished with a voice-frequency signaling system using serially-generated frequency-shift signals. The data transmiter and receiver circuit provide the conversion into dc levels as well as the timing signals for bit identification. As each bit is received, it is gated into bit

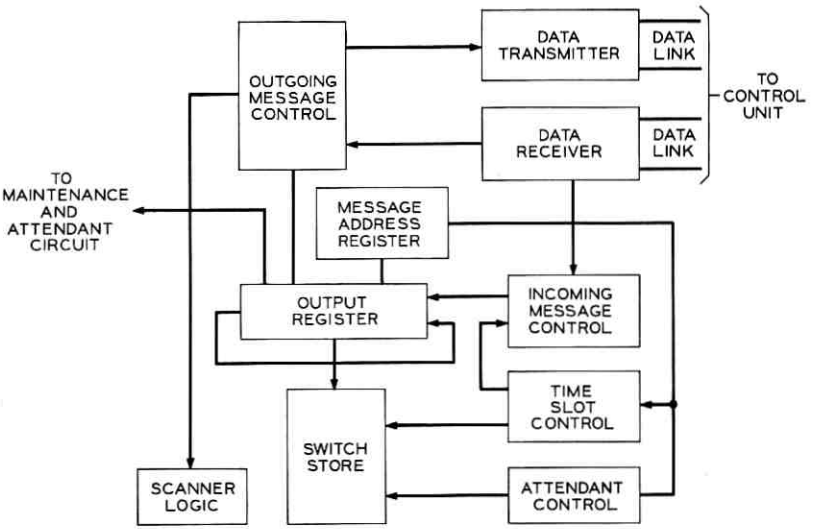

Fig. 6 — Switch unit message control.

1 of both stores during the message-loading time slot. On the next store cycle, this bit is shifted one position, thereby preparing bit 1 for the next message bit to be received. In this way, the message is loaded into both stores as it is received.

3.3.5 *Connection Message Loading*

Since the incoming message length exceeds the store word length, the loading sequence uses two store words. The first word is sequentially loaded with a start code and the message address. When the start code is recognized, the message address is gated to the message address register for interpretation, and succeeding message bits are loaded into the second word, which was reserved for this purpose. When the correct number of these bits have been loaded, the remaining bits of the message are then loaded into the remainder of the first word.

If parity is incorrect, the message is discarded and a parity-failure message is sent to the control unit. If parity is correct, relocation of the information in the second word is begun by reading this word out of the store into the output register. Information in the first data word is cleared. The contents of the message address register are gated to the store address circuitry to cause the corresponding word to be the next one read from the store. This new information is written into the memory.

Control of the store address circuitry is returned to the time slot counter, thereby completing the relocation sequence. In this process, the first data word is cleared, leaving it available for processing the next message received.

3.3.6 *Attendant Lamp Message Loading*

The attendant lamp message is loaded into the incoming words in the same manner as the connection message. In this case both data words contain information to be relocated to the attendant lamp memory words. The message address is recognized as an attendant message and a supplementary attendant address contained in the message is gated to the message address register.

The first data word is relocated as follows. During the incoming message time slot, the message address register contents are gated to the attendant store address counter, which causes the addressed attendant word to be read out. The information read out is inhibited from reaching the output register, thereby clearing the word. On the write cycle, the new lamp information is written from the output

register into the store. The cycle is repeated for the second data word during the next occurrence of this data time slot.

3.3.7 *Maintenance Message Loading*

The maintenance message, identified by a special message address, is loaded into the incoming message words in the same maner as the connection message; the contents of the second data word are gated directly to the maintenance circuit rather than into the store word associated with a time slot. The first data word is cleared and made ready for the reception of a new message.

3.3.8 *Line Number Translation*

The translation of the calling or called party addresses from the binary form in the switch store to select the desired line or trunk circuit is accomplished in three stages (see Fig. 7). The first stage is associated with each switch store and is called the group pretranslator circuit. It converts the most significant bits of the address from binary to one-out-of-n signals to select the corresponding group of 64 lines or trunks. The group pretranslator circuit either translates the least significant six bits into two sets of one-out-of-eight signals (2A switch unit) or gates them directly to the group control circuit (3A switch unit). The second stage of translation at the group lines or trunks combines and translates information from the group pretranslator circuits as follows.

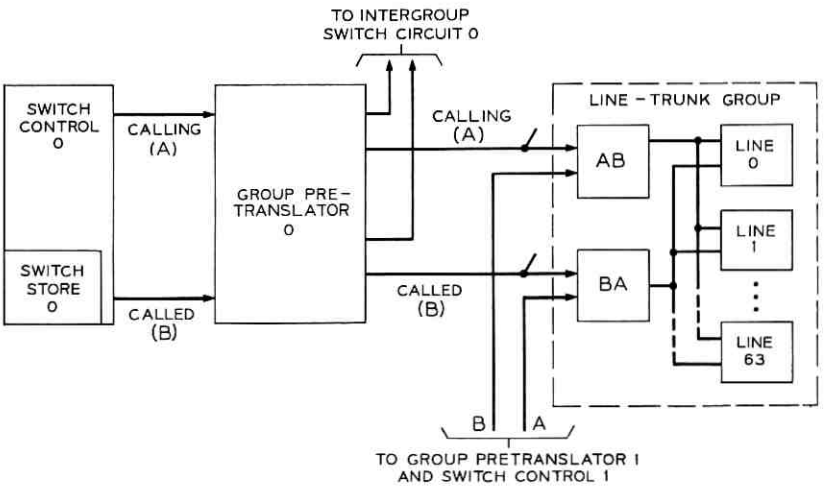

Fig. 7 — Line number translation.

The "calling" (A) party information from the group pretranslator of store 0 is ORed with the "called" (B) party information from the group pretranslator of store 1 (the AB translator). The "called" (B) party information from the group pretranslator of store 0 is ORed with the "calling" (A) party information from the group pretranslator of store 1 (the BA translator). Both the AB and BA translators have access to all 64 lines or trunks in the group.

This combining of translated information permits both incoming and outgoing intragroup calls to be completed in case of a translator failure. This kind of failure can be detected by the maintenance program which will cause the call program to select a time slot from the proper store to avoid using the failed circuitry. This combining of information which originated in the two stores places requirements on the logic and timing control circuits and on the call program in order to maintain the integrity of calls. In the 2A switch unit, the timing of the two stores is synchronized so that only one store is delivering an output at a given time. As a result, the combining of the information as described above is a time-sharing of the group translation circuitry between the two stores.

In order to obtain a greater number of time slots in the 3A switch unit, all stores deliver outputs at the same time. Therefore, information from one store is gated into only those groups which are selected by that store in that time slot. It is a requirement on the call program that the groups specified in a call in one time slot of one store be different from those specified in the same time slot of the other stores.

The third stage of the line number translator is provided on a per-line basis. Logic gates combine the matrix output information with a resonant transfer timing signal to complete the translation and operate the time-division gate.

The line number translator, in selecting and closing the line circuit time-division switch, connects the line to the group time-division bus. To complete the connection to another group, it is also necessary to select the proper time-division switch in the intergroup switch circuit. Figure 8 illustrates the time-division network. Each group of 64 lines has two time-division group buses; alternate circuit packs of 4 lines each are connected to each bus. The group buses are connected to each intergroup bus by an associated time-division switch. To complete an intergroup call, it is necessary to select two line circuit switches and two intergroup circuit switches. This selection is initiated by the group pretranslator which transmits the necessary group select and group bus information to the intergroup switch circuit.

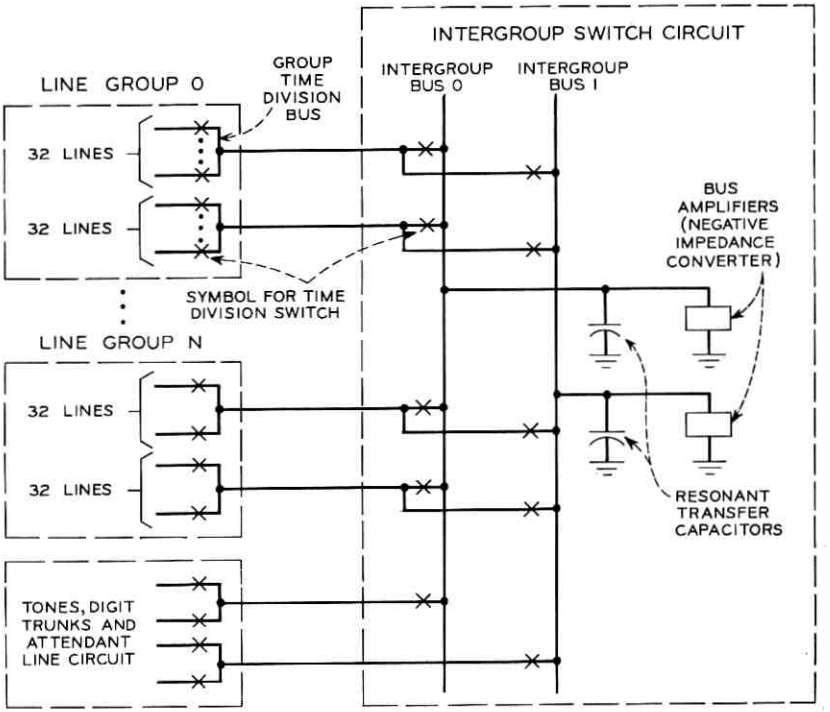

Fig. 8 — Switch unit time-division network.

This information, together with the resonant transfer timing signal, operates the intergroup time-division switches.

Intragroup calls using the same group bus are connected to the intergroup bus so that the common bus amplifier and the resonant transfer bus capacitor are included in the connection.

3.3.9 *Dialing Connection*

Dialing information is transmitted through the time-division system using two methods, one for *Touch-Tone* dialing and the second for rotary dialing.

3.3.9.1 ***Touch-Tone** Dialing*

A normal talking connection is first established between the calling party and the digit trunk circuit. The line transformer provides a voice path between the subset and the time-division network. For *Touch-Tone* dialing, the tones generated at the subset are transmitted

directly through the time-division path to the digit trunk and then to the digit receiver at the control unit via the digit trunk pair.

3.3.9.2 *Rotary Dialing*

An additional path must be established to transmit rotary dial pulses to the digit trunk circuit. This path is established using the same scan bus that the scanner uses to obtain the present supervisory state of the line or trunk circuit during the scan data time slot. The scanner interrogates the selected line or trunk circuit by pulsing the time-division switch driver; when the time-division switch is selected to sample the talking signal, the supervisory state of the line is also interrogated. This automatically places the supervisory state of the line on the scan bus at each time-division switch closure (approximately every 85 μsec). The off-hook and on-hook conditions caused by rotary dial pulses are present on the scan bus in the form of a series of pulses during the off-hook interval and no pulses during the on-hook interval. Logic in the group pretranslator circuit recognizes the digit trunk address and gates the scan bus to that digit trunk each time the connection information is read from the store. The digit trunk then filters the pulses to reconstruct the rotary dial information and transmits a 50-msec tone burst to the control unit digit receiver to represent a rotary dial pulse.

During the time a line or trunk is connected to a digit trunk, normal scanning is inhibited to prevent the scanner from interpreting the on-hook interval of a rotary dial pulse as a disconnect signal. Instead, the digit trunk provides supervisory information about a dialing line to the scanner.

3.3.10 *Conference Connection*

Two types of conferencing are used in the 2A and 3A switch units. The first is an add-on or bridging conference for three parties, one of which may be a trunk. The second is a gain-type conference which is set up by the attendant and provides for six conferees (two may be trunks) and the attendant.

The bridging conference is established in a dedicated time-slot pair which may also be used for normal 2-party connections. When used for a conference connection, a conference bit must be loaded into both time slots. Associated with each conference time-slot pair is a time-division switch which connects a capacitor onto the intergroup bus during the resonant transfer interval of both time slots.

The capacitor provides the temporary storage necessary to connect both time slots on a bridging basis.

The gain-type conference may be set up using any available time slots. Each conferee line number is inserted in a time slot with the assigned conference port address. Up to six conferees may be connected in this manner. The conference circuitry provides gains at each port, reducing the normal bridging loss.

3.3.11 *Ringing and Tones*

The ringing generator used in the switch units is a 90-volt rms, 20-hertz source. Since this exceeds the signal-handling ability of the time-division network, ringing voltage is connected to the lines by means of a per-line miniature wire spring relay which is operated by a dc signal transmitted through the time-division network to the selected line. The system tones are transmitted from common sources through the time-division network to the selected line or trunk circuit.

A line-to-line ringing connection is established when the time slot is loaded with the calling and called parties and a ring code of two bits. An immediate ring feature is provided which connects ringing to the line as soon as the calling party completes dialing. The control unit provides for changing to interrupted ringing after 1 second. The interrupted ring has a 1-second ring interval and a 3-second silent interval.

3.3.12 *Attendant Lamp Control*

Attendant features are provided in the No. 101 ESS using universal telephone consoles of the cordless type shown in Fig. 9. Each attendant has six loops which may be switched to any line or trunk in the system, one loop at a time. Signaling is accomplished when the attendant operates keys on the console to alert the system, or when lamps on the console operate to alert the attendant. For example, the system alerts the attendant to an incoming call on one of the loops by a flashing light associated with that loop. The attendant accepts the call by operating a key associated with that loop. This is detected by the switch unit scan logic, and a message is sent to the control unit. The system responds by establishing a time-division connection between the attendant and the calling party, and changing the illuminated state of the lamp associated with the loop from flashing to a steady "on."

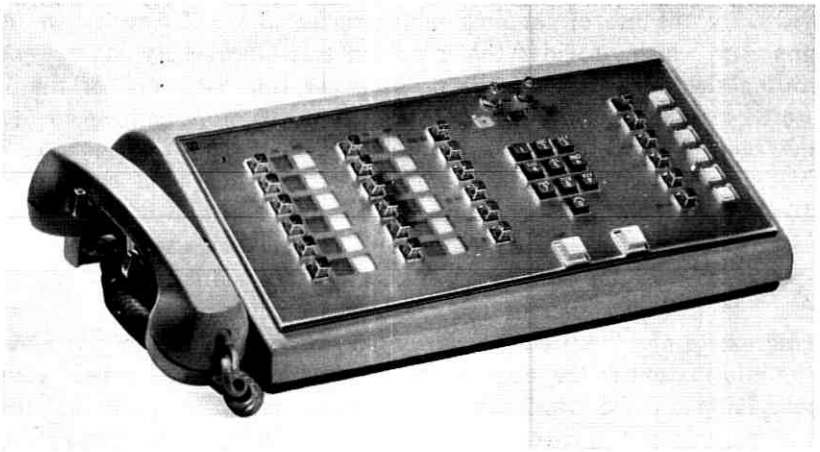

Fig. 9 — Universal telephone console.

Lamps on the attendant consoles are controlled by the control unit in a fashion similar in principle to the way that time-division switching is controlled: the new state of a lamp or set of lamps is determined by the control unit and a coded message containing this information is sent to the switch unit. This information is stored in the switch unit memory and remains unchanged until another message is sent. There are three lamps associated with each of the loops on the console. Additional lamps may be associated with any loop (for example, RDY, EXC DEST),* while other lamps are loop independent (for example, POS BUSY, CW, NS)†. Some of these lamps may be illuminated either steadily or at various flashing rates. The total number of bits required for each console is contained in four words of storage per console. Three of the four words are used to store the states of the lamps associated with the six loops, each word containing the information for two of the loops. The fourth word for each console contains the information for all of the common (or loop-independent) lamps.

The readout of the memory and lighting of the lamps is carried out on a time-division basis in which much of the common decoding circuitry and flashing rate control circuitry is time-shared among all of the lamps and all of the consoles. The smoothing required is pro-

* These are READY and EXCLUDE DESTINATION, respectively.
† These are POSITION BUSY, CALL WAITING, and NIGHT SERVICE, respectively.

vided by the use of latching pnpn triodes and RC filtering in the circuitry which provides the lamp current. Once every store cycle, during the occurrence of the proper data time slot, one of the 16 words of lamp memory is read. The attendent store-address counter determines which word it is, and after each readout, this counter is incremented, resulting in a particular word being read once every 16 store cycles, or 1.36 msec. Since the contents of each word must be interpreted in terms of the console it pertains to, there is a correspondence between the state of the attendant store address counter and the interpretation of the memory readout. Fig. 10 is a block diagram of the lamp control logic. On every lamp memory readout, the information in the store output register is gated to both the common lamp and the loop lamp logic. In these circuits, information from the store output register is combined with timing signals and gated to the appropriate lamp drivers as determined by the address of the word. The timing provides for two lamp lighting phases, during each of which only half of the information read from the store is actually used. During each phase, half of the lamp drivers are pulsed, causing the appropriate pnpn triodes to convert the single time-slot pulses to 50 percent duty factor millisecond pulses. An RC circuit then provides sufficient filtering to maintain a continuous current to the lamp.

3.4 *Memory*

The switch stores are involved in the execution of every one of the switch unit control functions. In these operations, the stores are used as shift registers, ring counters, and as conventional memory. Because each of the system control functions has a different operating cycle, the store is a random access store. The memory module consists of ferrite cores in a 2-wire, linear select array. Each word is defined by a word line linking one core for each bit in the word. Bit lines, one for each bit in a word, link all words in the store, so that in processing a word, all the bit lines operate in unison.

In this memory organization, the readout signal detection problem is complicated by the use of a single bit line for both writing and sensing. Although writing and sensing are separated in time, the input signal to the sense amplifiers during these two operations may differ by at least an order of magnitude. Thus, the sense amplifier is time-strobed. The gain of the amplifier is low during the write time,

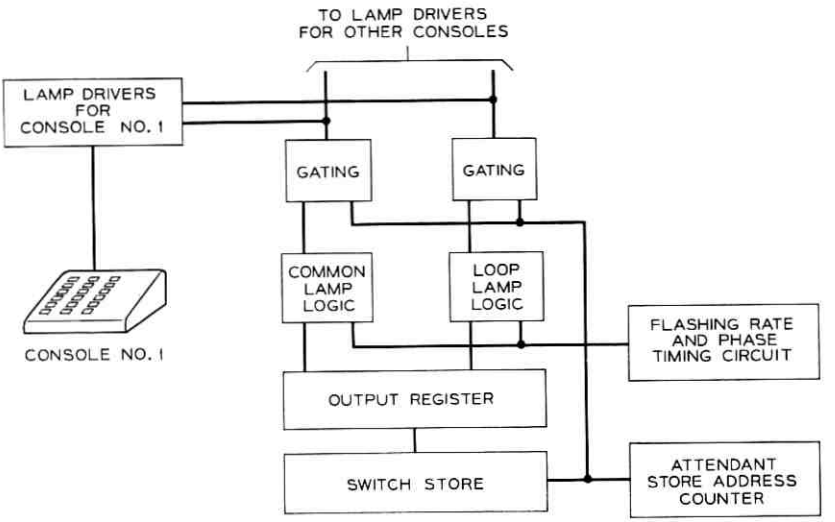

Fig. 10 — Lamp control logic block diagram.

and, during the readout interval, the gain is raised to the required level. This gain control is introduced into the sense amplifier in a manner which prevents the write noise from disturbing the bias point and dynamic range of the amplifier during the following readout interval.

3.5 *Logic*

Little is said in the description of the various logic functions performed in the switch units about the speeds required and the circuits used to carry out these functions. At an early stage in the development it was determined that a building block logic circuit approach held greatest promise for long-term economy of manufacture. A gate having no more than a 70 nanosecond worst-case delay and a 35 nanosecond nominal delay was required; the choice was a high-speed version of the transistor-resistor logic gate. The basic forms of this gate are shown in Fig. 11. To realize this gate design, two silicon planar epitaxial switching transistors were developed. These two transistors are virtually identical in operating characteristics except that the one is a double transistor in a single encapsulation as shown. Table II summarizes their characteristics.

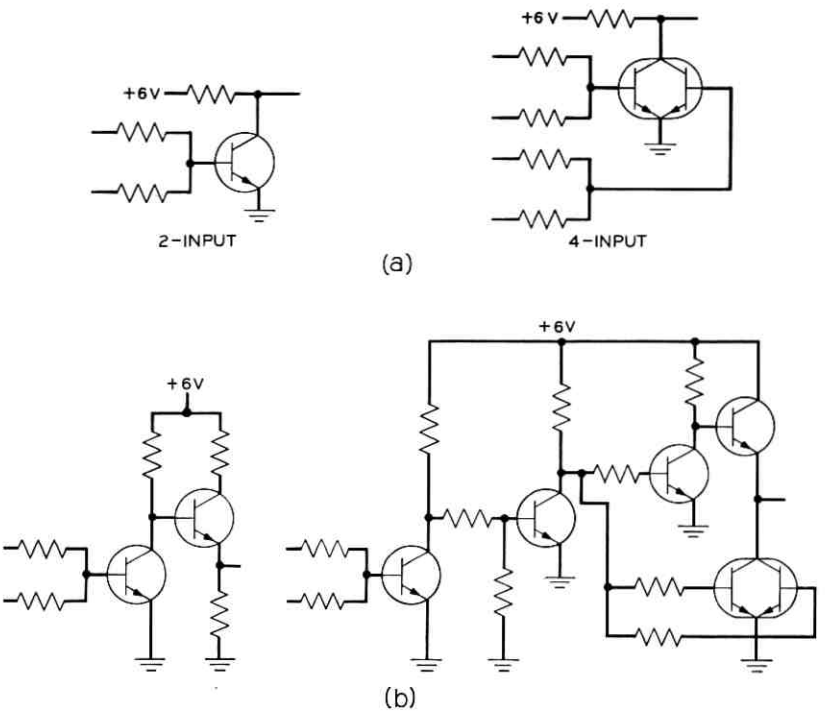

Fig. 11 — Transistor-resistor logic circuits: (a) low fan-out (fan-out $\leqq 3$), (b) intermediate fan-out ($\leqq 10$), (c) high fan-out ($\leqq 44$).

3.6 *Power*

Three potentials are used in the circuitry of the 2A and 3A switch units:

Potential	*Uses*
+6 volts	Logic circuitry
+24 volts	Talking battery (line circuits) Time-division switch drive circuitry Maintenance relay circuitry
−24 volts	Memory circuits Time-division switch bias Trunk and extended range line talking battery

These dc potentials are obtained from solid-state diode rectifiers supplied with alternating current from a single-core, multiwinding, ferroresonant transformer, connected to commercial 60-hertz single-phase power. Ringing power for the system is provided by a 20-

hertz subharmonic oscillator operating directly on commercial ac power.

In order to maintain telephone service in the event of either a commercial power failure or an equipment failure, a reserve power arrangement has been developed to provide backup for the 3A switch unit ferroresonant supply. By monitoring the commercial alternating current, the system will survive a failure of commercial power by automatically switching to the reserve arrangement. The reserve system delivers +24 volt power directly from the batteries to the switch unit. However, converters are required to convert the battery voltage to −24 volts, +6 volts, and the ringing voltage. The battery and charging rectifiers are engineered to provide as much busy-hour reserve capacity and as short a recharge time as the customer desires. The equipment design of this power system is such as to permit deletion of the reserve components if the customer so desires. In this case, in the event of commercial power failure, selected PBX lines are transferred to central office battery feed and become standard central office lines.

3.7 *Maintenance Features*

3.7.1 *Redundancy Plan*

In order to minimize service degradations resulting from equipment failures, much redundancy is included in the switch unit design. Thus, Fig. 1 shows that virtually all of the control logic is duplicated, so that a single failure affects only half of the system. When both halves of the logic and control portion are operative, some of the control functions are actually enabled in only one half;

TABLE II—CHARACTERISTICS OF LOGIC TRANSISTORS

Unity gain frequency $f_t > 400$ mHz (at $V_{CE} = 10$ Vdc, $I_c = 10$ mA)
Capacitance $C_{ob}(I_E = 0, V_{CB} = 5\text{Vdc}) < 3.5$ pf
Storage time constant $ts < 16$ nsec ($I_{B1} = I_{B2} = I_c = 5$ mA)
Saturation voltages $I_c = 10$ mAdc, $I_B = 0.5$ mAdc V_{CE} sat < 0.25 Vdc $I_c = 10$ mAdc, $I_B = 1.0$ mAdc V_{BE} sat ≤ 0.80 Vdc

the circuitry in the other is on stand-by. This is the case with scanning and attendant lamp control, so that both of these functions are unaffected by a half-system failure. However, time-division switching control is shared between the two halves, so that only half of the talking time slots reside in each store. The full traffic capacity of the switch unit is realized only when both halves are operative; therefore, a failure of one half causes a reduction in the switch unit traffic capacity and leaves all essential services intact.

Reliability is achieved in the time-division switching network by path diversity and component redundancy (see Fig. 1). Within each 64-line group of lines and trunks, the lines or trunks are separated into two groups of 32 lines, each group having its own time-division bus. A single failure which disables a bus can therefore affect at most a set of 32 lines or trunks.

3.7.2 *Failure Detection and Diagnosis*

When failures do occur, they must be expeditiously discovered, diagnosed, and repaired in order to minimize inconvenience to the customer. In the absence of any trouble conditions, both halves of the switch unit control logic are operative; scanning and attendant lamp control reside in one half or the other (though not necessarily both in the same half). Failure detection circuitry maintains a continuous check on power supply voltages (input and outputs), fuses, and the ringing power source. A continuous sequence of test calls, established by the maintenance program in the control unit, periodically checks the operation of all lines, trunks, digit trunks, tone sources, conference circuits, and time-division control logic in the switch unit. When switch unit failures are detected, the maintenance program attempts to establish a working mode in the switch unit with full traffic capacity and with the failed equipment either switched to stand-by status or at least made busy to future traffic. Failing this, a half system may be disabled. If an operating mode cannot be found, the maintenance program enables all switch unit equipment and ceases further testing until reinitiated by maintenance personnel. When failures are detected or when maintenance actions are executed, maintenance personnel at the control unit are alerted by alarms and by teletypewriter. By interpretation of teletypewriter printouts, the testing sequence may be reconstructed and the trouble condition diagnosed.

IV. 2A SWITCH UNIT

4.1 *Line and Trunk Capacity*

As shown in Fig. 1, lines and trunks in both 2A and 3A switch units are arranged in groups of 64. In the 2A switch unit, there are seven such groups; any line or trunk in any group can be connected to any other line or trunk in the same or any other group in any time slot under control of either store. With tone sources, digit trunks, and test lines excluded, the total number of lines and trunks combined is 420, which can be arranged optionally in a given installation as either 80 trunks and 340 lines or 56 trunks and 364 lines. The total busy-hour traffic capacity of the switch unit, assuming 70 percent time slot occupancy, is 1510 ccs.

For customers with fewer lines, an equipment option is available in which only four groups are provided. The switch unit provides service for 156 lines and 80 trunks or, optionally, 180 lines and 56 trunks. As indicated in Section VI, the conversion of a 180-line switch unit to a 364-line switch unit is accomplished by plugging in; no installation wiring is required. Irrespective of line size, the 2A switch unit can accommodate three attendants and seven digit trunks; the actual number used depends on the traffic requirements of the customer being served. These circuits, along with the switch unit tone sources, are equipped in a separate group in which a nonmatrix type of translation is used to control time-division switching. This arrangement precludes the possibility of a single component failure causing the loss of several of these common facilities. Time-division control of these circuits can be established from either store, so that a half-system failure does not restrict use of these facilities.

4.2 *Time Slot Arangement*

The 60 talking time slots of the 2A switch unit are divided between the two halves of the switch unit; 30 talking time slots are associated with each store. Data time slots occur in both halves because each half must be able to carry out control functions independently. As already indicated, each time slot consists of an energy transfer interval and a guard interval. Fig. 12 illustrates how the time slots in the two halves of the 2A switch unit are related. The energy transfer interval of the time slots in one half is made time-coincident with the guard interval of the time slots in the other half. Crosstalk coupling between adjacent time slots in the two stores is greatly reduced,

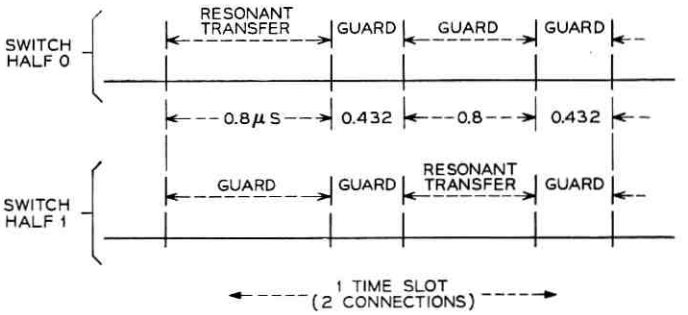

Fig. 12 — 2A switch unit half-system time slot relationship.

permitting the use of relatively inexpensive wiring for the time-division buses. Since only one time-division connection is actually established at a time, the circuitry used in the line and trunk groups is time shared between the two halves with no loss of traffic capacity resulting from mating time-slot blocking.

In addition to this "slip" between time slots in the two stores, Fig. 13 illustrates that one half has five data time slots where the other half has four. Since both halves must receive messages from the control unit at the same time and either can be controlling attendant console lamps, the last two of the data time slots, which are used for implementing these functions, are always present in both stores. However, the scanning function resides in only one half at a time and is essentially disabled in one half by the deletion of the time slot used for reading the last-look memory. Thus, in one half there are 30 talk-

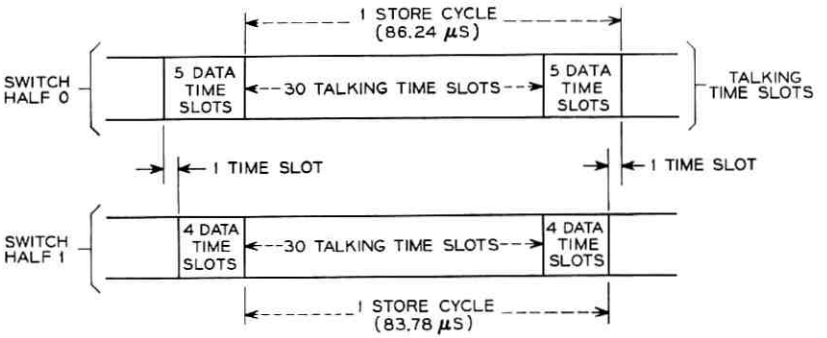

Fig. 13 — 2A switch unit half-system store cycle relationship.

ing time slots and 4 data time slots, while in the other half there are 30 talking time slots and 5 data time slots.

Irrespective of stores, the duration of each time slot is 2.464 microseconds, and therefore the cycle time of the store with 35 time slots is 86.24 microseconds; for the store with 34 time slots it is 83.7 microseconds. Thus, calls established in one store have a sampling rate of 11.9 kHz, and calls established in the other store are sampled at a 11.6 kHz rate. As a result of this rate difference, there is a periodic motion of the time slots in one store relative to the time slots in the other store. This motion of the time slots has a period of approximately 2.93 milliseconds and constitutes a process in which a given time slot in one store samples the crosstalk from a time slot in the other store at a 341 cycle per second rate. Since the baseband signal spectrum is from 0 to 6 kHz, this sampling process will cause severe fold-over distortion of the crosstalk signal energy, resulting in unintelligible noise only.

When scanning control is transferred from one half of the switch unit to the other, the number of time slots in the two halves is reversed. Thus, the store in which scanning control resides always has 35 time slots, and the other store always has 34 time slots.

V. 3A SWITCH UNIT

Figure 1 illustrates the switch unit block diagram for 120 talking time slots, each half of the system providing 60 talking time slots (as composed to the 30 provided by the 2A switch unit). Associated with the control circuitry of each half is an intergroup bus, to which all line or trunk group buses may be time-division connected. Any line or trunk has access to both intergroup buses and may be time-division connected to any other line or trunk using any time slot.

The control circuitry associated with an intergroup bus, which provides the necessary translation, storage, scanning, and message control functions is called a time-division control (TDC). Each TDC contains a switch store, with a capacity of 60 talking time slots and 5 data time slots which are normally synchronized from the switch control circuitry of TDC 0 resulting in a simultaneous time-division connection in each TDC. These mating connections are established by the call processing program in such a manner that the same line or trunk group is not selected in more than one TDC. Time-division samples do occur at the same time, requiring a high degree of isolation provided in the time-division bus cables.

Isolation between adjacent time slots is accomplished by dividing the 65 time slots into groups of 32 and 33. By alternating between these two groups, individual time slots move with respect to each other, resulting in an adjacency every 2.75 msec. Any crosstalk between adjacent time slots is therefore sampled at so low a rate as to be nonintelligible. The cycle time of the group with 32 time slots is 83.5 μsec or a sampling rate of 11.9 kHz, while the group with 33 time slots is 86 μsec or a sampling rate of 11.6 kHz.

Connections to the tones, digit trunks, and attendant line circuits are not mating time-slot restricted as are line and trunk circuits. Each TDC has a tone and digit trunk group which connects all tones, the attendant lines, and six digit trunks to the associated intergroup bus. The 3A switch unit may be equipped with a minimum of 120 time slots having a traffic capacity of 3240 ccs* and line and trunk frames for 436 lines and 112 trunks. An additional frame containing six line groups may be added to increase the maximum number of lines to 820. Two line groups may be equipped optionally as trunks to provide either 756 lines and 168 trunks or 696 lines and 220 trunks.

In the event additional traffic capacity is required, additional time slots may be provided in blocks of 60 talking time slots. In this case, a logic and control frame is added and equipped to bring the total number of time slots to 180 or 240, with a capacity of 4730 and 6130 ccs*, respectively.

When the switch unit is equipped for 180 or 240 time slots, an additional data link is required to meet the increase in data messages. This data link receives all messages associated with the added time slots. To provide for a more uniform traffic level, switch unit to control unit messages are sent alternately over both data links.

VI. EQUIPMENT FOR 2A AND 3A SWITCH UNITS

The circuits of the 2A and 3A switch units consist of gate subassemblies and loose components assembled on circuit packs which plug into equipment units which in turn are wired into two-bay frames. The wired and factory-tested frames are interconnected at the time of installation by plug-in cables. These plug-in design features minimize the time spent on the subscriber's premises for installation and maintenance.

* Without call transfer.

6.1 *Thin-Film Gates*

Tantalum nitride thin-film resistor networks deposited on a ceramic substrate are used for the logic gates and time-division transmission gates. Up to five TO-18 transistors mount on a single 0.55 by 1.8 inch substrate to form a multiple logic gate subassembly which is given a functional test before assembly onto a circuit pack. Figure 14 shows two views of a typical thin-film logic gate. A larger 1.6 by 2 inch substrate supports the transistors and pulse transformer of the time-division transmission gate, which receives a similar preassembly test. Both logic and transmission gates have wire terminals to provide both mechanical and electrical connection to an etched wiring board.

6.2 *Plug-in Circuit Pack Physical Characteristics*

Two types of circuit packs are used in the 2A and 3A switch units. Logic circuits are built on 4.6 inch high by 6 inch deep circuit packs; line and trunk circuits are built on 5.6 inch high by 11 inch deep packs.

The logic packs have space for flat mounting of ten logic gate substrates, giving an upper bound on packing density of 50 transistors per pack. The height of the substrate plus transistor permits pack center-to-center spacing as little as 0.4 inch. Circuits other than pure logic (for example, clock oscillator and store packs) are built of conventional discrete components mounted directly on the board. The overall average density for the logic circuit packs is 20 transistors per pack.

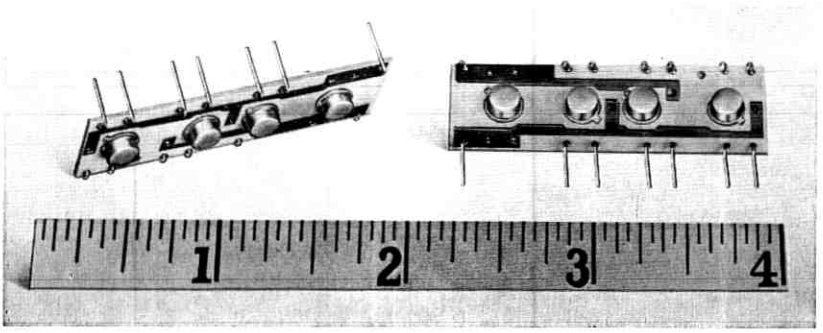

Fig. 14 — Thin film logic gate.

A 38-terminal board-end connector with plastic body and bifurcated gold-plated contacts is soldered onto one end of the double-sided etched copper-clad phenolic wiring board. A plastic faceplate with holes forming sockets around etched test point paths is riveted onto the opposite end of the pack; holes are also provided for a pack extractor tool. The width of the faceplate varies from 0.4 inches in increments of 0.2 inch to 1.4 inches as required by the highest component on the pack. Connections between paths on the two sides of the pack are made using a special highly reliable through-connection first used in the No. 101 ESS.

The line and trunk packs contain four complete line or trunk circuits or related circuits and are provided with a 46-terminal connector. A die-cast frame 2 inches wide supports the epoxy-glass composition etched wiring board upon which are mounted the relatively heavy line transformers and filter networks. To conserve space, the ceramic substrates of the time-division transmission gates are mounted perpendicular to the board; furthermore, some of the other per-line circuits are packaged on 1.6 by 2 inch "daughter boards" (etched wiring boards with discrete components), which are also attached perpendicularly. Figure 15 shows these features of the line and trunk packs.

6.3 *Circuit Pack Electrical Designs*

Although there are differences in the control circuits of the 2A and 3A switch units, circuit pack and circuit designs have been formulated to minimize the number of packs required for both the 2A

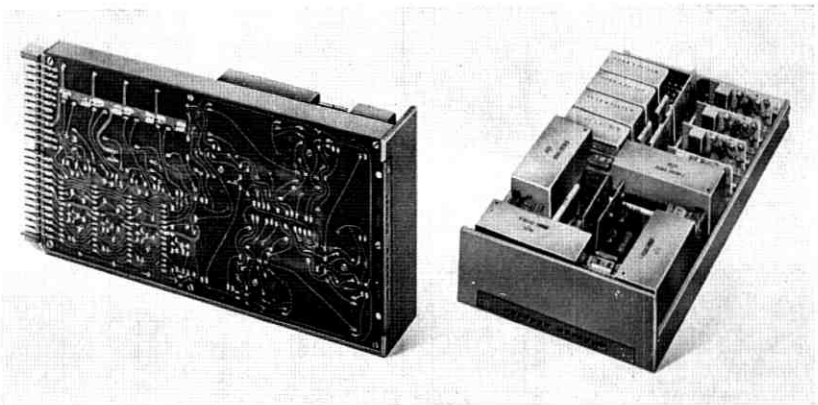

Fig. 15 — Circuit pack containing four line circuits.

and 3A switch units. A constraint of maximizing packing density to reduce the overall size of the switch unit has dictated the need for special-purpose logic packs containing many etched interconnections. General-purpose packs suffer from low-packing density because of terminal limitations, whereas special purpose packs tend to be space limited by the area of the etched wiring board but are limited in application by their specialized function.

Eighty-seven different logic packs are used in the 2A and 3A switch units. Fifteen percent of the pack types form the general-purpose core of the 2A and 3A equipment; these contain gates, flip-flops, counters, and amplifiers with a minimum of interconnections. Seventy percent of the pack types have specialized logic functions, and fifteen percent perform nonlogic functions such as store control, data transmitter-receiver, and attendant lamp driver. Despite the high proportion of special-purpose packs, 60 percent of the total logic pack types are common to both switch units.

The line and trunk circuits are identical in the 2A and 3A switch units; there are slight differences in the line group control packs and attendant line circuits. More than half of the 31 line and trunk type packs are used in common. The line and trunk circuit packs have compatible terminal assignments among themselves so that changes in line and trunk type (and in the 3A, changes from a line group to a truck group) can be accomplished by plugging in, with no wiring changes required.

6.4 *Apparatus Mountings*

The logic packs plug into die-cast aluminum apparatus mountings consisting of one, two, or three 12-inch-wide trays illustrated in Fig. 16. The card guide castings on the top and bottom of the tray have slots on 0.2 inch centers to accept any combination of circuit pack widths. Knock-out nose pieces on the front of the casting prevent accidental insertion of a pack in an unused position. A female connector snaps into slots at the rear of the casting to mate with the circuit pack connector. This connector is arranged for up to three levels of wire wrapping and the twist-lock fork terminals may be individually replaced in the field without removing the connector body and wiring on adjacent terminals. A ground strip with terminals on 0.2-inch centers is mounted under the connectors at the bottom of each tray to provide a short path from the circuit packs to the low-inductance frame ground.

Apparatus mountings for the line and trunk packs have similar

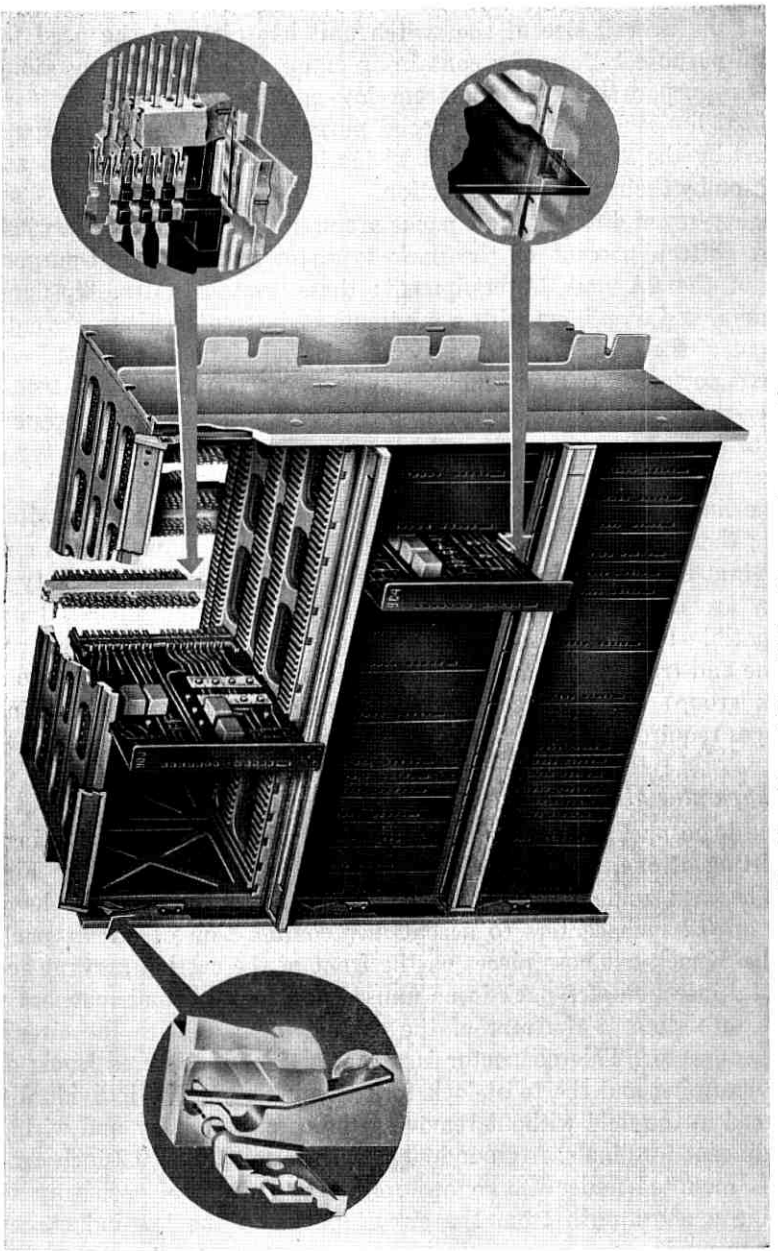

Fig. 16—2A and 3A switch unit apparatus mounting.

features, except they are 6 inches high and have card-guide slots on 1 inch centers with width to accommodate the cast frame of the packs. A mechanical interlock is provided to prevent certain circuit packs from being inserted into package locations where electrical damage may result.

6.5 *Wiring and Cabling*

The equipment within each cabinet is factory wired and tested before shipment to the field. The various equipment features and options available are implemented in three ways: first, by inserting or removing a circuit pack; second, by moving a circuit pack from one prewired connector position to another, and third, by replacing one circuit pack code by another in the same position. These methods eliminate any wiring by the installer in the switch unit itself and permit factory testing of all features and options.

Connections between frames are made using 64-terminal connectors. Single-ended connector cables are used, with the other end preformed and wired into the frame. This "umbilical cabling" technique results in smaller space requirements for connectors and higher reliability over a double-ended connecting cable, since only one pressure contact is in series with each interframe lead. Signal leads are distributed among the connectors so that the accidental removal of one connector will not disable the entire switch unit.

Logic and fused power connections between the frames are accomplished with six connectors in the 180-line 2A switch unit; three more connectors complete the signal and power interconnections to the auxiliary line frame, increasing the switch unit capacity to 364 lines. A similar expanded cabling scheme interconnects the three, four, or five frames of the 3A switch unit. In addition, the intergroup time-division buses of the 3A switch unit, which are constructed of shielded twisted-pair cable, are plugged together between the transmission frames via coaxial connectors.

External connections for lines and trunks are made using a 32-pair cable with a 64-terminal connector which plugs directly into the line and trunk group units. Four connectors are provided per group: one for the 32 tip and ring pairs per half group, one for attendant direct station selection (ADSS) control leads per half group, and two corresponding tip and ring and ADSS connectors for the other half of the group. Attendant console leads, digit trunks, and data links also leave the switch unit through 32-pair cables.

Terminal assignments in the 2A and 3A switch units are made so

that existing cross-connection wiring need not change when a 2A installation grows to the point where it is replaced by a 3A switch unit. Additional external leads are required by the 3A, but changeover involves only repositioning the 2A cables in the appropriate 3A connectors. Digit trunks, data links, and the first three attendant consoles can be replaced one-for-one, and the line and trunk group numbering plan is such that there is compatibility among the first seven groups.

Planned wiring is used to make intraunit connections in each apparatus mounting (this is bench wired before the unit is installed in the frame). Loose wiring interconnects the units in the frame, and local cables and formed switchboard cabling compose the interframe "connectorized" wiring. To alleviate wiring congestion, some of the cabled wiring is run as "air lift" cabling, that is, the wires are behind the plane of the wire-wrap terminals and come into the wiring field only at connection points.

6.6 *Cabinet Features*

The cabinets for the 2A and 3A switch units are constructed of aluminum extrusions and formed sheet aluminum parts welded together to form a basic framework into which the apparatus mountings are fastened. The frames are 34.5 inches wide by 19.5 inches deep to accommodate two bays of equipment while remaining small enough to be easily moved.

The minimum 2A control and line circuits for 180 lines and 56 trunks occupy two frames; the minimum 3A control and line circuits for 436 lines and 112 trunks occupy three frames, additional frames house added lines, control circuits, distribution (cross-connection) fields, and auxiliary equipment to give a uniform appearance to the installation.

The 2A frames are 62.5 inches high; the 3A frames are 84 inches high with the top 4.25 inches forming a removable cable rack which is installed after low elevators and doorways have been negotiated.

Bolt-on side panels and lift-off front and rear doors completely enclose the frames but allow quick access to equipment for maintenance. The decor of the cabinets is designed to blend with modern office furniture so that installation may be made in the general office area on the subscriber's premises. The frames are finished in dark covert gray textured vinyl paint; the lift-off doors are light olive gray (see Figs. 17 and 18).

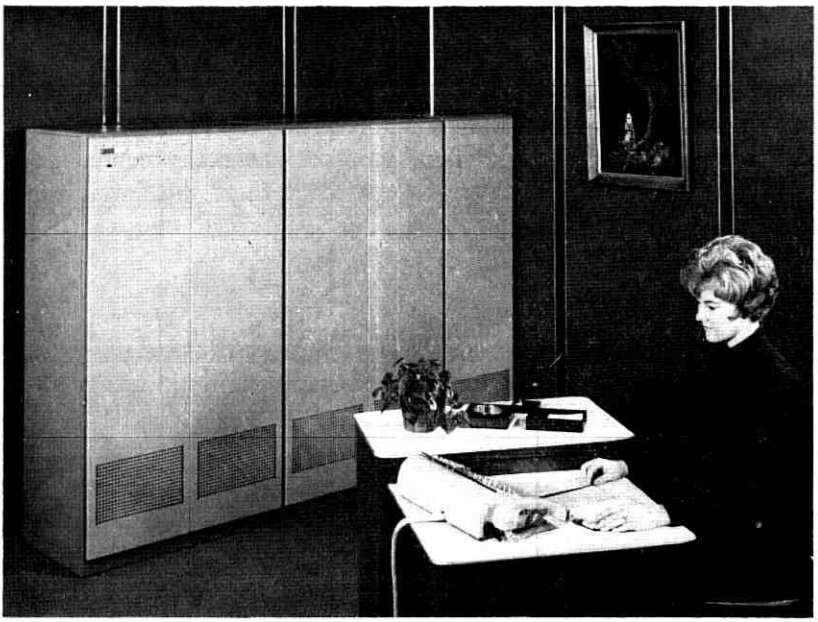

Fig. 17 — 340 line 2A switch unit.

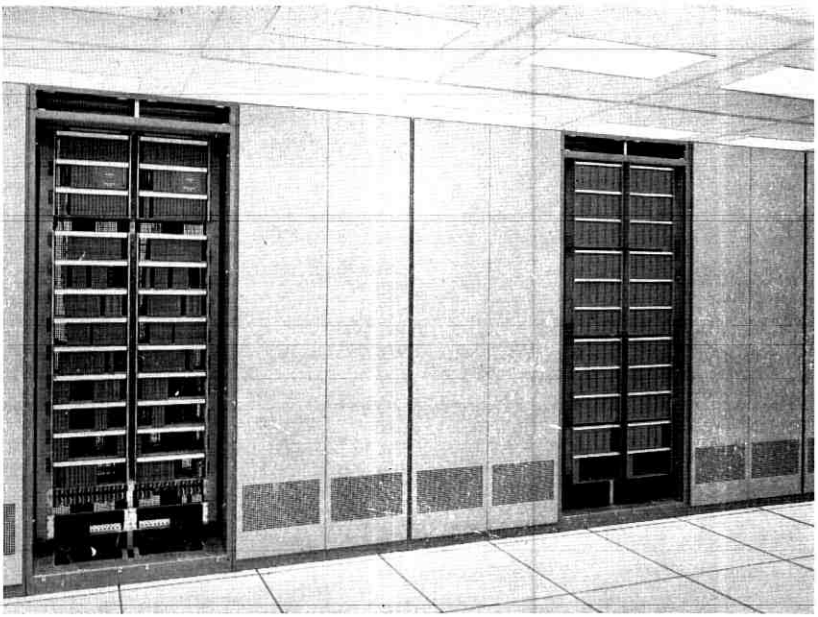

Fig. 18 — 820 line 3A switch unit.

VII. ACKNOWLEGMENTS

The design of the 2A and 3A switch units has involved a large number of people. In particular Messrs. W. B. Gaunt and R. O. Soffel have greatly contributed to the time-division circuit design. It is not possible to acknowledge individually all of the many contributors, but the authors are well aware that without them the development could not have been a success.

REFERENCES

1. Depp, W. A. and Townsend, M. A., "An Electronic Private Branch Exchange Telephone Switching System," Paper No. CP63-1043 IEEE Winter General Meeting, New York, February 1, 1963.
2. Herndon, J. A. and Tendick, F. H., Jr., "A Time Division Switch for an Electronic PBX," Paper No. CP63-577, IEEE Winter General Meeting, New York, January 27, 1963.
3. Priebe, H. F. and Seley, E. L., "No. 101 ESS 4A Switch Unit," B.S.T.J., this issue, pp. 477–495.
4. Cattermole, K. W., "Efficiency and Reciprocity in Pulse-Amplitude Modulation: Part 1 Principles," Proceedings of the Institution of Electrical Engineers, England, *105*, No. 23, Part B (September 1958), pp. 449–462.
5. Kohl, R. C. and Wadsworth, D. J., "Impact Testing of Plug-in Circuit Packages for High Reliability," IEEE Transactions on Reliability, *R-14*, No. 2 (October 1965), pp. 114–119.
6. Thomas, G. B., Jr., "Synthesis of Input and Output Networks for a Resonant Transfer Gate," IRE Convention Record, *9*, part 4 (March 1961), pp. 237–243.

No. 101 ESS 4A Switch Unit

By H. F. PRIEBE, JR. and E. L. SELEY

(Manuscript received September 11, 1968)

A combination of space division and time division networks makes possible an 800 to 4000 line switch unit private branch exchange for the No. 101 electronic switching system.

I. INTRODUCTION

The No. 101 electronic switching system (ESS) has brought new conveniences and services to private branch exchange and Centrex customers with the 200-line 1A, 364-line 2A, 820-line 3A switch units.[1-4] To extend the No. 101 ESS features to still larger customers, the 4A 4000 line switch unit was designed.

The No. 101 ESS 1A, 2A, and 3A switch units utilize time division for the switching networks. In the 1A switch unit, 240 lines and 40 trunks have access to two buses through a total of 50 time slots. With a partially duplicated bus system in the 2A switch unit 364 lines and 56 trunks are accessed by 60 time slots. The 3A switch unit accommodates 820 lines and 112 trunks with either 120, 180, and 240 time slots and a bus system similar to the 2A.

In general, the traffic capacity of a time division network depends upon the number of time slots; the line capacity depends upon the number of line circuits. As the number of lines increases, the traffic also increases; thus large line capacities require more time slots. The maximum number of time slots per talking bus is determined by the sampling rate and pulse width. The sampling rate is set by the transmission requirements; the pulse width is largely determined by active component performance and stray capacitance.[4] Substantially larger time division switching networks require considerable advancement in components and fabrication techniques.

II. LARGE PBX

2.1 *Multistage Network*

In present switching systems large line capacities with relatively small networks have been obtained with multistage networks. Most

of these systems have used space division networks; with the advent of No. 101 ESS, practical time division networks are also available. These two types of networks can be combined in various ways to obtain a large system; the characteristics of the individual networks make some arrangements preferable over others.

2.2 *Characteristics of Relay Space Division Networks*

The classical switching system has used metallic contact space division networks. These relay crosspoints have excellent transmission characteristics with a frequency range that permits simple dc supervision. Low price is an additional advantage. However, large physical size and slow operating speeds are disadvantageous.

2.3 *Characteristics of Time Division Networks*

Small physical size of relatively large capacity networks, high speed operation, and plug-in solid state circuit packs are some of the outstanding features of the time division network. On the undesirable side is the relatively large amount of per line equipment, such as the low pass filters and line transformers. The cost of the line packages in a time division switch unit is approximately half of the total switching unit cost. The transformer, needed for protection against longitudinal voltages in the time division network, blocks the transmission of dc supervisory signal and present solid state electronic devices do not permit an economical time division network that will transmit ringing voltage. Also without gain a transmission loss of approximately 2.0 dB is encountered.

2.4 *Space Division Input Network and Time Divison Output Network*

A 240 time slot 3A switch unit has a traffic capacity of 6,130 ccs* which is adequate for 2,000 lines with average traffic of 3.07 ccs per line. The 4A switch unit uses a two-stage switching network with a space division stage for line inputs and a time division junctor network as shown in Fig. 1. With a 4-to-1 line concentration ratio in the input network and a 3A time division switch with 512 lines inputs, a 2,048 line terminal switch unit is obtained. Minimum per line equipment is required and line concentration increases the traffic on the links with the resulting increase in efficiency of these circuits.

An increase in both lines and traffic, is obtained by using two 3A switching units and twice the number of line concentrators, as

* One hundred call seconds.

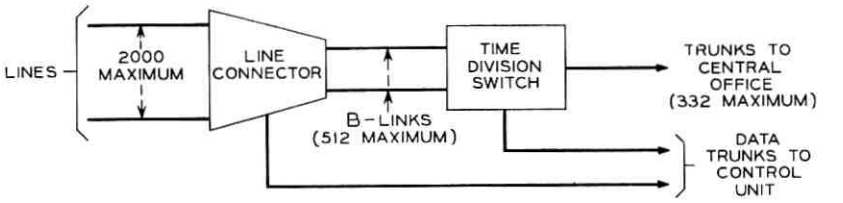

Fig. 1 — No. 101 ESS 2,000 line 4A switch unit.

shown in Fig. 2. With a 4:1 line concentration ratio the combination has 4,000 line inputs, providing a capacity for 3,200 lines with an average of 3.84 ccs per line, or 4,000 lines with 3.07 ccs per line. In the following discussion a single 3A time division switch and line concentrators will be called the 4A-1 switch unit and the two time division switch-line concentrators combination of Fig. 2 will be called the 4A-2 switch unit.

2.5 *Line Concentrator*

The No. 1 ESS 2-to-1 line concentration ratio space-division ferreed-line concentrator[5] was selected for use in the first stage network of the 4A No. 101 ESS switch units. A tip-ring connection pattern of the 32 lines to 16 B-links 2-to-1 ratio concentrator is shown in Fig. 3. To achieve a 4:1 line concentration, the outputs of two concentrators are multipled. With this network, the Private Branch Exchange (PBX) service features must be considered as well as the per line traffic capacity. For example, the six-party conference feature requires that six lines on a single concentrator must be able to get to six B-links that

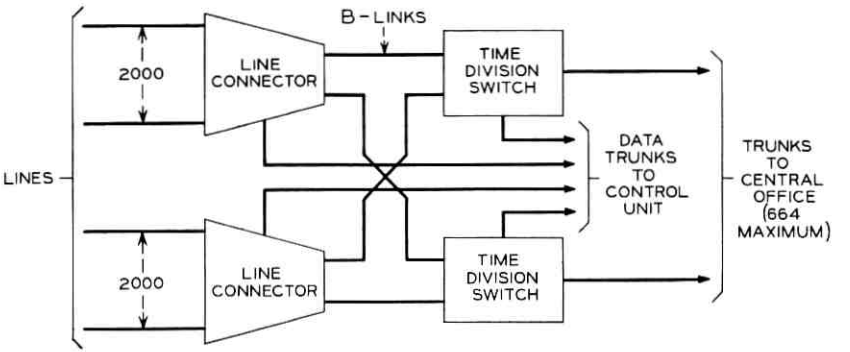

Fig. 2 — No. 101 ESS 4,000 line 4A switch unit.

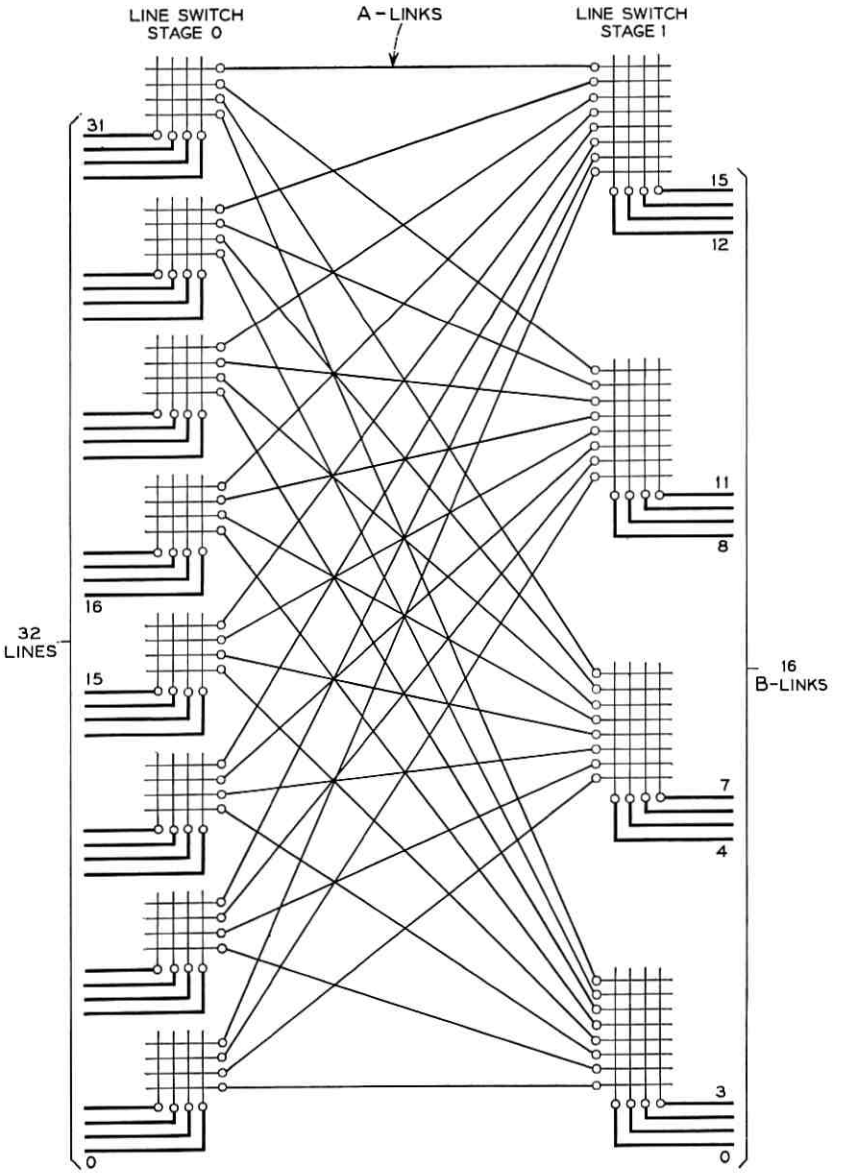

Fig. 3 — Connection pattern of 32:16 concentrator.

connect to one time division switch. Other features involve similar situations but with fewer transmission paths. Thus, the maximum division of links is two, and the interconnection of networks cannot be carried further without the loss of some features. With the 4A-2 switch unit, B-links are grouped with the odd numbered links connected to one time division switch and the even links connected to the other time division switch.

2.6 *Concentrator Traffic Capacity*

The load-service curve for the 2-to-1 ratio line concentrator is shown in Fig. 4. At a probability of 0.004 that a call cannot get an A-B link combination, the usage per line is 8.82 ccs. In the 4A-1 switch unit the 16 B-links of a concentrator terminate on one time division switch. With the 4A-2 switch unit, however, eight B-links from a concentrator terminate on one time division switch and the other eight terminate on the second 3A time division switch. Either arrangement of the 4A switch units may be operated with a 2:1 or a 4:1 line concentration ratio. The concentrator traffic capability per 16 B-links, is 260 ccs for the 4A-1 switch unit and 230 ccs for the 4A-2 switch unit.

These figures indicate the maximum ccs per group of 16 B-links; the per line traffic is obtained by dividing the concentrator maximum traffic figure by the number of equipped lines per concentrator. To

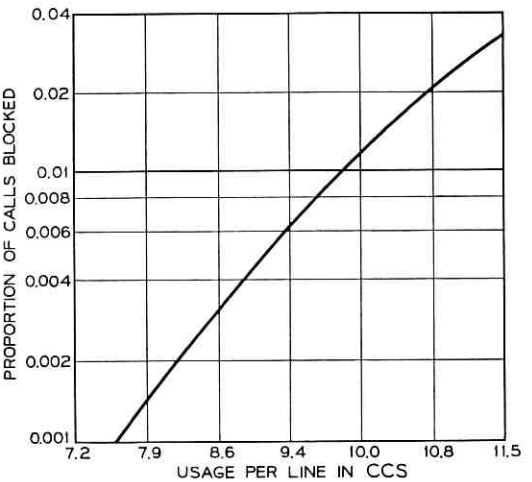

Fig. 4 — Traffic capacity of 32:16 line concentrator.

provide adequate service to a group of high traffic lines a concentrator must be operated with fewer working lines. Since intratraffic requires two links through the network, the percent of intratraffic must also be considered.

2.7 *Data Channels to Control Unit*

The No. 101 ESS is a common control system where a control unit in a central office does the call processing for switching networks (switch units) located on subscriber premises.[6] Coordination of activities between switch units and the control unit is maintained via data links between the control unit and each of the associated switch units. Original design of the No. 101 ESS was for a large number of small switch units operating from one control unit; data processing was designed so that a switch unit would use one data link. With the larger switch units more per-switch unit-data capacity was required; this is provided by using multiple data channels. The four bus 3A uses two data links; the 4A-1 switch unit uses three, while the 4A-2 switch unit has six data link circuits.

III. LINE CONNECTOR

3.1 *Block Diagram*

The line connector, shown in Fig. 5, connects station lines to the B-links which are the inputs to the time division switch. Additional required functions are the scanning of lines to detect service requests (off-hooks) and data transmitting and receiving capability.

The line concentrator scans all idle lines; when a new off-hook condition is encountered, scanning is stopped and a data message is sent to the control unit giving the equipment number of the line requesting service. Call processing at the control unit, finding an idle path, sends a connect order to the line concentrator. The line is then connected through to a B-link where it appears as an off-hook request to a 3A time division switch, and its line connector scan point removed transferring supervision control to the time division switch. On a disconnect, the message to the line concentrator removes the line's connection to the B-link and restores the line's scan point.

Line connector circuits have been physically divided into three groups: line switching circuits, line switch controller, and data converter. A line switching frame contains the per line equipment and network for 256 lines. Up to four line switching frames are accessed by a controller frame. A data converter will operate two line switch controllers. The data converter receives serial data from the control

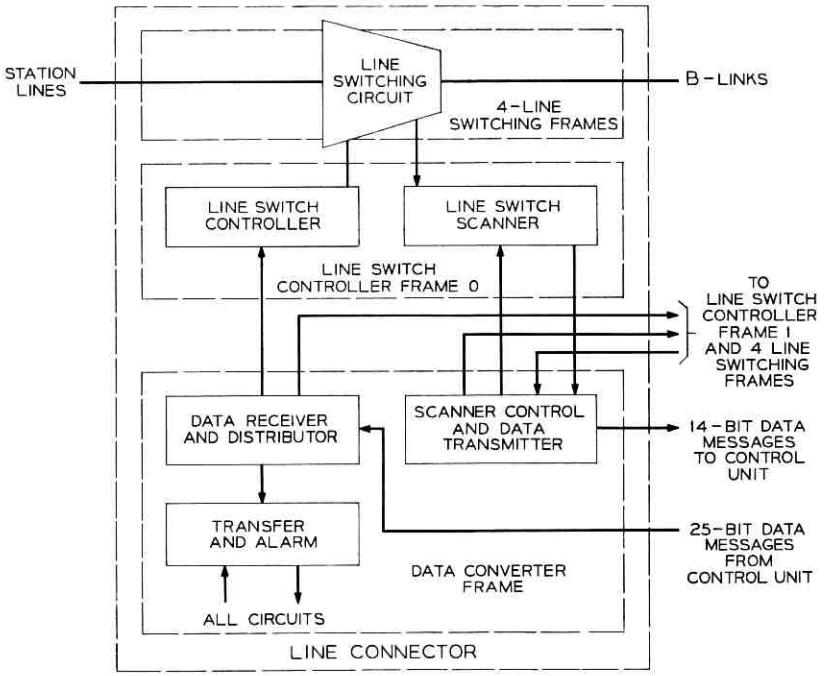

Fig. 5 — Line connector block diagram.

unit and supplies parallel outputs to the controller; in return, parallel information from the controllers is transmitted serially back to the control unit via the data converter.

Most of the circuits use diode transistor logic and follow the design pattern of the No. 1 ESS circuit packs.[7]

3.2 *Line Switching Frame*

The major function of the line switching circuit is the interconnection of lines and links. A line switching frame consists of eight 32-to-16 ratio line concentrators which accommodate a maximum of 256 line terminals and can be connected to provide either a 2:1 or 4:1 line concentration ratio. A block diagram of the circuits within a frame is shown in Fig. 6, and Fig. 7 is a sketch of the seven-foot frame. Besides the eight concentrators in a frame, there is a type 1B ferrod per line, a 48 wire-spring relay translator, and 128 cut-through relays.

Operation of ferreed crosspoint switches in the line concentrators is accomplished by applying a high-current pulse to a selected path

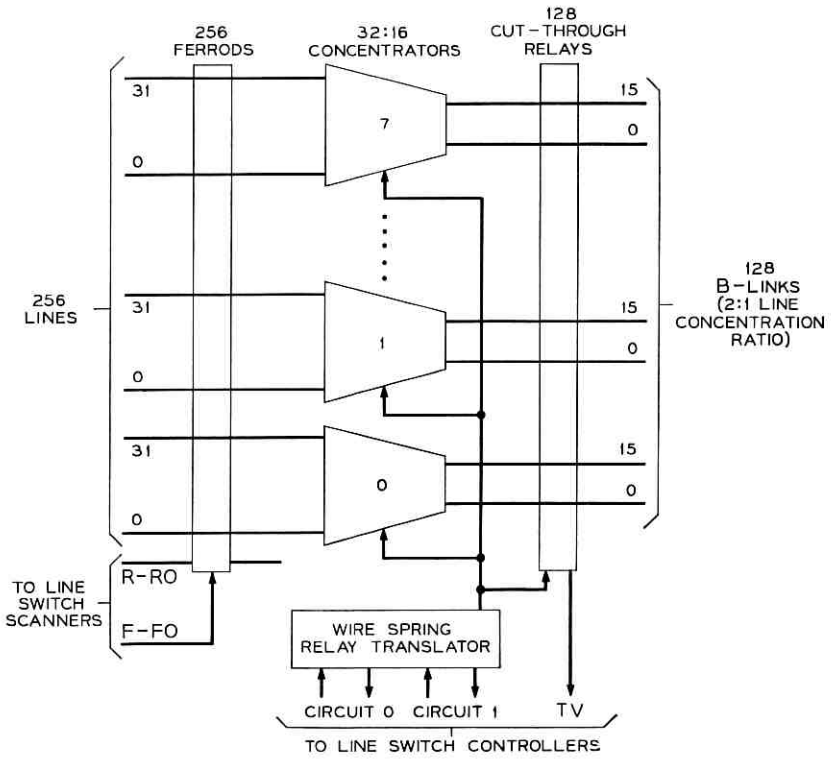

Fig. 6 — Block diagram of line switching circuits.

in the switching network. Three relays, one in each group of 16 of the 48 relay translator, select the path to be pulsed.

The ferrod sensors enable a line scanner to determine the line status since an idle line will normally have its ferrod connected to tip and ring. When service is given to a line, its connection to its ferrod is removed by action of a bipolar ferreed whose winding is in the pulsing path.

When the relay translator is operated to select a pulse-current path, it also operates a cut-through relay associated with the switching network link output. The cut-through relays have a combined function: first, to open the B-link before ferreed crosspoints are operated; second, to discharge the line; third, to connect the balanced pair from the concentrator output switch to a test circuit after the crosspoints are operated; and fourth, to cut-through the connection.

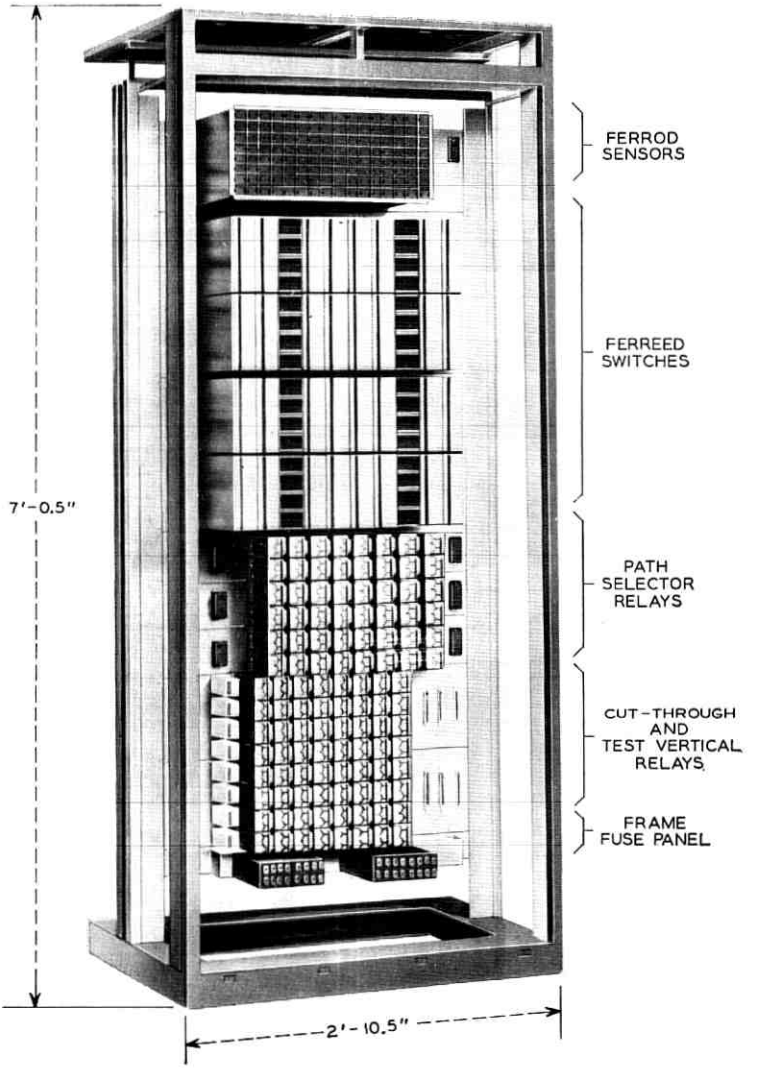

Fig. 7 — Line switching frame.

3.3 *Line Switch Controller Frame*

The line switch controller frame contains two basic circuit groups: line ferrod access circuits (line switch scanner) and line link access circuits (line switch controller). Each circuit is duplicated with one on-line and the other in standby status. Fig. 8 is a block diagram

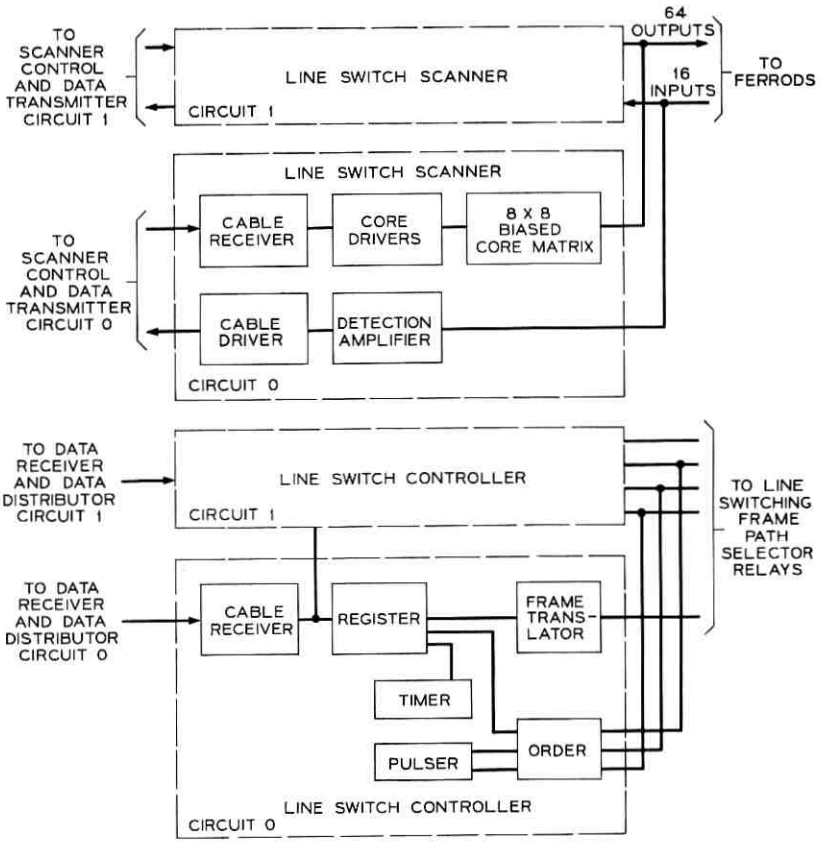

Fig. 8 — Block diagram of line switch controller.

and Fig. 9 shows the frame. A controller frame has the capacity to access four line switching frames, a total of 1024 line terminals.

3.3.1 *Line Switch Scanner*

The line switch scanner receives address pulses from a scanner control.[8] These pulses are applied to a biased core switch to give a 1-out-of-64 translation. Sixteen of these outputs interrogate a 256-ferrod matrix in a line switching frame. One switch output interrogates 16 ferrods simultaneously. These outputs are strobed, amplified, and passed on to the scanner control in the data converter frame.

3.3.2 *Line Switch Controller*

Address and order information to the line switch controller is in three groups: 26 bits of line-link data, order group of 6 bits, and an enable bit. The line-link information specifies where in the network fabric (station line and B-link) an operation should be performed, and the order group data specifies what should be performed.

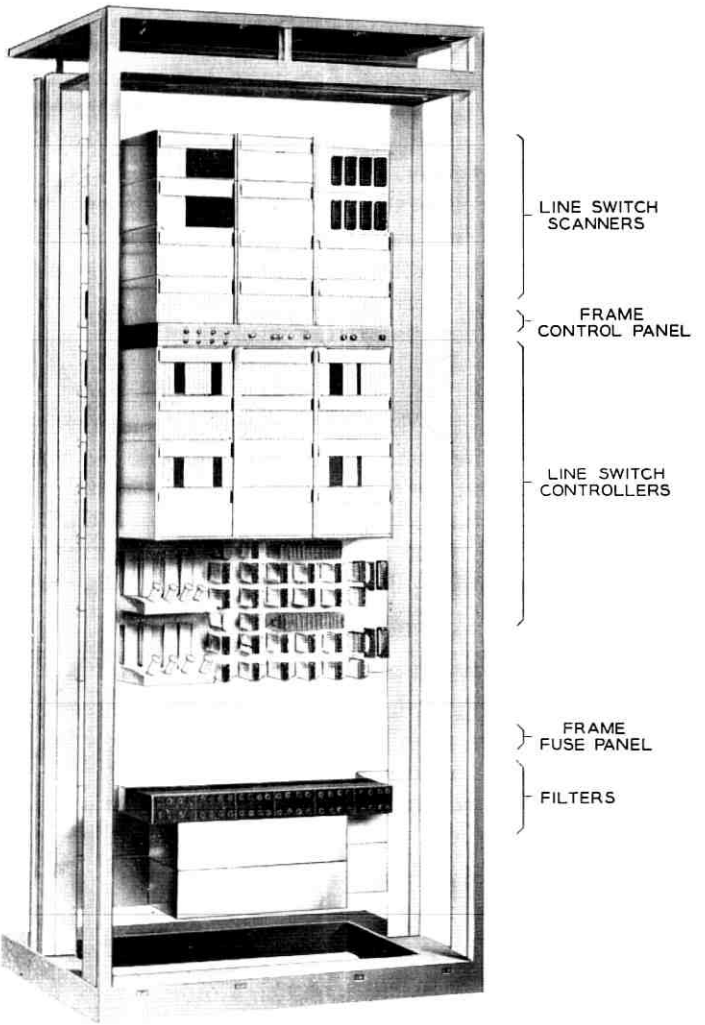

Fig. 9 — Line switch controller frame.

The line switch controller message is placed in a register and translated by a reed relay translator which operates three path selector relays in a line switching frame.

Regardless of the order being carried out, the normal timing sequence is the same. First, the path-select relays operate, selecting, in addition to the pulse path, a cut-through relay. The operation of a cut-through relay operates the high current pulser provided a pulse path exists, and ten milliseconds later the output of the test vertical circuit is strobed. Following the test vertical strobe, the relays are released and the register reset. The normal cycle time is approximately 40 milliseconds. Had the normal cycle failed to be carried out within 45 milliseconds an automatic reset circuit would release the relays and reset the register.

Following each controller action (except the connect order) on any network path in a line switching frame, a cross check is made via the test vertical. Since the test is performed after the high-current pulser has operated and before cut-through occurs, any normal condition will present a balanced pair to the check circuits.

3.4 *Data Converter*

The main function of the data converter circuits is to enable the control unit to access the remote switching network via voice band data links. Three circuits, the data receiver and distributor, the scanner control and data transmitter, and the transfer and alarms are shown in Fig. 10. These make up the data converter frame shown in Fig. 11. All circuits are duplicated except the output circuitry of the transfer and alarms circuit.

3.4.1 *Incoming Data Circuits*

The serial data message from the data receiver is assembled in a 25-bit shift register, then gated in parallel to the line switch controllers. Both incoming data circuits are active so that either may supply incoming maintenance messages to the transfer and alarms circuit; only one circuit at a time is permitted to gate to the controllers. The 25-bit data message includes a two-bit start code and an odd parity bit.

3.4.2 *Scanner Control and Data Transmitter*

Line scanning is carried out with the high order bits of a 12-stage binary counter supplying address pulses to the line switch scanner access circuits. The low order four bits of the address counter are

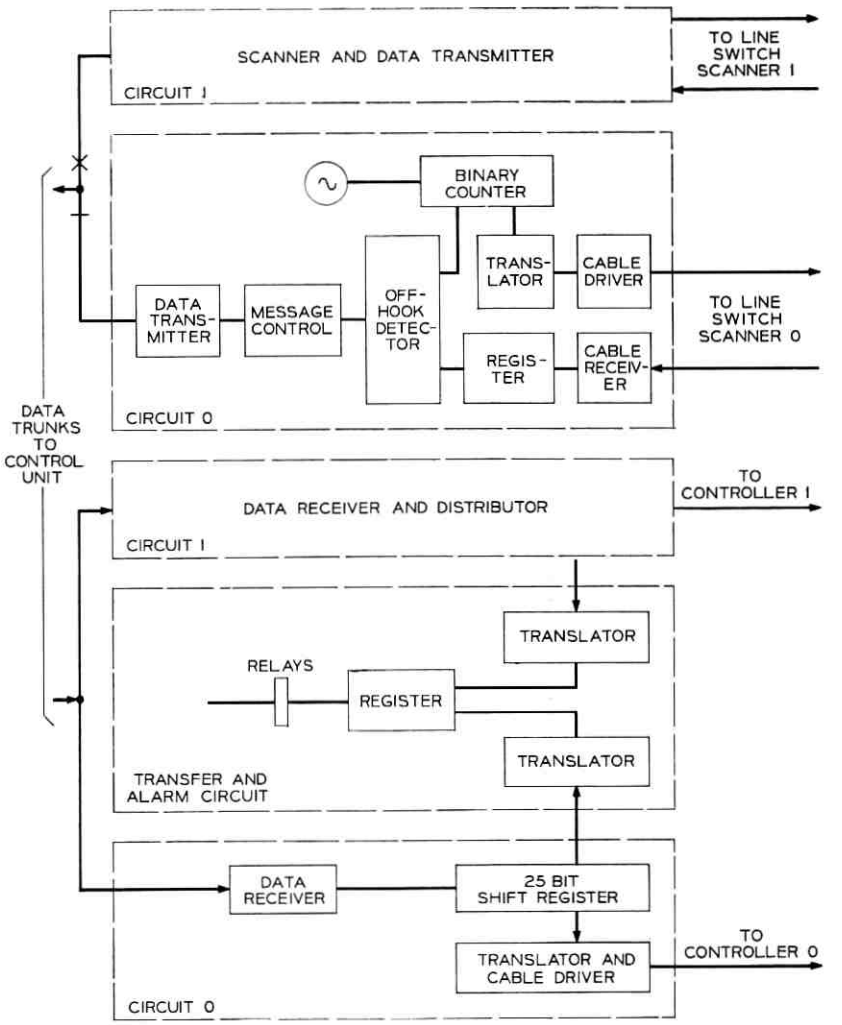

Fig. 10 — Block diagram of data converter.

used to interrogate a 16-bit register that receives line ferrod outputs. When an off-hook is detected, the address counter is stopped and a 14-bit data message is transmitted to the control unit. The data message consists of a one-bit start code, 12-bit equipment number, and an odd parity bit. Scanning resumes when either a scanner go-ahead is received from the control unit or a 0.5-second timer operates.

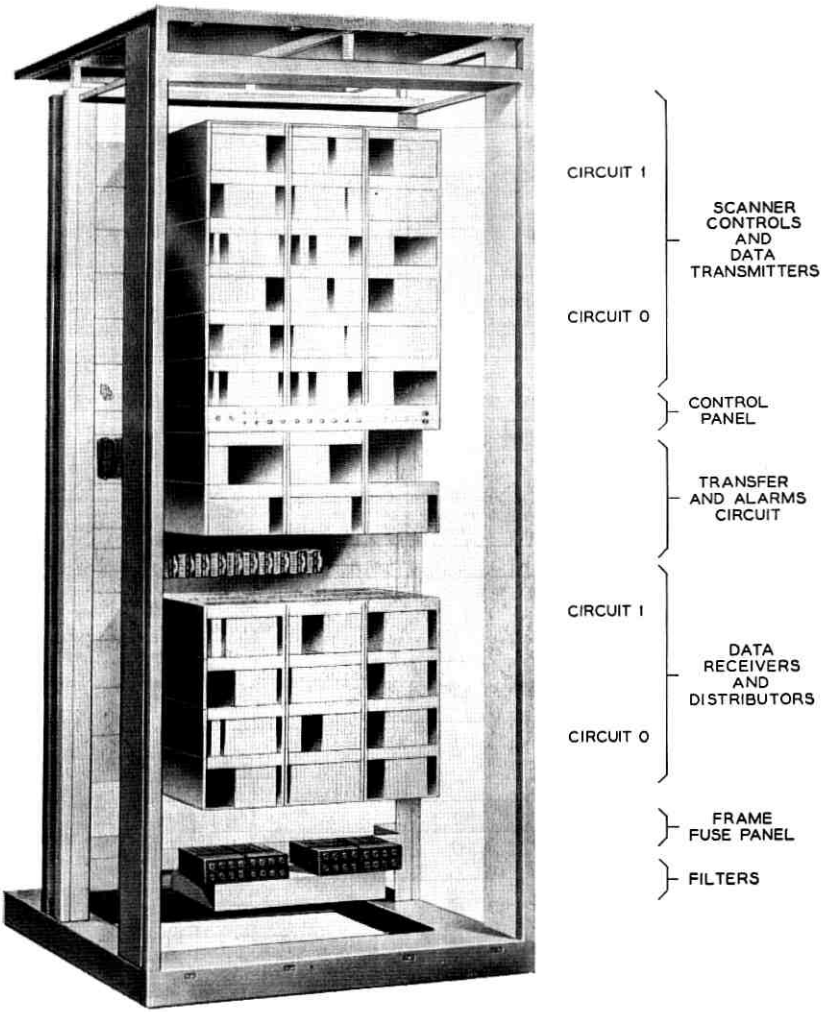

Fig. 11 — Data converter frame.

3.4.3 *Transfer and Alarms Circuits*

The main role of the transfer and alarm circuit is to control the on-line and off-line status of the various duplicated circuits and to inform the control unit, via the on-line scanner control and data transmitter, of the non-normal conditions. A 21-bit maintenance register makes up the maintenance scan points that are scanned in sequence by the on-line scanner following line scanning.

3.5 *Reliability and Maintenance Features*

The electronic circuits of the line connector are duplicated with one circuit on line and the other in standby in order to allow the system to operate in the presence of a failure. However, a finite probability of simultaneous failures in duplicated circuits remains; to decrease this probability, frequent testing is used.

During the normal call processing of setting up and tearing down calls, three conditions can exist that require immediate attention: (*i*) the on-line incoming data circuits receive a message with wrong parity, (*ii*) an enabled line switch controller times out, or (*iii*) a cross in the network of a line switching frame is detected. These three conditions set priority scan points so that the on-line scanner control and data transmitter will immediately send a message to the control unit. Upon receipt of this priority message at the control unit, the last message sent to the line connector will be repeated; if this message results in a failure, a teletypewriter printout results and maintenance programs are called into action, systematically switching gear and retransmitting messages to find a working mode.

IV. 4A SWITCH UNIT OPERATION

4.1 *Organization of the 3A*

Two basic circuit groups make up the 4A switch unit, the line connector and the 3A switch unit. The 3A switch unit is referred to as a 3A time division switch when used as part of the 4A switch unit. To adapt the 3A switch unit as to serve as the second stage network in the 4A switch unit it is only necessary to change trunk and line group assignments. In the 3A, line groups 5 and 6 are reassigned as trunk groups, and groups 8 through 15 are assigned to B-links. The 240 time slot 3A time division switch has the capability for a total of six 6-port conference circuits, 12 attendants, 24 digit trunks, and a maximum of 332 trunk circuits:

Type of Trunk	*Circuits*
CO* only	144
Tie† or CO	144
Tie or special service (FX, WATS, tel. dict, code call)	24
Tie only	20

* Central office.
† Tie trunk.

The 4A-2 switch unit has twice the number of circuits and trunks as the 4A-1 switch unit, however, the number of attendant circuits remains the same for both with a maximum of 12. The 3A time division switch controls all attendant functions directly.

Station lines connect to the line connector; trunks and service circuits terminate on the 3A time division switch.

4.2 *Two-Step Operation*

The basic elements of a 4A switch unit are shown in Fig. 12, duplicate equipment and maintenance circuits are not shown other than the four intergroup buses. Establishing or taking down connections in the 4A-type switch units requires two operations, one in each of the networks. Scanner circuits in each network scan all idle-inputs. As discussed in Section 3 scanner circuits in the line connector interrogate the line ferrods, and when an off-hook is encountered, scanning is stopped and a 14-bit message is sent to the control unit indicating the line connector equipment number that went off-hook. The 14-bit message contains a one-bit start code, an odd parity bit, and a 12-bit equipment number. Call programs at the control unit select a path (A-link and B-link) and a 25-bit message is transmitted to the line connector. Also, the control unit alerts the 3A time division switch portion of the program to expect an off-hook from the B-link just assigned. The 25-bit message contains the order (connect in this case), the equipment number, and B-link involved in the connection. The message also contains a two-bit start code and an odd-parity bit. The message is shifted into the line connector data distributor and gated to the line switch controller.

Once the controller is enabled, all of the various functions are carried out to perform the desired network action. First the path select relays are operated which in turn operate a B-link cut-through relay removing the potential from the ferreed crosspoints that are to be pulsed. The ferreeds are pulsed to connect the line, A-link, and B-link together, also, the cutoff ferreed is operated to disconnect the ferrod from the line. Relays are released and the B-link will now appear off-hook in the 3A time division switch. This off-hook will be handled just as in normal 3A operation. In this instance, the B-link will be connected to a digit trunk so that dialing may occur.

When the line goes on-hook the B-link goes on-hook, the 3A time division switch detects the change in scan point condition and sends a 14-bit data message to the control unit. The control unit deter-

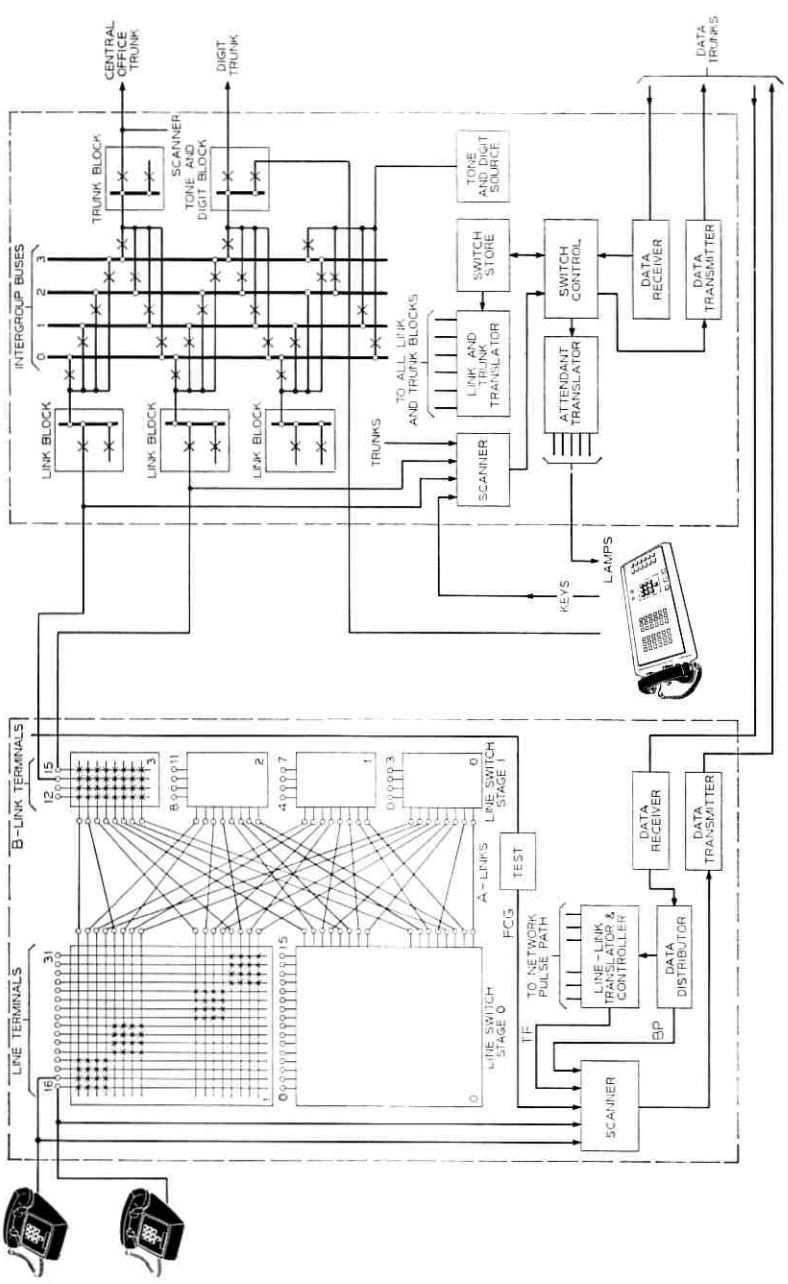

Fig. 12 — Basic elements of a 4A switch unit.

mines from its memory what changes need to be made in the 3A time division switch and in the line connector. A 47-bit message is sent to the 3A time division switch to cause it to disconnect the time division connection, and a 25-bit message is sent to the line connector. The 25-bit message is similar to the connect message, except that the order is now a disconnect which causes the line switch controller to disconnect the line from the A-link and to release the cutoff ferreed, thus restoring the ferrod sensor so that the next off-hook occurrence of the line will be detected. Before the relays are released the network path is tested via the test vertical.

A line-to-trunk call involves the time division connection of the trunk to the intergroup bus in the 3A time division switch, the time division connection of the intergroup bus to a B-link to the line connector, and connection through two ferreed switches in the line connector to the line. Tone, dialing, and ringing connections are set up in a similar manner. A line-to-line call involves two sets of ferreed switches plus the time division connections in the 3A time division switch.

4.3 *Plug-In Units*

Cables between the frames of the line connector are equipped with plug-in connectors except for the power leads. Two cable racks are provided, one at the top and the other at the bottom of the frames. Frames are of one size and fasten together in a line with end panels on the end frames. Individual front and rear panels are the same for all frames. B-link cables connect directly from the line connector frames to the 3A time division switch units and do not connect to the distributing frame.

4.4 *Options and Growth*

All the options are provided by plug-in, that is, a frame has the same wiring regardless of the options selected at the time of installation. In the data converter frame, the data link option of either loaded or nonloaded facilities is obtained by placing the circuit packs involved in the proper position in the mounting tray. If the second controller frame is used, a second set of cable drivers and receivers is installed in the positions provided.

A controller frame is equipped to handle four line switching frames (1024 line terminals); if less than the four frames are provided, the unused outputs are left idle.

A line switching frame has a 2:1 concentration ratio; by paralleling B-links (connecting the outputs of concentrators 0 and 4, 1 and 5,

2 and 6, and 3 and 7) a 4:1 concentration ratio is provided. Two plug-in jumper cables on the frame provide this option.

V. STATUS

The first 4A switch unit was placed in service in February 1967 by Illinois Bell Telephone Company to provide telephone service for more than 1300 telephones at Bell Telephone Laboratories, Indian Hill, Naperville, Illinois. By the end of 1967 a total of six 4A switch units were in operation. The 4A-2 switch unit is scheduled for service in 1969.

VI. SUMMARY

The 4A switch units provide all of the No. 101 ESS service features to large PBX and Centrex customers with requirements for up to 4000 lines. Two stage switching with a combination of space and time division has resulted in an attractively priced system.

VII. ACKNOWLEDGMENTS

The designers of the 4A switch unit have drawn heavily upon the work of others in both the No. 1 ESS and No. 101 ESS. Mr. J. G. Kappel supplied the traffic analysis of the line concentrator.

REFERENCES

1. Higgins, W. H. C., "A Survey of Bell System Progress in Electronic Switching," B.S.T.J., *44*, No. 6 (July–August 1965), pp. 937–997.
2. Depp, W. A. and Townsend, M. A., "An Electronic Private Branch Exchange Telephone Switching System," IEEE Transactions on Communications and Electronics, *83*, No. 73 (July 1964), pp. 329–331.
3. Herndon, J. A. and Tendick, F. H., Jr., "A Time Division Switch for an Electronic Private Branch Exchange," IEEE Transactions on Communications and Electronics, *83*, No. 73 (July 1964), pp. 338–345.
4. Browne, T. E., Wadsworth, D. J., and York, R. K., "New Time Division Switch Units for No. 101 ESS," B.S.T.J., this issue, pp. 443–476.
5. Danielsen, D., Dunlap, K. S., and Hoffmann, H. R., "No. 1 ESS Switching Network Frames and Circuits," B.S.T.J., *43*, No. 5, part 2 (September 1964), pp. 2221–2253.
6. Seley, E. L. and Vigilante, F. S., "Common Control for an Electronic Private Branch Exchange," IEEE Transactions or Communications and Electronics, *83*, No. 73 (July 1964), pp. 321–329.
7. Cagle, W. B., Menne, R. S., Skinner, R. S., Staehler, R. E., and Underwood, M. D., "No. 1 ESS Logic Circuits and Their Application to the Design of the Central Control," B.S.T.J., *43*, No. 5, part 1 (September 1964), pp. 2055–2095.
8. Freimauis, L., Guereio, A. M., and May, H. F., "No. 1 ESS Scanner, Signal Distributor, and Central Pulse Distributor," B.S.T.J., *43*, No. 5, part 2 (September 1964), pp. 2255–2282.

Contributors to This Issue

JAMES L. BLUE, A.B., 1961, Occidental College; Ph.D., 1966, California Institute of Technology; Bell Telephone Laboratories, 1966—. Mr. Blue has been concerned with noise in microwave diodes. Currently, he is involved in mathematical analysis of microwave diode oscillators. Member, American Physical Society, Phi Beta Kappa.

THOMAS E. BROWNE, B.E.E., 1959, Manhattan College, M.E.E., 1961, New York University; Bell Telephone Laboratories 1959—. Mr. Browne has worked on circuit design and device characterization in the development of the No. 101 electronic switching systems (ESS). In 1965 he was appointed supervisor of the 2A Switch Unit Group and in 1967 became supervisor of a group developing magnetic and semiconductor integrated circuit memories. Member, IEEE, Eta Kappa Nu.

ARTHUR N. CHESTER, B.S., 1961, University of Texas; Ph.D., 1965, California Institute of Technology; Bell Telephone Laboratories, 1965—. Mr. Chester began work at Bell Laboratories studying physical processes related to the argon ion laser, specifically electrophoresis and cross sections for energy transfer between excited states in atom-atom collisions. He then worked on the application of the silicon diode array camera tube to X-ray and high energy particle imaging. At present he is studying luminescence in solids. Member, American Physical Society, American Association for the Advancement of Science, Sigma Xi, Sigma Pi Sigma.

DAVID J. GOODMAN, B.E.E., 1960, Rensselaer Polytechnic Institute; M.E.E., 1962, New York University; Ph.D., 1967, University of London; Bell Telephone Laboratories 1960–62, 1967—. Mr. Goodman has performed analytic studies of digital communication systems. Member, IEEE, Eta Kappa Nu, Tau Beta Pi.

T. C. LOOMIS, B.S. (Chem.), Bradley Univ., 1948; Ph.D (Anal. Chem.), Iowa State College, 1953. Bell Telephone Laboratories, 1953—. Mr. Loomis is a member of the Analytical Chemistry Department,

specializing in X-ray spectrochemical analysis. He is currently supervisor of the Small Sample and Trace Analysis Group.

LEIF LUNDQUIST, Civilingenjör, 1964, Royal Institute of Technology, Stockholm, Sweden; Microwave Department, Royal Institute of Technology, Stockholm, Sweden, 1964–1965; Bell Telephone Laboratories 1965—. He is working in the Radio Systems Engineering Department and is currently engaged in interference studies. Member, Svenska Teknologföreningen, IEEE.

H. F. PRIEBE, JR., Newark College of Engineering, 1955–58; Bell Telephone Laboratories, 1952—. Mr. Priebe's major activities have been in the design of logic and memory circuits for an electronic private branch exchange. At present he is concerned with the applications of integrated circuit memory systems for the No. 101 ESS. Member, AAAS; associate member, IEEE.

ARNOLD STEPHEN ROSENBAUM, B.S.E.E., 1964, University of Illinois; M.S.E.E., 1965, University of Illinois; Bell Telephone Laboratories, 1964—. Mr. Rosenbaum is engaged in analysis relating to wideband microwave transmission system design. He is studying for his Ph.D. at the Polytechnic Institute of Brooklyn. Member, Eta Kappa Nu, Tau Beta Pi.

ELDON L. SELEY, B.S.E.E., 1956, Oklahoma State University; M.S.E.E., 1961; New York University; Bell Telephone Laboratories 1956—. Mr. Seley has been Call Processor Group Supervisor for the No. 2 ESS and has supervised the logic and system design of the No. 2 ESS. He is organizing and executing the transfer of the Step-by-Step Central Office System Design. Member, Eta Kappa Nu, Sigma Tau, Phi Kappa Phi, Omicron Delta Kapp, IEEE.

DONALD J. WADSWORTH, B.S.E.E., 1960, University of Washington, M.E.E., 1962, New York University; Bell Telephone Laboratories 1960—. Mr. Wadsworth has worked on the circuit development and physical design of the No. 101 electronic switching systems (ESS). He presently supervises a group responsible for the physical design of a new small ESS processor. Member, Tau Beta Pi, Phi Beta Kappa.

M. M. Weiss, B.S. 1941, City College of New York; M.A. 1947, Columbia University; Ph.D., 1958, New York University; Bell Telephone Laboratories, 1956—. Mr. Weiss worked on the nuclear radiation damage effects on electronic materials and devices, and various techniques for determining the radiation environment. He has been serving as radiation protection and health physics consultant to the Bell System. Since 1966 he has been supervisor of the Radiation Protection Group which is responsible for the ionizing radiation protection program at Bell Laboratories. He is vice-chairman of the company's Radiation Protection Committee and a member of the New Jersey Commission on Radiation Protection. Member, Health Physics Society, IEEE, American Physical Society, Phi Beta Kappa, Sigma Xi.

Robert K. York, B.E.E., 1957, Rensselaer Polytechnic Institute, M.S.E.E., 1961, New York University; Bell Telephone Laboratories 1957—. Since joining Bell Laboratories, Mr. York has been engaged in the development of electronic switching systems (ESS). His work has included the development of semi-permanent memories and time-division switch units of the No. 101 ESS, a switching system serving private branch exchanges. Presently, Mr. York is supervisor of the Network and Scanner Group for the No. 2 ESS. Member, IEEE, Tau Beta Pi, Eta Kappa Nu, Sigma Xi.